Theses and Dissertations

1-1-2013

Dislocation Reduction In Silicon Doped High Aluminum Content Algan Layers For Deep UV Optoelectronic Devices

HUNG-CHI CHEN
University of South Carolina

DISLOCATION REDUCTION IN SILICON DOPED HIGH ALUMINUM CONTENT ALGAN LAYERS FOR DEEP UV OPTOELECTRONIC DEVICES

By

HUNG-CHI CHEN

Bachelor of Science
Ming-Chuan University, Taiwan 2006

Master of Science
University of South Carolina, 2010

Submitted in Partial Fulfillment of the Requirements

For the Degree of Doctor of Philosophy in

Electrical Engineering

College of Engineering and Computing

University of South Carolina

2013

Accepted by:

M. Asif Khan, Major Professor

Enrico Santi, Committee Member

Mohammod Ali, Committee Member

Jamil Khan, Committee Member

Lacy Ford, Vice Provost and Dean of Graduate Studies

ii

DEDICATION

This dissertation is dedicated to my parents

for their sacrifices, supports, and unconditional love

and

to my beloved wife

who gave me the strength and courage for this achievement

ACKNOWLEDGEMENTS

ABSTRACT

III-Nitride based deep ultraviolet (UV) light emitting diodes (LEDs) are prospective candidates to replace the conventional bulky, expensive and environmentally harmful mercury lamp as new UV light sources, used in the applications of water and air purification, germicidal and biomedical instrumentation systems, etc. Due to the lack of native substrates and poor carrier injection, AlGaN-based deep UV LED is suffering from low optical power and low overall efficiency, which prevents the availability of low cost, high efficiency deep UV LED on the market.

This dissertation is focused on improving the efficiency of deep UV LEDs, by improving the base template epilayers, specifically silicon doped n-type AlGaN electron cladding layer on which the subsequent quantum well and other device layers are grown. Approaches such as short period superlattice (SPSL) nAlGaN and silicon modulation doping nAlGaN are shown to effectively decrease the threading dislocation density(TDD) from 1.2×10^9 cm^{-2} to 3×10^8 cm^{-2}, followed by the improvement of sheet resistance to $53\Omega/\square$. The improvement of crystal defect density is believed to contribute to the increase of internal quantum efficiency (IQE) and thus the overall device efficiency. Deep UV LED on a wafer device employing proposed silicon doping modulation technique shows light emission peak at 281nm and yields 25% improvement of the optical power due to the dramatic reduction of the dislocation density as well as the overall efficiency.

TABLE OF CONTENTS

LIST OF FIGURES

CHAPTER 1

INTRODUCTION

1.1 OVER VIEW OF III NITRIDE LIGHT EMITTING DIODES

1.1.1 III-Nitride Light Emitting diodes

III-Nitride semiconductor materials, including GaN, InN, AlN and its alloys such as InGaN, AlGaN, AlInN and AlInGaN have been considered as promising materials for realizing electronic and optoelectronic devices, for general purpose, commercial, and military applications. Significant breakthroughs have been achieved in the last two decades for research and development in these materials and devices, leading to successful demonstration of high power visible light emitting diodes (LED), blue- violet laser diodes (LD) and high electron mobility transistors (HEMT) devices. The III-Nitride materials with the property of direct bandgap, indium nitride (InN, Eg=0.64eV), gallium nitride (GaN, Eg=3.4eV) and aluminum nitride (AlN, Eg=6.2eV), are suitable for optoelectrical applications covering from infrared to deep ultraviolet light spectrum regions by forming a III-nitride alloy system (AlInGaN) [1].

The principle of Light Emitting Diode is to form a p-n junction where electrons and holes will recombine radiatively and thus generate photons. The energy of photons is decided by the bandgap of the region where the recombination occurred. A more detailed process will be explained in the next section. The first demonstration of a III-Nitride light

emitter was announced in 1971 by Pankove et al. Instead of forming a p-n junction, a device consisting of an unintentionally doped n-type GaN, a Zn doped insulating layer, and an indium surface contact to form a metal-insulator-semiconductor (MIS) was considered as the first current-injected GaN light emitter [2], where Zn was used as a p-type dopant, and a year later, magnesium was also induced to form a p-type GaN [3], neither of the dopants were succeeded. In the 10 years after the research efforts of Pankove and his co-workers had ended, there is not much research focusing on GaN topic until two major breakthroughs. III-Nitride epitaxial layers, due to the lack of native substrate are usually deposited on foreign substrates, such as Sapphire, SiC, Si etc, and thus the lager lattice mismatch (~13.8%, in case of GaN on Sapphire) and the difference of thermal expansion coefficient [4] causes a degradation of crystal quality and thus the delay of their development. In the 1980s, the Akasaki group achieved a significant improvement in the crystal quality of GaN by the adoption of low temperature AlN nucleation layer [5] [6]. Then dramatically decreased the deep-level impurities and defects induced electron concentration to less than 10^{15} and further increased the electron mobility to several hundreds of $cm^2V^{-1}s^{-1}$, indicating an improvement of the electrical and luminescence properties of GaN [7] [8]. The second breakthrough was the achievement of real p-type conductivity GaN, where Mg acceptors were first activated by electron-beam irradiation and followed by a first GaN p-n junction blue LED [9]. More importantly, in 1991, Nakamura et al. proposed a high temperature post growth anneal technique to activate Mg-doped GaN, carrying out a higher activation efficiency p-type GaN [10]. The two major breakthroughs in high quality single crystal growth and efficient material doping has inspired scientists to put more research efforts in the III-

Nitride based devices, resulting in marked progress in a short time frame, especially in the spectral regions of visible, such as the first demonstration of high brightness blue and green LED in 1995 [11], the first demonstration of blue laser diode [12], and the world`s first white LED, realized by applying a Y3Al5O12:Ce phosphor coating on a blue LED in 1996 [13] . The first demonstration of blue LED by Nakamura exploded the research and development in III-Nitride materials, due to huge potential applications and business opportunities, which also brought more research issues and challenges while pursuing a lower cost, higher efficiency. Many different structure designs, substrate selections, light extraction techniques have been adopted and have improved high power LED efficiency. Nowadays, applications of the III-Nitride LED are ubiquitous, and the LED efficiency has been pushed hard to reach its new record. In 2012, commercially available InGaN blue LEDs can offer a high external quantum efficiency of up to 50% at 350mA drive current, allowing the realization of a white LED performance of up to 85 lm/W [14].

1.1.2 Light Emitting Diode Efficiency

The typical structure of a Light Emitting Diode is a p-n junction diode, mainly consisting of direct bandgap semiconductors such as GaAs, GaN, etc. Once the p-n junction has been created, a space charge layer and a built in voltage (or energy barrier) will automatically be formed due to the carrier balance process. By applying an external forward voltage to the diode, the electrons and holes in conduction band and valance band respectively see a lower energy barrier and start the minority injection process by injecting electrons and holes into the depletion region and the extended region where the diffusion length can reach. The electron and hole recombination occurs during the injection and diffusion processes and the regions that this recombination took place is

called active region. If all of the carriers from the power supply can be injected into the device, all of them undergo radiative recombination to create photons, and all the generated photons can successfully escape from the device to air, this LED will be considered as an ideal LED with 100% efficiency. The performance of an LED is usually characterized by its external quantum efficiency (EQE). Currently, the best EQE value is around 50%. There are many factors, such as material defects, current overflow, total internal reflection effect, etc., that prevent the LED reaching a high EQE efficiency. Many approaches and structure designs have been reported to improve LED efficiency; these approaches and designs, and their effects to the efficiency, will be briefly reviewed below. The definition of external quantum efficiency (EQE) is the ratio of the extracted photons emitted into free space to the injected electron- hole pairs, and is usually expressed in a product of the injection efficiency (η_{inj}), the radiative recombination efficiency (η_{re}) and the light extraction efficiency (η_{ex}) as shown in Eq. (1.1).

$$\eta_{EQE} = \eta_{inj} \times \eta_{re} \times \eta_{ex} \qquad (1.1)$$

1) Injection efficiency (η_{inj})

Injection efficiency is the fraction of injected current that can be captured in the active region for the recombination process. Figure 1.1 shows the comparison of normal LED structure and an injection efficiency improved LED structure. Figure 1.1(a) shows a p-n homojunction under forward bias, where minority carriers traveling in a large range until its diffusion length can reach and the concentration decreases during the diffusion process, causing a low efficiency for recombination. The injection efficiency improved design is exhibited in Figure 1.1(b), where several techniques are used in the structure for the injection improvement such as double heterostructure, multiple quantum well (MQW),

4

and electron blocking layer. Since the homojunction LED structure will cause the carrier to be distributed to a large region for recombination and decrease the efficiency, a double heterostructure design can provide a better confinement to the carriers, by adopting a higher bandgap material as barriers surrounding the quantum well, the larger the well size, the more the carriers can be confined in this region (active region). However, a larger well size in III-Nitride LED will typically cause the so called quantum-confined stark effect (QCSE), describing the existence of a built-in electric field, resulting from spontaneous polarization and piezoelectric polarization, will cause a separation of electron and hole wave-function and decrease the probability of recombination, and thus decrease the efficiency. The MQW design can decrease the QCSE phenomenon and provide a larger active region for carrier confinement and increase the current injection efficiency. The QCSE phenomenon can be more effectively decreased by forming the structure in semipolar or nonpolar crystal direction [15]. To further capture carriers in the active region, an electron blocking layer design is also frequently used to prevent current overflow and stop electrons in the active region. The electron blocking layer is usually p-type doped to prevent a formation of barrier for holes.
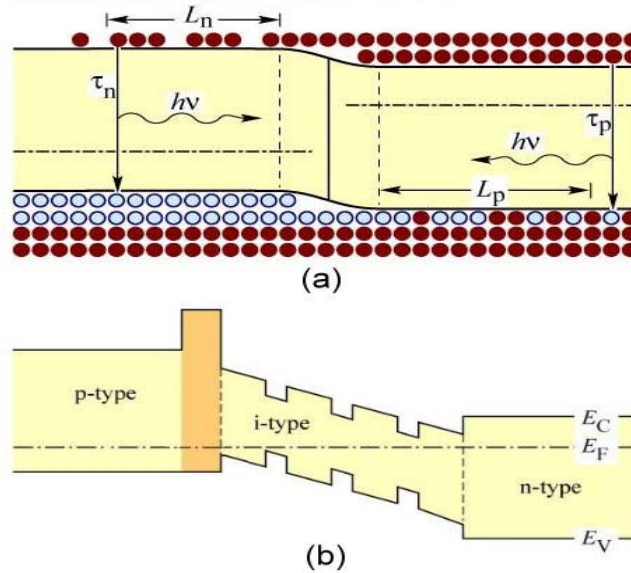
Figure 1. 1 (a) Homojunction under forward bias (b) Design of Electron blocking layer. [16]

2) Recombination efficiency (η_{re})

Recombination efficiency is the fraction of injected carriers in the active region that recombine radiatively and generating photons. There are two fundamental recombination mechanisms in LED, namely radiatively recombination and non-radiative recombination. During a radiative recombination, electrons and holes recombine followed by the emission of photons, whereas in a non-radiative recombination process, the energy is converted to phonons, generating extra heat to the material. There are several physical mechanisms such as crystal defects, surface recombination, Auger recombination, etc. which cause non-radiative recombination. Among these mechanisms material defects, i.e. unwanted foreign atoms, native defects, dislocations, etc., are the most common reasons for non-radiative recombination by creating multiple trap centers or deep levels in the forbidden region of the LED. The mechanisms of radiative recombination and non-radiative recombination are shown schematically in Fig 1.2. where part (a) shows a

radiative recombination, part(b) exhibits defects causing electron traps, hole traps and nonradiative recombination centers that result in the generation of phonons. Additionally, the non-radiative recombination via Auger processes are expressed in part (c).
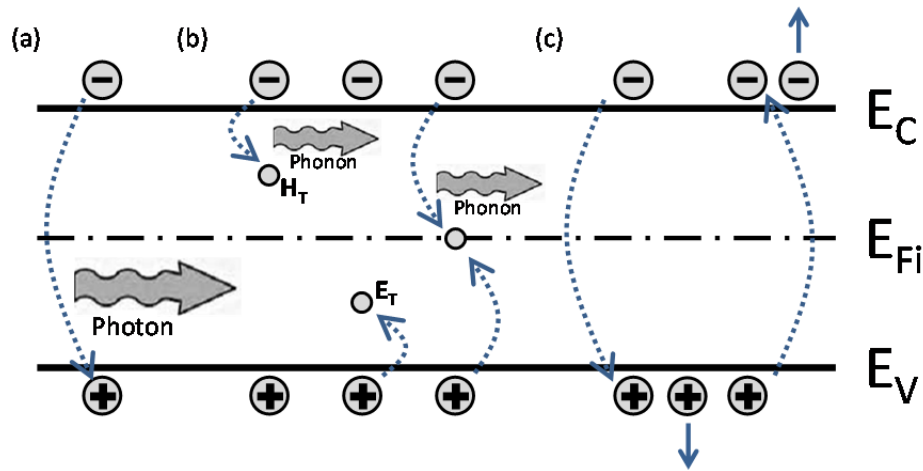
Figure 1. 2 Band Diagram illustrating recombination: (a) radiative (b) non-radiative via deep levels and (c) non-radiative via Auger processes.

Defects are the most common factor causing a non-radiative recombination, and the majority of defects in III-Nitride LED are threading dislocations with a typical dislocation density of $10^8 \sim 10^{10}$ cm^{-2} [17] due to the large lattice mismatch (16%) and large difference in thermal expansion coefficients between GaN and its foreign substrates, where sapphire is mostly used [18]. More detailed mechanisms for the generation of defects in III-Nitride semiconductor and types of these defects will be discussed in the later section. Several approaches have been proposed to decrease the defects, i.e. deep levels/ traps, to further improve the recombination efficiency in III-Nitride LED, including the use of a nucleation layer, AlN buffer layers, superlattice techniques, patterned sapphire substrate(PSS) [19], epitaxial lateral overgrowth (ELOG) [20], free-standing GaN substrates [21], misoriented sapphire substrate [22] [23] etc. The

production of the injection efficiency and the recombination efficiency is called internal quantum efficiency (IQE). Currently, the highest internal quantum efficiency is around 65% [24].

3) Light extraction efficiency (η_{ex})

The extraction efficiency is defined by the ratio of photons able to escape from the semiconductor into free space to photons generated in the active region. Due to the large difference of refractive index between semiconductor (GaN, n= 2.4), substrate (sapphire n= 1.76) and air (n=1), light incident on any of the two above mentioned interfaces will be totally reflected, if the angle of incidence is larger than the critical angle (θ_C) from Snell`s Law, as illustrated in Figure 1.3, the reflected light can escape after several bounces or eventually become trapped in the semiconductor and be absorbed by substrate, cladding layer, active region or by contacts.
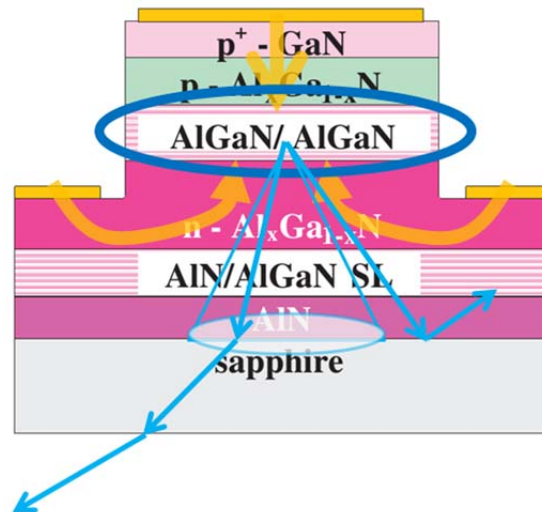
Figure 1. 3 Light Extraction and Reflection.

In terms of light extraction, several schemes such as roughened or textured surface [25] [26], patterned sapphire substrate [27] [28] and shaped LED [29] to increase the critical angle and decrease the probability of light trapping in the LED, flip-chip packaging [30] [31] to prevent the metallic contact hindering the path of light extraction and to increase the critical angle by extracting light from sapphire to free space, photonic crystal structure [32] [33] to guild light to the air and some other approaches like thin film, laser lift-off process [34] etc. have been used to improve the light extraction efficiency. Currently, the best reported light extraction efficiency is around 80% [35], and the commercially available light extraction efficiency is around 60%.

Except the external quantum efficiency (EQE), wall plug efficiency (WPE) (or power efficiency), the ratio of the optical output power to the electrical power, is also used in determining LED performance. While a power supply connects to an LED device, there will be some unavoidable voltage drop across the whole LED device, which majorly comes from the parasitic resistance, such as metal contact resistance, or lateral resistance in n-type cladding layer. A high parasitic resistance will not only cause a high drive voltage, but also increase the device temperature and result in a degradation of LED life time and reliability.

Some efficiency factors, other than the device respect, such as system engineering, packaging, etc. are needed to be considered as well, which are beyond the scope of this research and will not be discussed here.

1.2 REVIEW OF DEEP UVLED RESEARCH AND APPLICATIONS

1.2.1 Deep UVLED Applications

Optoelectronic devices emitting light in visible spectrum regions are approaching their maturity, with its implementation in many applications such as automotive lighting, residential and commercial lighting, illumination, displays, etc. Advantages, such as high efficient, compact, robust and reliability of visible solid-state optical sources are leading many groups to shift their research focus towards short wavelength ultraviolet, solid-state opto-electrical devices. The UV spectrum can be further divided into four distinct sub-regions: UV-A (320–400nm); UV-B (290-320nm); UV-C or deep UV (200-290nm); and vacuum UV (10-200nm). UV radiations usually fulfill by using UV tube technology and are capable of producing higher power levels as compared to the existing UV LEDs. However, there are many shortcomings of traditional UV lamps, including fragility and susceptibility to break, short working life span (hundreds to thousands of hours), operating at high temperatures (600-900 $^{\circ}$C) and environmental harm. Due to the improvement of growth, high quality epilayer and of packaging design, brighter, more powerful and longer-life, UV LEDs can offer an alternative to traditional UV lamps. UV-A and UV-B LEDs have seen some market available applications such as UV curing, currency counterfeit or counterfeit-sensitive documents identification, phototherapy, etc. It has been estimated that 90% of the UV LED applications are based in UV-A and UV-B regions. Also the market for UV LEDs is expected to be more than $150 million in 2016. While in the Deep UV (UV-C) spectral range, the primary LED applications are water, air and biomedical instrumentation systems sterilization. Deep UV LED (<280nm) has a germicidal effect on micro-organisms in water, air and surface by breaking- up the

chemical bonds within the DNA and RNA of organisms such as bacteria, viruses etc. and preventing their replication, as shown in Figure 1.4. DNA has an absorption peak at around 260nm, but the wavelength distribution will be dependent on the target organism such as 269nm is determined to be the most effective wavelength for Escherichia coli in water [36]. Some other applications such as Chemical and biological agent detectors [37] [38] and non-line of sight (NLOS) communications also work in this spectral range [39].
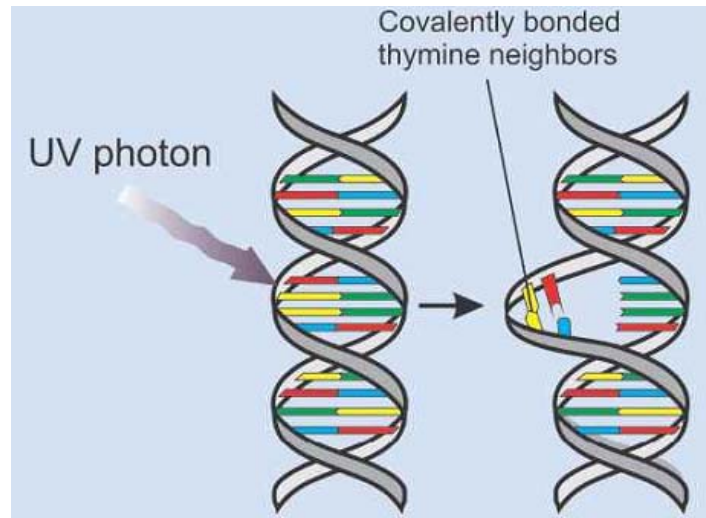
Figure 1. 4 Effect of UV radiation induced DNA bonds damage. [40]

1.2.2 Review of Deep UVLED

With a wide range of potential applications and several billion dollars in estimated market value, AlInGaN- based UV LEDs have attracted more research interest while the visible LEDs arrive at maturity, and many researchers from governments, industries and universities have shifted their research focus to a shorter spectrum wavelength UV and Deep UV regions.

AlGaN-based UV LED is considered as a light emitting diode with an emission wavelength shorter than around 360nm, while the emission wavelength above 360nm (near UV) typically has GaN or InGaN quantum wells (QWs) in the active region. The first AlGaN-based UV LEDs were reported by Sandia National Laboratory in 1998, with an emission peak at 353.6nm and an output power of 13uW at 20mA [41]. In the following years several groups published 360nm to 280nm UV LEDs in succession such as 352nm UV LED on bulk GaN by Nishida et al. [42], 340nm UV LED comprised of quaternary AlInGaN MQWs by Adivarahan et al. [43], 333nm UV LED with a Mg-doped GaN/AlGaN superlattice hole injection assistance layer by Kinoshita et al. [44] and first UV-B LED(305nm) by using the pulse atomic layer epitaxy (PALE) approach for depositing quaternary AlInGaN MQWs by Khan et al [45]. Deep UV LED research is pioneered by Asif Khan and co-workers at the University of South Carolina, who first published deep UV LED with a peak emission of 285nm and light output power of 0.25mW at a 650 mA pulsed current in 2002 [46]. Several groups have also shown their research efforts in AlGaN based Deep UV LEDs, such as 270nm - 280nm by Zhang et al. [47] [48] [49] [50], 250nm - 270nm by Hirayama et al. [51] [52], 220nm - 250nm by Grandusky et al. [53] [54], and the shortest wavelength UV LED with a light emission peak at 210nm by using an AlN emitting layer reported by NTT [55]. The maximum EQE of UV LED with emission wavelength from 290 to 360nm ranges from 2 ~7 % [56] [57] [58] [59] [60]; however, for the shorter wavelength UV-C LEDs of 290 nm and below, the EQE value is typically around 3% [61] [62]. Figure 1.5 illustrates a summary of recent works in EQE for near and deep UV LEDs.
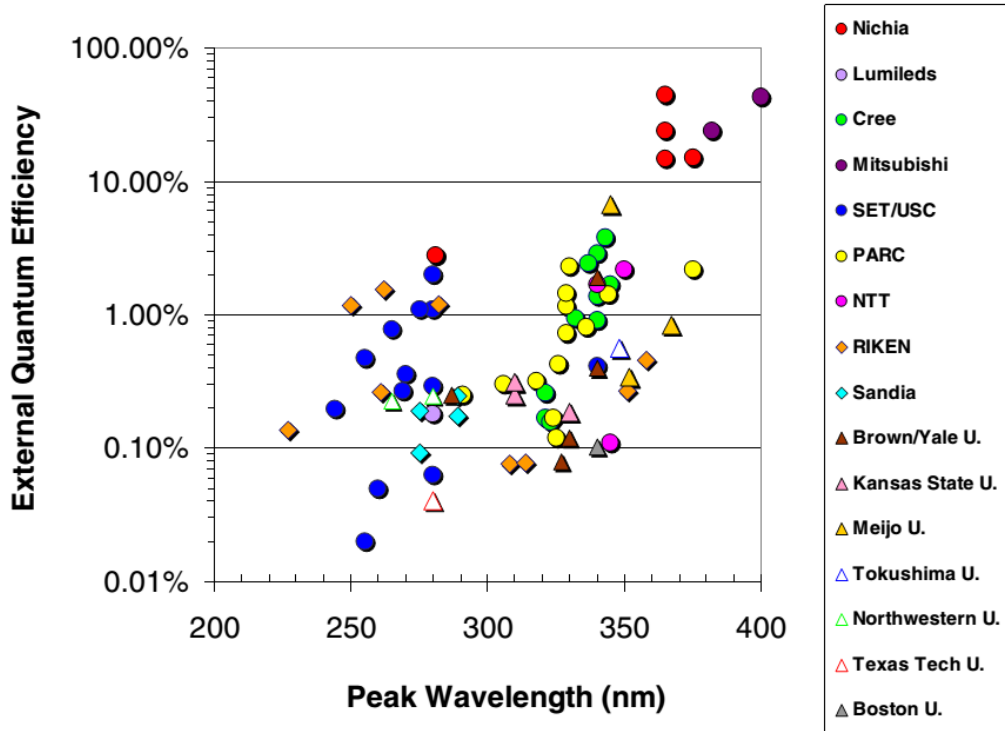
Figure 1. 5 Summary of recent works in EQE for near and deep UV LEDs. [63]

Numbers of factors account for the low EQE of deep UV LEDs. A major portion can be attributed to the relatively high defect densities. AlGaN-based deep UV LEDs typically fabricate on foreign substrate, such as sapphire (Al_2O_3), SiC, Si, ZnO, $LiGaO_2$ etc., and large lattice mismatch between the nitride films and the substrates (AlN/ Sapphire: 13.3%; GaN/sapphire: 16.1% [64]) results in high defect densities in AlGaN-based MQW, with around 60% Al composition, leading to a degradation of the recombination efficiency. Sergey et al. [65] proposed a model of the relation between nonradiative recombination and dislocation density, and suggested threading dislocation in the AlGaN material acting as trap centers [66] [67] in the forbidden region, where the nonrecombination occurrs by the approach of Shockley-Read [68] through the mid-gap traps. In order to get a recombination efficiency close to unity, it was suggested that the

13

dislocation density has to be reduced to around 10^7 cm^{-2}. Due to the high lattice mismatch and the low surface mobility of Al atoms on the growth surface, causing a poor lateral growth, the threading dislocation densities of deep UV LEDs are typically around 10^{10} cm^{-2}. An epilayer structure of typical AlGaN-based deep UV LED is schematically shown in Figure 1.6, which can be divided into five different parts, namely, substrate, buffer layers, n-type barrier, active region, and p-type barrier. In the figure, the AlN buffer was first grown on the sapphire substrate, but due to the large lattice mismatch, tremendous dislocations were generated at the interface of the sapphire and AlN layers, and penetrated through the active region to reach the surface of the LED structure, causing a nonradiative recombination in the active region and thus a low recombination efficiency.
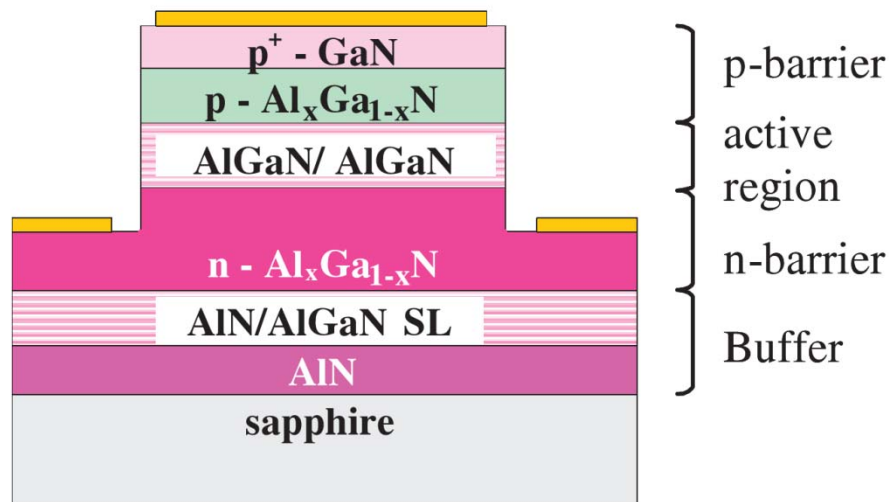
Figure 1. 6 Schematic of a typical UV LED.

Many approaches have been proposed to reduce the defect densities in AlGaN-based deep UV LED structure, among them, approaches providing a high crystal quality, low dislocation density buffer template layer have mostly been reported. Many groups

adopted a two-step growth process by first depositing low temperature (LT) AlN nucleation layers, followed by a high temperature (HT) smoother AlN layer; they also suggested that this approache can increase two dimensional growth and the grain size, decreasing the formation of dislocation on the grain boundary dislocations can also be redirected by a subinterface between the LT-AlN and HT-AlN, which can be optimized by tuning the III/V ratio, carrier gas flow etc. growth conditions [69] [70] [71] [72]. A multiple interfaces AlN layer formed through an ammonia pulsed-flow multilayer growth technique [51]or multiple modulation of the III/V ratio technique [73] have been reported. Some others techniques such as bulk AlN layer, which provides a radical method to decrease the lattice and thermal expansion coefficient mismatch [74] [75] [76], and an epitaxial lateral overgrowth technique (ELOG) [77] [78], which provides a gate for releasing the lattice mismatch-induced strain and thus a decrease dislocation density as shown in Figure 1.7(a). In addition to the above-mentioned high quality AlN buffer layer, techniques like AlN/AlGaN and $Al_xGa_{1-x}N/Al_yGa_{1-y}N$ short period superlattice lattice (SPSL) have been grown on the quality improved AlN buffer layer and worked as the threading dislocation filter layer, resulting in a crack free and smooth AlGaN suface as shown in Figure 1.7(b) [79] [80]. Other techniques like ELOG AlGaN [81] [82], pseudomorphic growth of AlGaN on bulk AlN [83] [84], rough/smooth AlGaN [85] etc. have been reported to be able to decrease the threading dislocations in the deep UV LED structure. Native AlN substrate has been adopted and mitigates the defects problems; however, the commercially available AlN substrates with a limited area around 1 inch are still cost prohibitive [86]. Although the above-mentioned efforts can provide an efficient way to decrease the dislocation density, currently available deep UV LEDs still have an

average dislocation density of around 5×10^8 to 10^9 cm^{-2}, which corresponds to 50% to 20% internal quantum efficiency from a simulated model [65], indicating further research in improving the crystal quality and decreasing the crystal dislocation is required.

(a)　　　　　　　　　　　　　　　　(b)
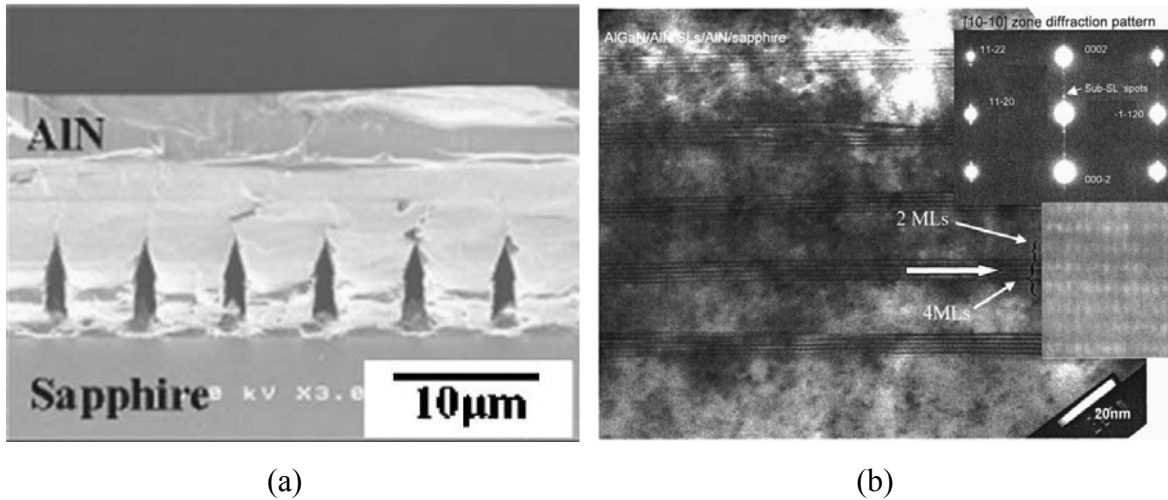
Figure 1. 7 (a) Cross-sectional SEM image of epitaxial lateral overgrowth AlN technique (b) Cross-section TEM image of PALE AlN/AlGaN superlattice. [77] [80]

Apart from the high defects, another source of the low EQE of deep UV LEDs is the insufficient current injection efficiency. High Al content in the AlGaN layer raises the issue for n-type and p-type AlGaN for the purpose of electron cladding layer and electron blocking layer respectively. The reason for these challenges is believed to be attributed to an increase in donor activation energy [87], dislocation density and a compensation effect from acceptor-like defects [88]with increasing Al mole fraction. By improving the material quality and optimization of doping level, the sheet resistant of n-type AlGaN with Al content of 60% is around 250Ω/□, while p-type AlGaN with even higher Al content can easily reach hundred times higher sheet resistance, due to the existence of Mg-H complexes, where the hydrogen source may come from carrier gas, nitrogen precursor, NH3, and in the metalorganic sources, as well as increased ionization energy

16

for Mg acceptors with the increase of Al more fraction [89], resulting in a poor hole injection and a current leakage from the active region [90]. The activation energy of Mg acceptors of AlGaN with 70% Al content is around 400meV, while for Si-doped AlGaN, the activation energy is around 10 ~25meV [91], which is lower than room temperature thermal energy (~ 26meV). Currently, the p-AlGaN doping is still a challenge and major cause for poor injection efficiency. Other than the doping issues, several approaches have been reported to provide efficient electron blocking layers, such as composition graded p-AlGaN for decreasing hole injection barrier [92], multiaqantum barrier electron blocking layer enhancing the effective barrier height and thus a 2.7 times improved efficiency [93], thin AlN insertion layer between p-AlGaN blocking layer and AlGaN MQW to suppress the current overflow and diffusion of Mg into MQW [94], etc. ,providing a better electron confinement and thus improving the current injection efficiency.

Other causes related to the poor EQE of deep UV LEDs is low light extraction efficiency. The average light extraction efficiency of deep UV LED is lower than 8%, due to (i) the total internal reflection (TIR), since a highly difference of refractive index from semiconductor to air, (ii) the absorption in p-GaN contact pad as well as the wire-bonding pads and (iii) the lack of suitable encapsulation polymers for deep UV LEDs. To prevent light absorption by the p layers and the contact pads, a filp-chip is commonly used, which also provides a path for heat dissipation [95] [96]. Other proposed methods such as the use of vertical injection thin-film structure [97], nanopixel contact with Al reflector [98], microlens array [99], moth-eye structure of sapphire back-side surface [61] etc. have been reported to improve the light extraction efficiency. From most recently, Sharalov et al. published 278nm AlGaN-based deep UV LED with a light extraction

efficiency of around 30% by adopting UV transparent p-type cladding and contact layers, UV reflecting ohmic contact as well as an optimized encapsulation, and thus a record high EQE of 10.4% and a output power of 9.3mW at 20mA pump current [100].

Some other potential factors such as (i) carbon and oxygen incorporation in AlGaN acting as nonradiative recombination centers, which can be mitigate by preventing the leakage of MOCVD system as well as the system contamination (ii) quantum confined stark effect (QCSE) which is more sever in high Al content UV LED, due to the increase of polarization field, resulting a red shift and degrade recombination efficiency; approaches like thin quantum well structure and semipolar UVLED have shown an reduced QCSE phenomenon [15], (iii) thermal management for high power LEDs etc. require further studies and research efforts to pursue commercial available high efficiency AlGaN-baed deep UV LED.

1.3 DISSERTATION SYNOPSIS

This dissertation is focused on developing high-efficiency Deep UV optoelectronic devices, by improving the base template epilayer crystal quality specifically silicon doped n-type AlGaN electron cladding layer on which the subsequent quantum well and other epilayers are grown. The working principle and efficiency of III-Nitride light emitting diode is first reviewed followed by an introduction of UV LED application and review of deep UV LEDs in Chapter1. In Chapter 2, the problem of developing high efficiency deep UV LEDs is explicated as well as the experiment methods employed in this work are explained. Chapter 3 focuses on the development of crack free, low dislocation, and high conductivity high Al content si-doped AlGaN layer by the adoption of proposed short period superlattice (SPSL) silicon doped AlGaN.

Another proposed technique for developing high crystal quality of silicon doped AlGaN, namely, silicon doping modulation AlGaN will be discussed in Chapter 4. In Chapter 5, AlGaN-based deep UV LED will be fabricated by adopting the quality improved silicon doping modulation AlGaN layer, and a study to compare the power raised deep UV LED with the conventional deep UV LED will be shown. Last, in Chapter 6, the conclusion of this work and the future works including a work of high quality semipolar AlN template on m-sapphire will be presented.

CHAPTER 2

PROBLEM IDENTIFICATION AND EXPERIMENTAL METHODS

2.1   PROBLEM IDENTIFICATION

AlGaN-based deep UV LED is suffering from a low total efficiency, including external quantum efficiency (EQE) and wall plug efficiency (WPE). High crystal defect density in the LED structure, especially in the active region, bring a nonradiative recombination state and is one of the major reason contributing to low internal quantum efficiency (IQE) as well as the overall efficiency and thus methods to decrease the defects in the active region is imperative for pursuing a high efficiency deep UV LED.

To decrease the crystal defects, some approaches have been proposed to produce a high quality base template on which the n-type AlGaN electron cladding layer, multiple quantum well, p-type AlGaN electron block layer and p-type GaN are grown. Most of these approaches were focused on undoped buffer layers including aluminum nitride (AlN) layers. Many alternatives such as Rough/smooth AlN layers, AlN/AlGaN superlattice layers, etc. have been shown to reduce the dislocation densities to the order of 3×10^8 cm^{-2}.

Upon the template, the n-type AlGaN electron cladding layer is crucial in determining 1) the internal quantum efficiency (IQE), since it is the layer right below the active region, and the threading dislocations in this n-AlGaN layer will propagate through

the active region to the surface of the LED structure. These dislocations in the active region act as the trap center to facilitate non-radiative recombination and thus degrade the internal quantum efficiency (IQE); 2) the current spreading, n-AlGaN layer plays an important role in deciding the uniformity of current spreading through the active region. A high resistance of n-AlGaN layer will result in a current crowding issue causing a non-uniform light emission, also will increase the device series resistance leading to an increased operating voltage and thus degrade the WPE, and will raise the junction temperature and further influence the device reliability and life span.

To decrease the defects in the n-AlGaN layer, this may also improve the electron mobility and thus decrease the resistivity, several groups have reported to improve the crystal quality of III-nitride layers and most of them are focused on producing a low defect density undoped buffer layer. Our group has been adopting a novel two-step pulsed atomic layer epitaxy grown high quality AlN nucleation layers, AlN/AlGaN superlattice, rough/smooth undoped-AlGaN [101] , etc. as template for the consequent deep UV LED epilayers. These optimized high quality templates have low dislocation density of 3×10^8 cm^{-2} and are expected to result in a low defect deep UV LED device structures and further improve the optical power efficiency. However, when silicon is doped in a high aluminum content AlGaN layer on such low defects template to achieve n-type conductivity, the dislocation density immediately increases to $1{\sim}5\times10^9$ cm^{-2}. Figure 2.1 exhibits a 1μm×1μm AFM image of conventional n-AlGaN with the etch pit density of 1.2×10^9 cm^{-2}, which is calculated by the number of counted defects (pits) within the scan area and is correspond to threading dislocation in the material, grown on a low defects template. Moreover, if we lower resistivity simply by increasing the silicon

doping, the defects go up. If silicon doping is kept low and the thickness is increased to achieve a low resistivity, the layers crack. Approaches exert on low resistivity thick n-type AlGaN layer itself are not much reported such as, indium doped nAlGaN[10], δ-doping nAlGaN[11] etc. However, these methods have to sacrifice either surface roughness, layer thickness, or layer conductivity.

As mentioned above, high quality n-type AlGaN layer is of tremendous importance to the device performance. It is necessary to prevent the increase in dislocation density in the n-type AlGaN layer. Thus, a high crystal quality n-AlGaN electron cladding layer, which can maintain a low dislocation density from template or acting as a dislocation filter and manage the strain to be capable of growing thick layer for achieving low resistivity is required. The n-AlGaN layer with highest conductivity for improving current crowding issues and large thickness to assist heat dissipation is essential for achieving a high efficiency deep UV LED.
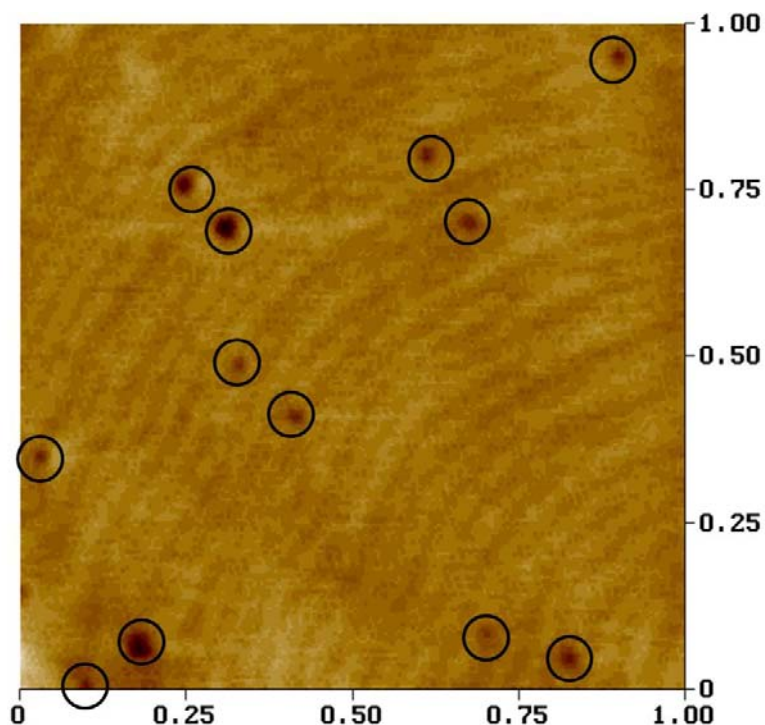
Figure 2. 1 AFM image of conventional n-AlGaN (EPD~1.2×10^9 cm^{-2}).

2.2 EXPERIMENTAL METHODS

2.2.1 Metal Organic Chemical Vapour Deposition (MOCVD)

MOCVD is one of the most popular methods for depositing high quality thin films and has been widely used in fabricating electronic and optoelectronic devices, especially in III-Nitride based commercial devices. Several reasons make MOCVD the most adopted thin film deposition method in the market, such as (1) multiple metal-organic sources are available and different materials can be grown in the same system, therefore a high flexibility (2) no ultra-high vacuum level needed (typically around 10^{-10} torr for MBE), and can operate under atmosphere pressure (3) able to produce very high quality and smooth layers, due to the ability of controlling the growth rate and the uniformity of doping (4) able to grow sharp interfaces and thus facilitates the formation

23

of heterostructure, which is used in most of the optoelectronic devices like LED and Laser diode.

In this dissertation, all the experiments were completed by using a homemade MOCVD system with a vertical design water-cool quartz reactor. Wafers were placed on a 2" SiC susceptor which was sitting on a ceramic tube and heated by using the RF induction heating system. The temperature was monitored by a thermocouple installed under the susceptor and protected by a thin quartz tube, and was controlled by changing the RF value of the RF generator. The reactor pressure was kept constant at 40 Torr during all the growth experiments, Hydrogen (H_2) was used a carrier gas and trimethylaluminium (TMAl), trimethylgallium (TMGa), and ammonia (NH3) were used as the precursors for aluminum, gallium and nitrogen, respectively. For the doping purpose, Disilane (Si_2H_6) and Bis-cyclopentadienyl magnesium (Cp2Mg) was used for n-type and p-type doping respectively.

2.2.2   Characterization Techniques

To characterize the grown material qualities, including its surface morphology, structural properties, optical and electric performances, several well-established characterization methods were used. The extracted information is important for optimizing both single layer crystal quality and the overall structure performance. The working principle and how the measured data can be used in analyzing the material properties in different aspects will be briefly discussed.

a. Optical Microscopy

Two different modes of optical microscopic images, namely, dark field and Nomarski mode can be used to characterize the macro-scale of the sample surface. Nomarski mode is capable of showing a three dimensional image, meaning particles exist on the surface or defects that make a rough surface will display as a 3D image, allowing the surface roughness and contamination condition to be examined. The concept of Nomarski mode also known as Differential interference contrast mode (DIC) is to show a phase contrast image by the recombination of interfered beams, which is accomplished by changing the path length of the incident polarized-beams when they pass through crystal defects or particles. Another frequently used mode is the dark field mode which is useful in exhibiting the pinholes and cracks that scatter the incident beams, showing a bright image, while for the un-scattered portion of the wafer, a dark image will be displayed.

b. Atomic Forced Microscopy

The surface morphology of the grown layers will be evaluated by Digital Instrument atomic force microscopy (AFM), which has a nano-scale resolution and operates in the tapping mode, which overcomes the problems such as distorted data and damaged sample in the contact mode and limited resolution in the non-contact mode. In the tapping mode (also known as intermittent-contact mode) AFM measurement, a micro-cantilever oscillated near its resonant frequent of around 200Hz to 400 kHz, which was driven by a piezoelectric crystal material, approaches the surface until the tip contact the surface; the contact means an existence of repulsive force between the surface atom and

the atom comprising the tip. When the tip scans over the surface, instead of dragging it on the surface like contact mode does, the tip lifts off from the surface and will decrease the oscillating amplitude while passing a height due to a limited space for oscillating or increase the amplitude if there is a hollow. The oscillation amplitude of the tip is measured by the deflection of laser beam detected by a position detector; a feedback system adjusts the space between the sample surface and tip to maintain the amplitude and force on the sample. Figure 2.2 shows the correlation between interatomic force and their distance in different operating mode. For the tapping mode, when the distance between the tip and sample is close enough, the tip will locate in the repulsive force regime and will act like the contact mode and will be able to provide a better resolution, while the tip oscillates off from the surface, the tip will work like non-contact mode locating in the van der Waal attractive force regime, preventing the misinterpreted information.
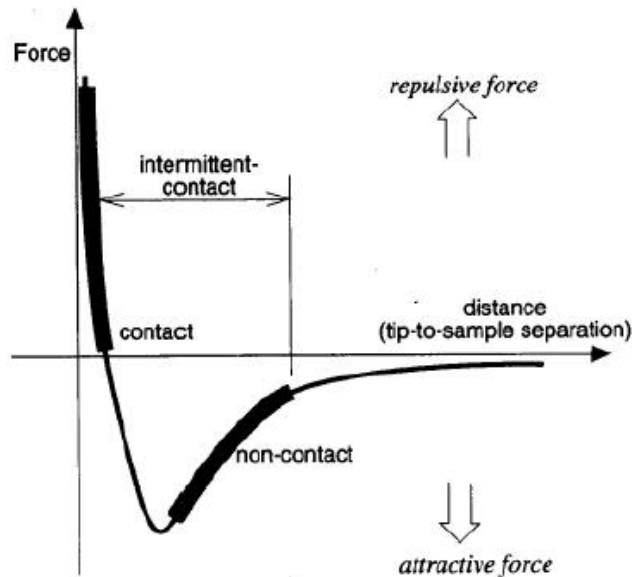
Figure 2. 2 Interatomic forces vs. distance curve. [102]

26

AFM measurement can be implemented in ambient air and no need any sample preparation. In this work, AFM characterization technique will be used to exhibit the surface morphologies such as surface atomic steps, grains, grain boundaries, surface pits, also some numerical analysis such as the root mean square (RMS) of surface roughness, peak to peak distance etc. Figure 2.3 is a AFM image of AlGaN surface with a surface RMS value of 0.6nm, where the atomic steps have been clearly displayed; also from the shape of the crystal grains, which will be more common to be found on AlGaN layers or silicon-doped AlGaN layers as compare to AlN layer, the existence of screw type dislocations in the grains can be easily disclosed. On the other hand, AFM is one of the simplest methods to obtain the dislocation density data from a pre-etched thin film, and this method will be primarily employed to exhibit the dislocation density of the grown samples in this research.
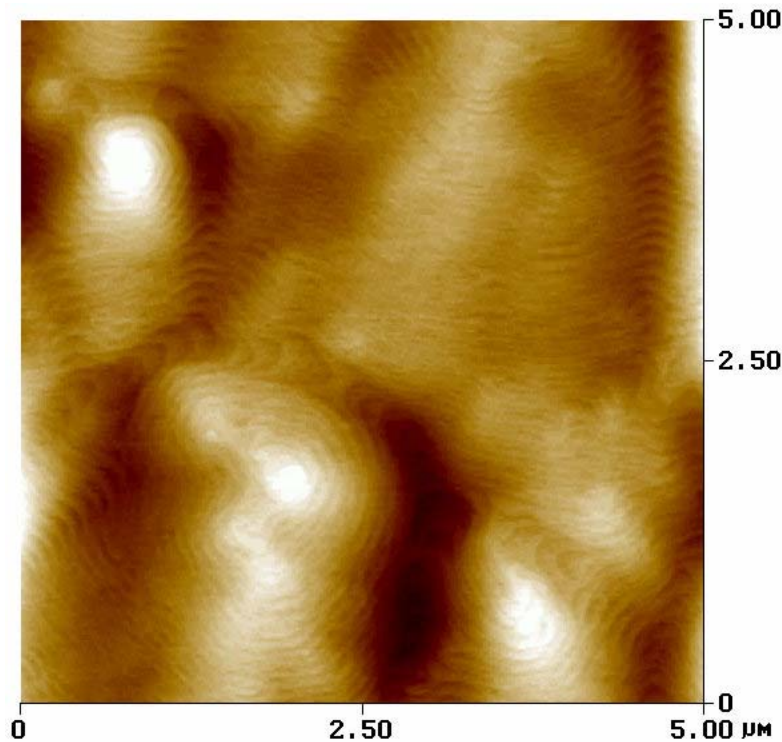
Figure 2. 3 AFM images of AlGaN sample.

c. Etch Pit Density

It is of great interest to measure the dislocation density in thin film as a quality metric. Several destructive and nondestructive methods have been developed to reveal the dislocation density in the AlGaN-based materials. These methods include transmission electron microscopy (TEM), which though require extensive sample preparation time, can exhibit microstructure of dislocations and other defects in not only single layer but also whole LED structure, and is one of the most powerful tool for defects characterization; cathodoluminescence (CL), where the dislocation will be disclosed through a nonradiation process, showing spots on CL image and the dislocation density can be counted. Additionally, defect selective etching process studied with AFM, where the number of etched pits displayed on the AFM-scanned surface is used to find the etch pit density (EPD) by dividing these number by the scanned area, and this EPD is found to be positively correlated or the same to the dislocation density.

The defect selective etching process facilitates the desire to obtain the epilayer crystal quality on the surface, providing a fast dislocation density and dislocation types feedback for the optimization of crystal growth. Several solutions have been used to carry out the defect selective etching or so called orthodox etching, such as molten salts (KOH+NaOH), hot acids (H_2SO_4, H_3PO_4), and vapor phase HCl; each of these solutions with a specific etching process and experiment setup has its pros and cons. In this dissertation defect selective etching by using hot H_3PO_4 acid will be used to evaluate the etch pit density. The etching procedure has been optimized with a series of systematic experiments and the total dislocation density of the experimental data has been confirmed with their TEM data to assure the accuracy of the experiment procedure and condition. A

typical procedure is first to heat the 85% phosphoric acid to around 150°C and slightly stirs the acid to make a uniform temperature, which is detected by an infrared laser thermometer, after the temperature is stable, then dips the sample for 5 minutes, which was cut to an area size of around 1cm× 2cm. After the 5 minutes etching, sample will be removed from the acid and clean with DI water and isopropanol. After the cleaning, 5 to 10 minutes sample baking under a 150°C is need to make sure the sample is dry to prevent any inaccuracy while extracting the image and defects information from AFM. Figure 2.4 is the AFM image of an etched AlGaN sample, which is the same piece of sample shown in Figure 2.3. There are many additional dark spots/pits with different sizes showing on the surface as compare to the Fig 2.3, where no pits have been exposed. The larger size pits which are located at the termination of surface steps are corresponding to mixed or pure screw type dislocations. Also there are some smaller pits positioned within the terraces between steps are considered to be pure edge type dislocations. It is believed that the etching rate that results in the different size is related to the defects energy of each type dislocations. And these defects energies is inversely proportional to the ability of etching; which means the larger the defects energy, the easier the etching ability and rate. Screw type dislocation has larger defects energy than edge type dislocation and thus it is easier for the formation of pits and higher etching rate. To find the etch pit density (EPD), there are 42 pits, including all types dislocation, revealed on the 2μm×2μm (=4×10^{-8}cm^2) AFM image. Take the counted pits number divided by the area, an EPD of 1.5×10^{9}cm^2 is obtained, which indicating the total dislocation density is around 1.5×10^{9}cm^2.
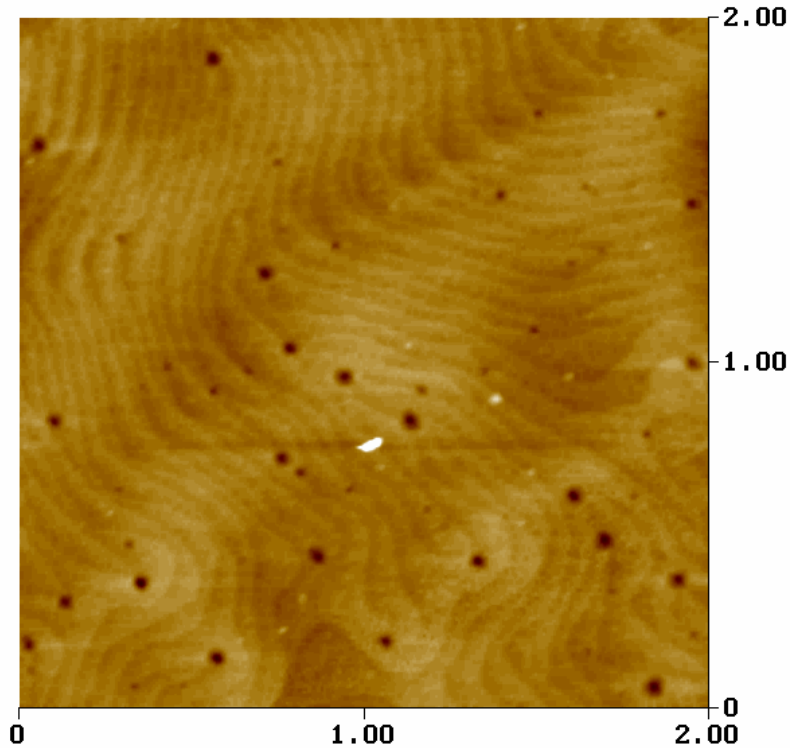
Figure 2. 4 AFM image of defect selective etching.

d. Transmission measurement

The transmission measurement is used to determine the optical absorption edge and is capable of finding the thin film thickness. Before the start of measurement, the background correction procedure is first completed by doing background scanning (or called blank scan) without placing the sample on the stage. During the measurement, light is incident on the tested sample and the transmitted light is expressed as the ratio of the incident light, and thus the percentage of the transmitted light is displayed as a function of the incident light wavelength. The principle of finding the absorption edge is simply adopting the theory of any incident light with a higher energy than the bandgap of the material will be absorbed. The transmission intensity will be greatly influenced by the defects, impurities in the tested sample, as well as the surface morphology; a rough

30

surface may result in an unclear absorption edge. On the other hand, the transmission measurement is also used to fast access the thin film thickness; the concept is depicted in Figure 2.5. Considering a light is incident to the sample, and will be transmitted, reflected, and absorbed partially at each interface of any two different refractive index media. Thus light is reflected back and forth, in the meantime, light transmission and absorption are occurred. From the basic constructive theory, one can easily find many transmission peaks and valleys in a widely scanned wavelength range, typically from 200nm to 800nm. The distance between any of these neighbor peaks or valleys is depend on the light path, i.e. the thickness, and thus by choosing two or more peak wavelength data, the thin film thickness is able to be determined. An optimized equation is used in this work to obtain the thickness information, due to the refractive index is slightly shift at different light energy and is also related to the material absorption edge. Figure 2.6 shows a transmission result of a AlGaN thin film with a absorption edge at 231nm, corresponding to a bandgap energy of 5.5eV and 75% Al content. The average transmission is around 80% which can be calculated from Fresnel equation by using the refractive index of AlGaN about 2.3 and air refractive index of 1. The clear absorption edge indicating a good crystal quality, also clear fringing peaks, which can be used to find the epilayer thickness, indicate the thin film has good optical quality.
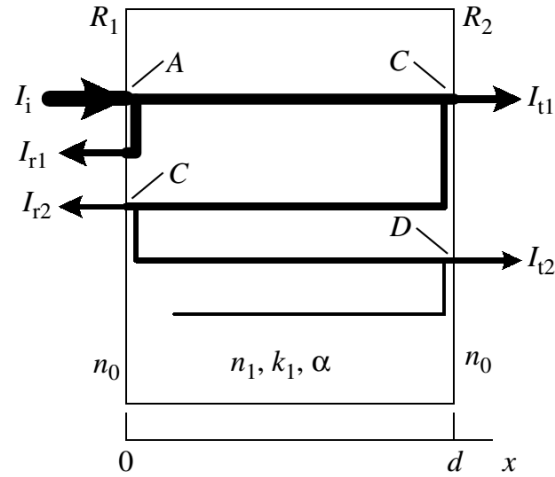
Figure 2. 5 Thin film interference effects. [103]
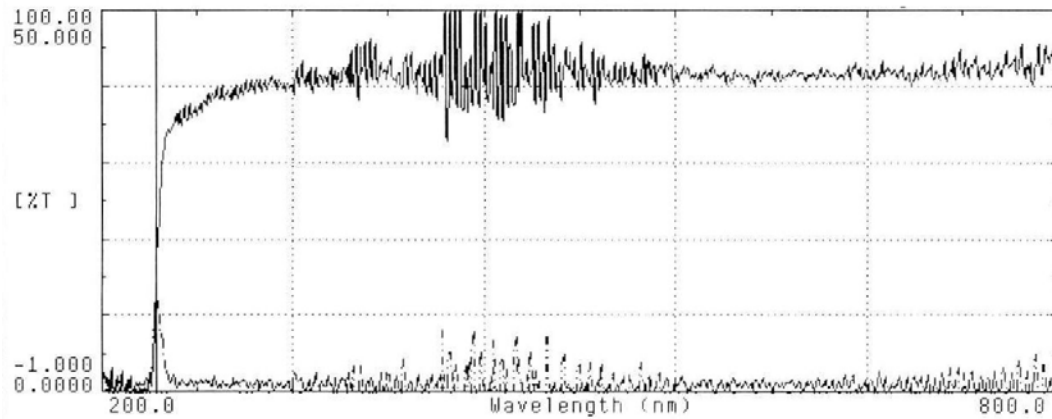
Figure 2. 6 Transmission measurement of AlGaN thin film.

e. Contactless Sheet Resistance

The sheet resistance and its uniformity are obtained by Lehighton contactless sheet resistance mapping system which provides a fast and nondestructive measurement. The working principle is relied on the creation of eddy currents on the tested sample, which is first fixed by two vacuum pumped holes sitting below and then brought into a gap of ferrite cores. The oscillating magnetic field induces the eddy currents in the

32

sample. A feedback system is used to measure the absorption of power which is proportional to the sample conductivity or inversely proportional to its sheet resistance.

f.   Van der Pauw Measurement

Van der Pauw method is a powerful tool for characterizing a thin film electronic properties, such as sheet resistance, resistivity, carrier type, electron and hole mobility, and carrier concentration. Based on Ohm`s law, the Van der Pauw measurement is implemented by making contacts on the corners of a 1cm×1cm square sample and measures the resistance between the contacts as depicted in the Figure 2.7(a). The resistivity is formulated in the equation 2.1, where F is a function of Q and equates to 1 while in a symmetrical sample like samples used in this work, and thus the resistivity formula can be further simplified.

$$\rho = t\frac{\pi}{2\ln 2}\left[\frac{V_{43}}{I_{12}} + \frac{V_{14}}{I_{23}}\right]F(Q), where Q = \frac{R_A}{R_B} \tag{2.1}$$

Combining this Van der Pauw method with the Hall measurement by passing the electromagnetic field through the sample as shown in Figure 2.7(b), the carrier mobility, concentration and carrier type can be found [104].
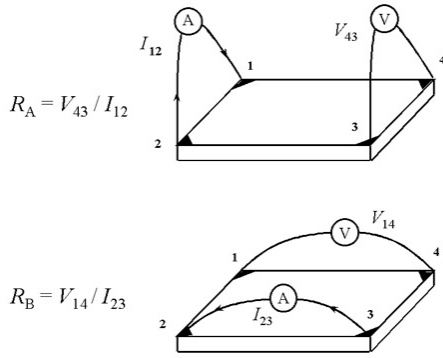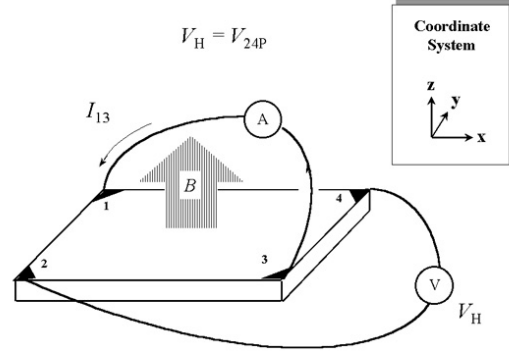
(a)	(b)

Figure 2. 7 Schematic of Van der Pauw Hall Measurement. [105]

g. X-Ray Diffraction

XRD is one of the most common tools used to analyze the crystal quality, due to the fact that it does not damage the sample, no need for sample preparation, and fast response. X-ray diffraction technique gives us information on the crystalline quality which is averaged over the X-ray irradiated area, more information such as stress type, dislocation density, epilayer thickness, chemical composition, lattice constants, lattice mismatch, and strain condition can be obtained by performing X-ray diffraction on the crystal. X-ray used in the diffraction have wavelength lying approximately in the range 0.5-2.5Å. The wavelength of the x-ray source used in this work is 1.54056Å, conducted on a Philips Materials Research Diffractometer.

The principle scheme of high resolution x-ray diffractometer is presented in Figure 2.8(a). The X-ray is first generated from the filament X-ray tube, and then passed through a primary four bounce Ge (022) monochromator to eliminate unwanted wavelengths hitting the sample mounted on the sample holder. The diffracted beams

34

passed through the sample enter the detector; this forms a "double axis" instrument. The measurement can also be done by adding an analyzer crystal before the detector to define the direction of 2theta (2θ) that gives a "triple-axis" instrument with good resolution in 2θ, although this addition will cause a lower intensity output. X-ray diffractometer has four axes which can be scanned: Omega(ω), 2θ, Psi(φ) and Phi(Φ) as depicted in Figure 2.8(b).

X-ray diffraction condition is normally defined by Bragg`s Law, which is shown in equation (2.2), where d is the distance of the Bragg plane, θ is the incident angle, and λ is the wavelength of the incident x-ray wavelength. Figure 2.9(a) shows the Bragg planes and the diffracted beam and illustrates that any incident beam in accordance with Bragg`s law will cause a constructive interference and will be followed by a diffraction condition. Figure 2.9 (b) shows Ewald`s circle moves in the reciprocal space by changing the incident angle. During the movement, if there is any reciprocal lattice point locates on the circumference of the Ewald`s circle, which implicates the occurrence of diffraction at the lattice point or Bragg plane. In this example, the reciprocal lattice point 0004 is on the circumference of this Ewald`s circle; thus the diffraction happened at (0004) plane with a θ incident angle.

$$2dsin\theta = n\lambda \tag{2.2}$$
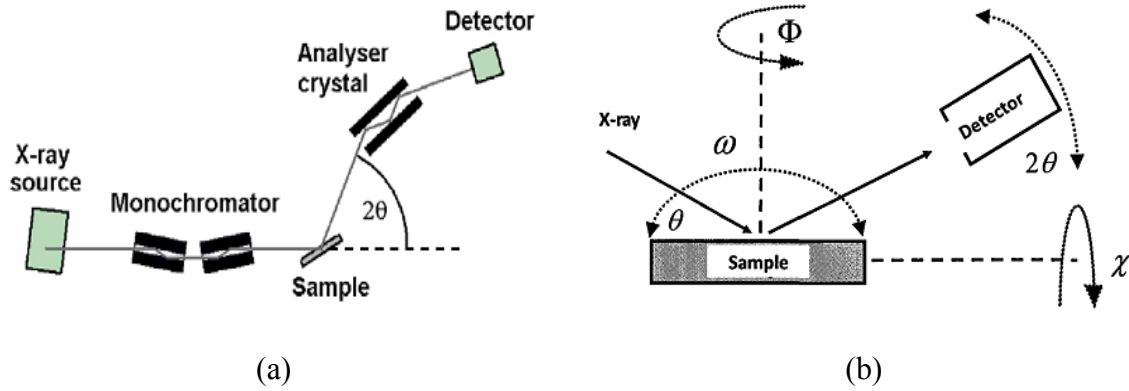
Figure 2. 8 Scheme of high resolution X-ray diffractometer. [106]
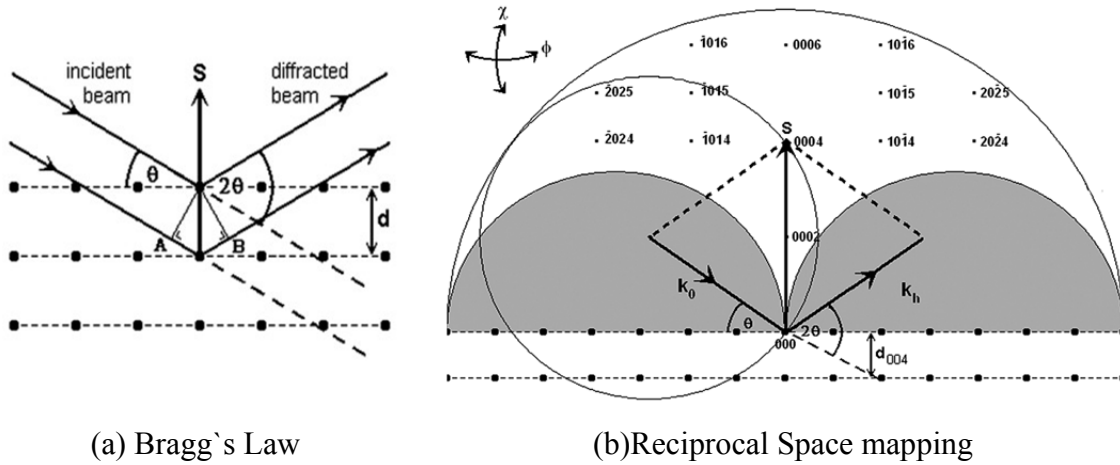
(a) Bragg`s Law   (b)Reciprocal Space mapping

Figure 2. 9 Mechanism of X-ray diffraction. [106]

On-axis and off-axis ω rocking curve are most frequently used to characterization crystal mosaicity. The reason for the broadening of rocking curve is due to the existence of different orientation grains, or due to a grain masaicity. The mosaicity of a mosaic crystal or mosaic block is defined by four parameters: tilt, twist, lateral coherence length, and vertical coherence length. All these parameters are related to the threading dislocations: Screw and mixed type threading dislocations result in tilts of the lattice

planes, which can be evaluated by on-axis ω scan while edge and mixed type threading dislocation measured by off-axis ω scan is related to twists in the lattice planes.

On the other hand, 2θ-ω scan is most employed to unveil the fluctuation in vertical lattice constant, the chemical composition and the thickness of single layer or periodic structures like superlattices or MWQs.

Another type of XRD scan that is highly used to characterize strains in hetero-structures is reciprocal space mapping (RSM), which is carried out by applying ω and ω -2θ scans to fulfill an area scans or 2-axes scan. An ideal reciprocal lattice point should look like a tiny spot on reciprocal space mapping image, but the dimension and the imperfection of the crystal in the tested material will cause a broadening to the reciprocal lattice point. Figure 2.10 exhibits a reciprocal space mapping image of AlGaN layer, providing a fast path to access the structure strain condition. The AlGaN peak is positioned around the center between the fully strained line and the fully relaxed line which means the AlGaN layer is relaxed around 50% and another 50% of compressive strain remains in the layer. Details of the reciprocal space mapping can refer to the Ph.D. dissertation by previous student Dr. Joseph Dion [107].
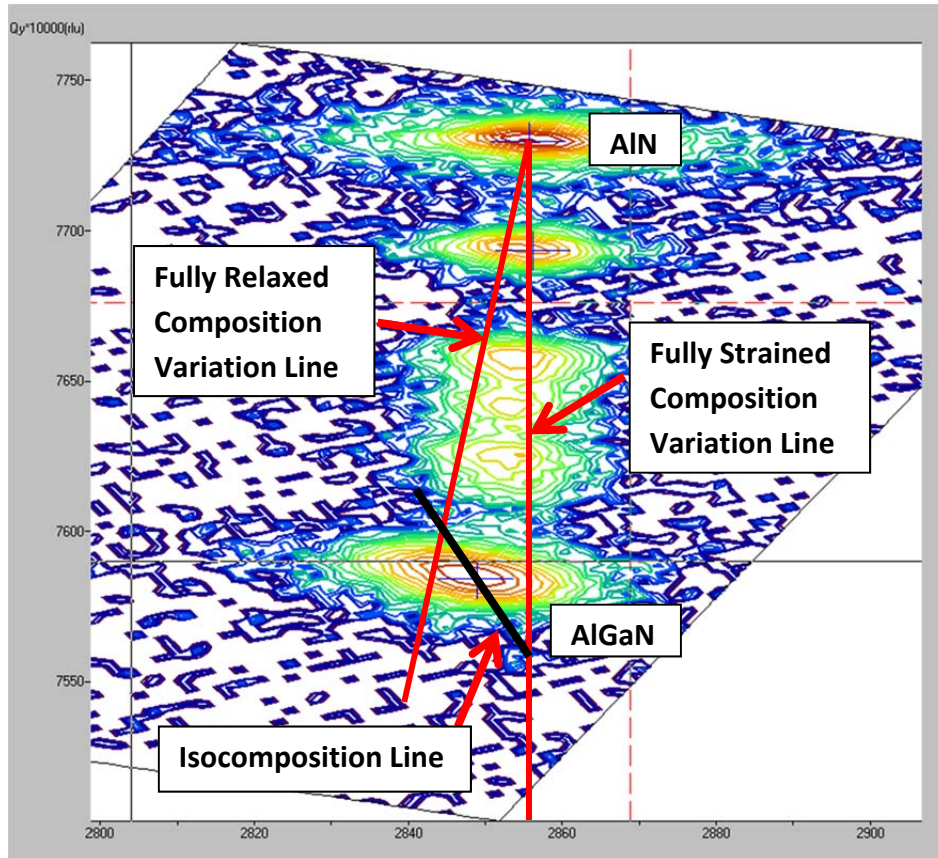
Figure 2. 10 Reciprocal space mapping showing partially relaxed AlGaN layer.

h. Transmission Electron Microscopy (TEM)

The previously mentioned characterization techniques are indirectly interpreting the material defects especially for threading dislocations which is the dominant defect in the III-Nitride based light emitting diode. Transmission Electron Microscopy (TEM) is a reliable technique for analyzing microstructure and dislocations in not only a single layer but also a whole LED structure, with a maximum resolution limit of 1Å. The types of dislocations, the behavior of generation, propagation and termination of dislocations, as well as the vanishing behavior of dislocations by the mechanism of forming dislocation loops can be observed through the technique of TEM. Figure 2.11 shows a TEM cross-

38

sectional image of an AlN layer deposited on sapphire, where dislocations generated from the interface between the sapphire and the AlN nucleation layer, propagating to the sample surface. Some of the dislocations disappear at the dislocation terminations while some are stopped through the formation of dislocation loops.

Though TEM is capable of disclosing the microstructure information, TEM specimens require extensive preparation time; the cross-sectional and plan-view TEM specimens in this study were thinned by mechanical polishing and precision ion milling. Two different High Resolution TEM microscopes were used for the investigation: Hitachi H8000 STEM200 kV (75-200 kV) was used to record lower resolution images, or images with multi-beam condition. For high resolution images that measured under specific diffraction vector or g-vector under two-beam condition were recorded by JEOL 2000F 200 kV with CEOS GmbH with a hexa-pole STEM probe corrector (80-200 kV).
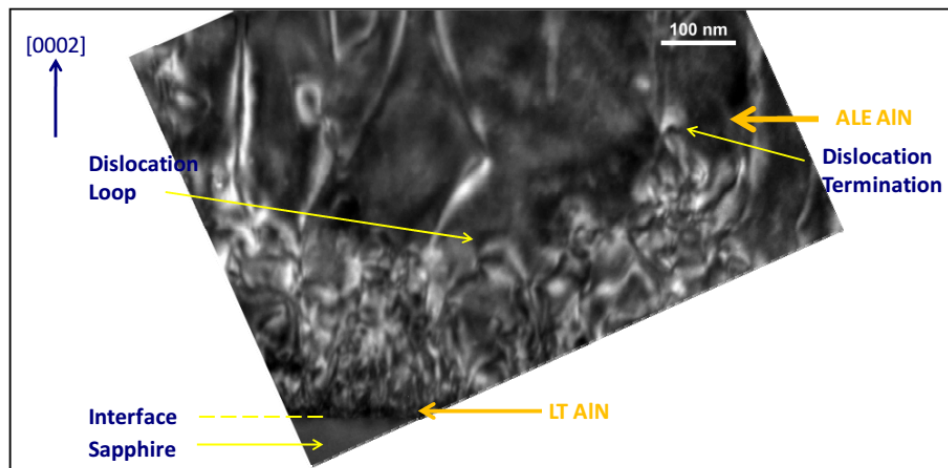
Figure 2. 11 TEM cross section image of AlN on sapphire. [108]

SHORT PERIOD SUPERLATTICE SILICON DOPED HIGH ALUMINUM CONTENT ALGAN

In III-nitride materials, silicon is the most common dopant source for n-type semiconductors where silicon ion is induced to substitute either Al or Ga atomic sites. In the case of n-type III-nitride layers deposited by metalorganic chemical vapor deposition of, silane (SiH_4) or disilane (Si_2H_6) is commonly used as a precursor source for silicon doping. N-type silicon dopant is easily incorporated in low Al content (< 40%) AlGaN layer. However doping in high Al composition AlGaN layer (Al > 40%) remains a challenge. It is well known that silicon doping efficiency decreases with increasing Al content. The difficulty is mainly due to the increase in dislocation density, donor activation energy, and compensation effect as silicon dopant transforms into a deep level [109] [110].

In case of deep UV optoelectronic devices, it is essential to achieve successful doping and high conductivity in high Al content AlGaN layers buffer layers. The n-AlGaN layer for deep UVLED is grown on a higher aluminum content AlGaN template for a lesser light absorption, since the light is extract from the substrate side. A higher aluminum content template (Al composition more than 70%) possess a smaller lattice constant, thus the n-AlGaN layer used for deep UV optoelectronic devices is grown under compressively stress. For AlGaN layers with aluminum composition of 60%, theoretical

critical thickness is around 40nm [111]. Once the thickness of n-AlGaN layer crosses the critical thickness limit, the compressively stress will be relaxed by forming dislocations in the material thereby increasing the total dislocation density in this n-AlGaN layer.

Silicon doping also easily induces edge type dislocation and will lead to a decrease in compressive stress or an increase in tensile stress for tensely stressed layers [112]. This results in a higher surface roughness as well as cracks in the epilayer. Combining the above mentioned silicon doping effects with the typically optoelectronic device crystal structure of nAlGaN, silicon doped AlGaN have been showed a reduction of compressively strain, which was achieved by the inclination of edge threading dislocation. The inclination angle is related to the doping level and was induced by surface roughness during growth [113]. To achieve low dislocation density, and high conductivity in the high Al content crack free AlGaN layer, the methods of controlling strains and creating interface to bend the dislocation for further decreasing dislocation density is proposed in this work and the results are discussed in this and next chapter.

3.1 TEMPLATE PREPARATION FOR N-ALGAN

It is widely known that the threading dislocation, generated from the interface of heterostructures especially in those high lattice mismatch structures, tend to propagate from the base to the surface of the structure and thus low defects and smooth bottom layer is crucial to achieve a low overall defects structure while pursuing high efficient optoelectronic devices. The use of bottom buffer layer can be traced back to 1986, when Amano et al. proposed an AlN buffer layer to improve the crystal quality of GaN film on sapphire. Nowadays, most of the III-Nitride base devices are exerting this bottom layer in order to obtain a high crystal quality structure, including those Nitride-based devices

grown on Silicon substrate. This AlN buffer layer is also critical in determine the overall efficiency in deep UVLED, not only because of it can help to improve the crystal quality, but also it is the only III-Nitride material will not absorb light emitted in the deep UV region. Scores of approaches have been reported to further gain the material quality of this AlN buffer layer such as the growth high temperature AlN, multi- III/V ratio modification, atomic layer epitaxy (ALE) etc.. The influence of low temperature nucleation layer to the material quality of AlN buffer has been studied in my master thesis [108]. The growth of thick AlN buffer layer has also shown effectively in decrease the dislocation density. High quality thick AlN buffer layer has also been published in a PhD dissertation by a previous student by adopting a rough/smooth technique [107]. The AlN buffer layer used in the work will be based on the rough/smooth technique and the material characterization date shown in Figure 3.1, where XRD (102) rocking curve scan relating to the major dislocation in the crystal is as low as 310 arcsec exhibiting a highly crystalline quality, also the 2μm×2μm AFM image shows a smooth surface with RMS value of 0.084nm as shown in Figure 3.2, and a sharp transmission edge at 203nm indicating a good optical transmission in the material, has successfully demonstrated that the AlN buffer layer is suitable in developing high efficiency deep UV LED.
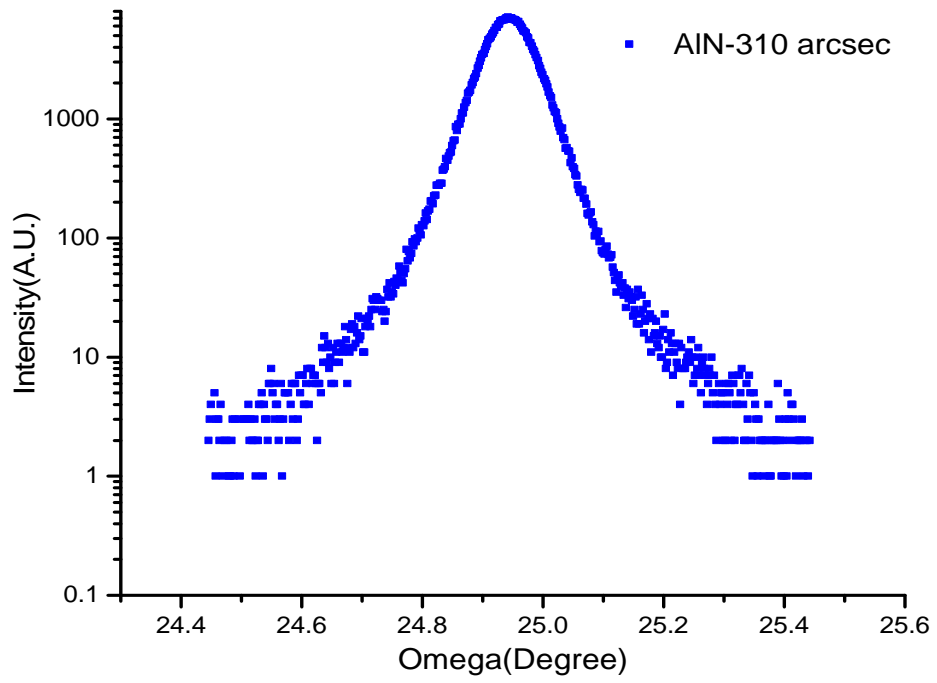
Figure 3. 1 XRD(102) scan of AlN template.
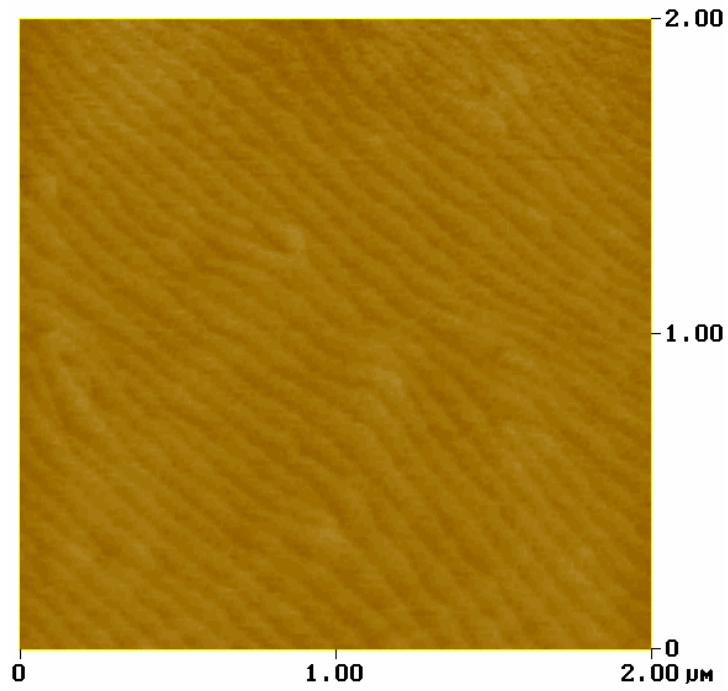
Figure 3. 2 AFM image of AlN template.

Beside the high quality AlN buffer layer, the technique of short period superlattice is also used for preparing high quality template for the subsequent growth of silicon doped AlGaN. Concepts of superlattice layers has been widely used and analyzed in improving crystal quality and strain management in the epitaxial layers. It acts as dislocation filters by the formation of dislocation loops to annihilate threading dislocations, also the design of AlN/AlGaN can effectively release partial of the compressive strain, resulting in crystal quality improved on grown layer and smoother surface. Figure 3.3 shows TEM image of conventional growth nAlGaN layer, where 5-periods of AlN/AlGaN superlattice was mainly acting as screw type dislocation filter by forming the dislocation loops, indicated by white arrows.
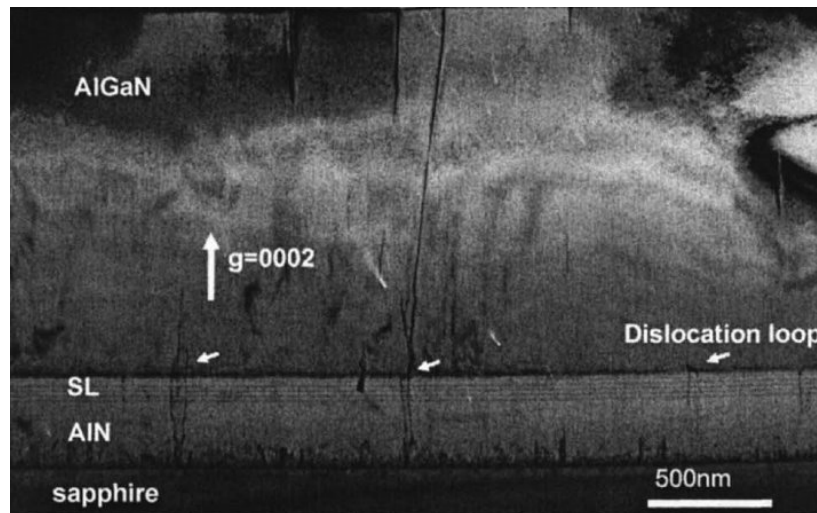
Figure 3. 3 Reduction of threading dislocation by using superlattice layers. [80]

In this study, two kinds of superlattice were used. The first type superlattice is AlN/AlGaN superlattice with the periods of 150 Å AlN layer followed by 80 Å AlGaN. Another type superlattice deposited on the first AlN/AlGaN superlattice is $Al_xGa_{1-x}N/Al_yGa_{1-y}N$ superlattce where the absorption edge was designed to be lower than

250nm for prevention the absorption of deep UV light. By adopting these two-step superlattice techniques on the previously optimized AlN buffer layer, we are able to provide a low defects SL template for exploiting high crystalline quality silicon doped AlGaN. Figure 3.4 shows the transmission data of our SL template with a sharp absorption edge at 235nm indicating the material is suitable for the use of template where deep UV light will pass through. Figure 3.5 exhibits the XRD (002) and (102) scans of the low defects SL template with the FWHM value of 280 arcsec and 370 arcsec respectively. The template surface morphology is shown in Figure 3.6, where many spiral hillocks can been seen on the 5μm×5um AFM scan with a RMS roughness of 0.7nm, indicating the existence of screw dislocations, and is commonly seen in the Ga doped III-nitride layers. The dislocation density of the SL template is characterized by etching pit density (EPD) as shown in Figure 3.7, where the black circles pointed out the etch pits with a number of 13 on this 2μm×2μm AFM scan, giving a EPD of 3×10^8 cm^{-2}.
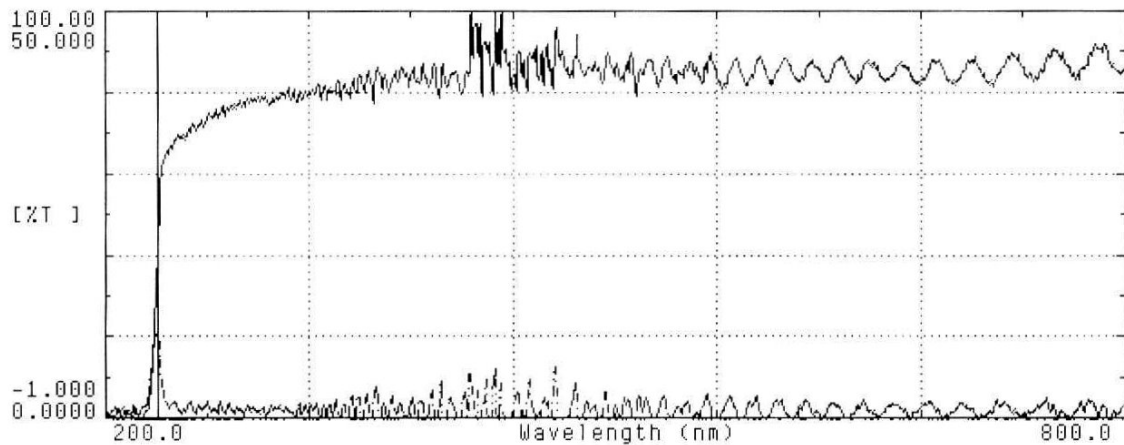
Figure 3. 4 Transmission measurement of SL template.
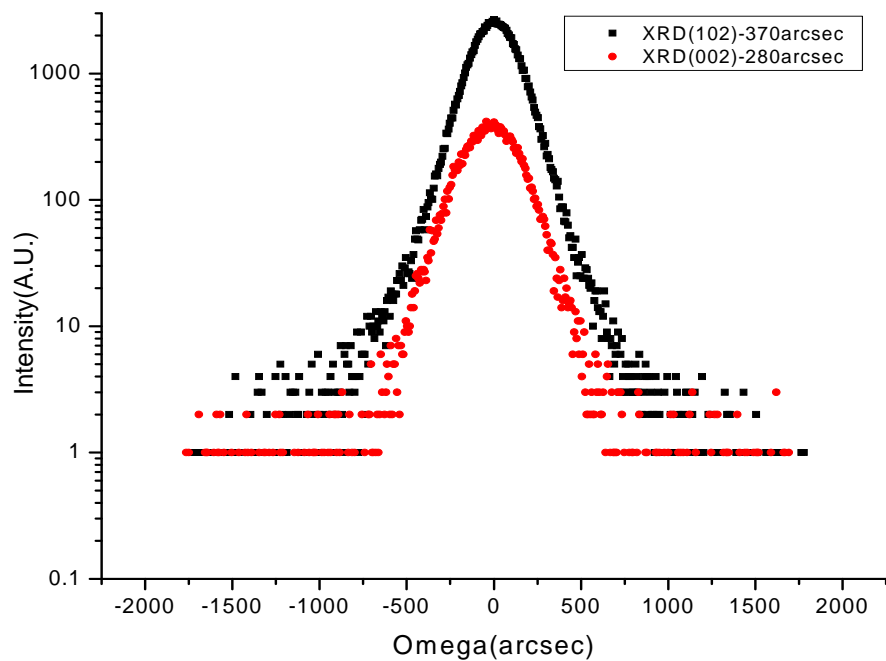
Figure 3. 5 XRD (002) and (102) scans of SL template.
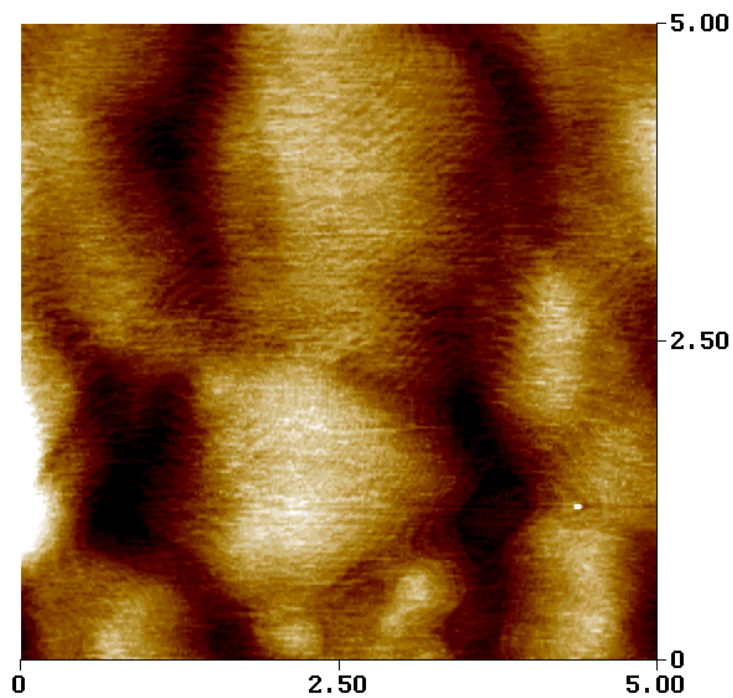
Figure 3. 6 AFM image of SL template.
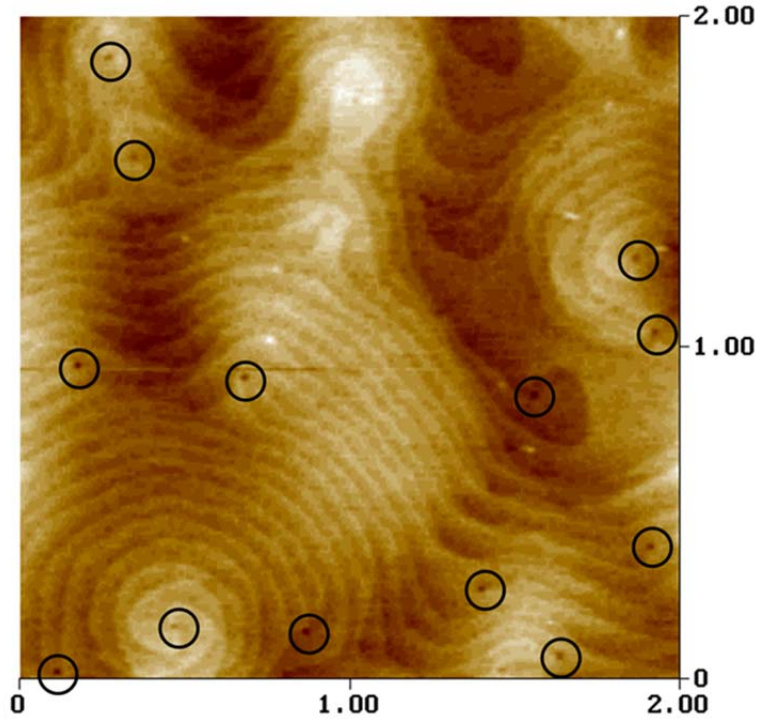
Figure 3. 7 AFM image of superlattice template (EPD~3×10^8 cm^{-2}).

3.2 SHORT PERIOD SUPERLATTICE SILICON DOPED ALGaN

In order to achieve a low defect, high conductivity silicon doped high Al content AlGaN, though many reports point out that increase of Al content will raise the difficulty of silicon doping and limit the crystal quality, a short period superlattice(SPSL) silicon doped AlGaN technique will be employed. Most of the reports use the superlattice technique in the un-doped buffer layers in order to produce a high crystal quality template. Our group first published that the use of superlattice structure can improve the crystal quality, the electronic properties, and thus the optical power in deep UV LED, due to its capability of effectively relaxing stress induced by the lattice mismatch from the heterostructure. In this research, short period superlattice technique is not only used in

47

fabricating a high quality template, but is also used in producing low defect silicon doped

AlGaN for implementing the high efficiency deep UV LED.

3.2.1 Superlattice n-AlGaN on undoped superlattice template

In this work n-$Al_xGa_{1-x}N$/n-$Al_yGa_{1-y}N$ superlattice will be adopted in forming the

nAlGaN, since the conventional used AlN/AlGaN is difficult in silicon doping. In order

to get a suitable n-AlGaN layer for a deep UV optoelectronic, both the x and y of the

aluminum composition have to be well designed to target an absorption edge less than

245nm. In order to maximize the impact of superlattice technique, the lattice constant of

the two interlayers for forming the superlattice period have to be designed with as large a

difference as possible, namely AlN(x=1) and GaN(y=0). However, AlN layer is difficult

in doping, and the growth condition for growing smooth AlN and GaN has a large

difference, thus a compromised solution has been proposed. Instead of using AlN/GaN

superlattice, n-$Al_xGa_{1-x}N$ layer with 35% of Al composition and $Al_yGa_{1-y}N$ layer with

80% of Al composition are introduced to compose the superlattice n-AlGaN, also the

growth condition of both nAlGaN layers has been pre-optimized for getting a smooth

surface. In order to prevent the deep UV light absorption especially from the low Al

content layer, the thickness of each layer is designed by the theoretical absorption

equation (Beer–Lambert law) as shown in Eq 3.1, as well as the experimental setup,

where AlN/AlGaN was used to provide a more accurate absorption edge, giving an

optimized thickness of around 20A with an average absorption edge of 237nm. Figure 3.8

exhibits a quasi-sharp absorption edge of the calibrated AlN/AlGaN layer, indicating the

design of nAlGaN layer with 35% Al content with a thickness of 20A is suitable for use

in forming deep UV light absorption free n-$Al_xGa_{1-x}N$/n-$Al_yGa_{1-y}N$ superlattice.

$$I = I_0 \times e^{-\alpha x} \tag{3.1}$$

, where α is the absorption coefficient, x is the layer thickness.
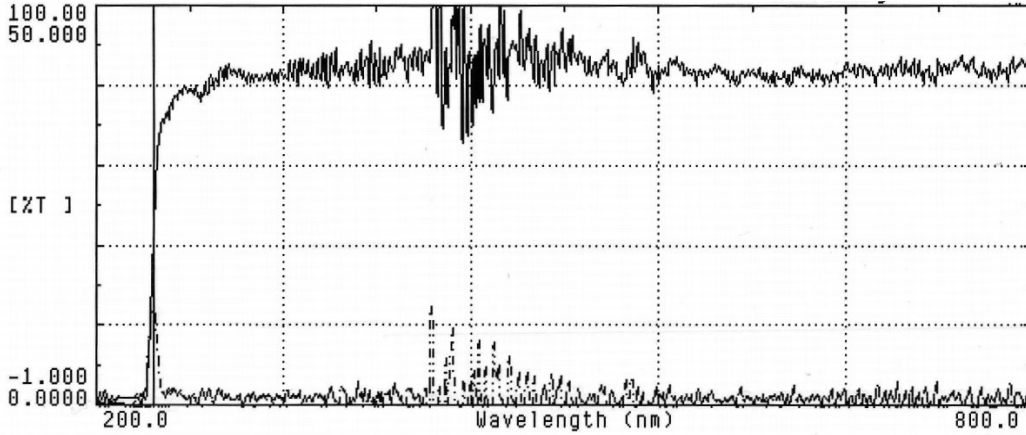
Figure 3. 8 Absorption edge calibration of AlN/AlGaN superlattice.

The n-$Al_xGa_{1-x}N$/n-$Al_yGa_{1-y}N$ superlattice is accomplished by using the above pre-optimized, calibrated AlGaN layers with the period thickness of around 40A and the same doping level as the conventional nAlGaN. The total superlattice nAlGaN thickness is preposely engineered to be half as thick as the conventional nAlGaN, due to the fact that our custom built MOCVD system is adopting a single metalorganic loop, which require longer stabilization time as compares to double or multiple loop design for the mass flow controller (MFC) and pressure controller to prevent the damage of the device itself while changing the metalorganic source flow and pressure condition. Whereas the longer stabilization time will increase the total growth time, it also may influence the epilayer surface, due to surface decomposition and diffusion, which is crucial for developing short period interlayers requiring sharp interface. In the experiment results,

the comparison data to the conventional nAlGaN and superlattice template, as well as the mechanism of decreasing defects will be discussed below.

Figure 3.9 first reveals the transmission characteristic of the superlattice n-AlGaN where a clear absorption edge of 251nm is shown. The results agree with our design by using 40A thick of n-Al$_x$Ga$_{1-x}$N/n-Al$_y$Ga$_{1-y}$N superlattice, where x=35% and y=80%, and meeting our requirement of the targeted nAlGaN layer with about a 250nm absorption edge. The surface morphology is characterized by 2μm×2μm AFM scan as shown in Figure 3.10 with a RMS roughness of around 0.34nm. The smooth surface consists of many two dimensional steps and no surface pits or large opening was seen. Moreover, unlike the surface of conventional nAlGaN (Figure 2.3), this superlattice n-AlGaN did not show spiral hillock on the surface, though a small portion of steps intersection were seen, indicating larger crystal grains and thus improved surface morphology. The sheet resistance of the sample is approximately 273Ω/□, which is higher than the conventional nAlGaN due to the decreased thickness, and can still be used in deep UV LED fabrication.
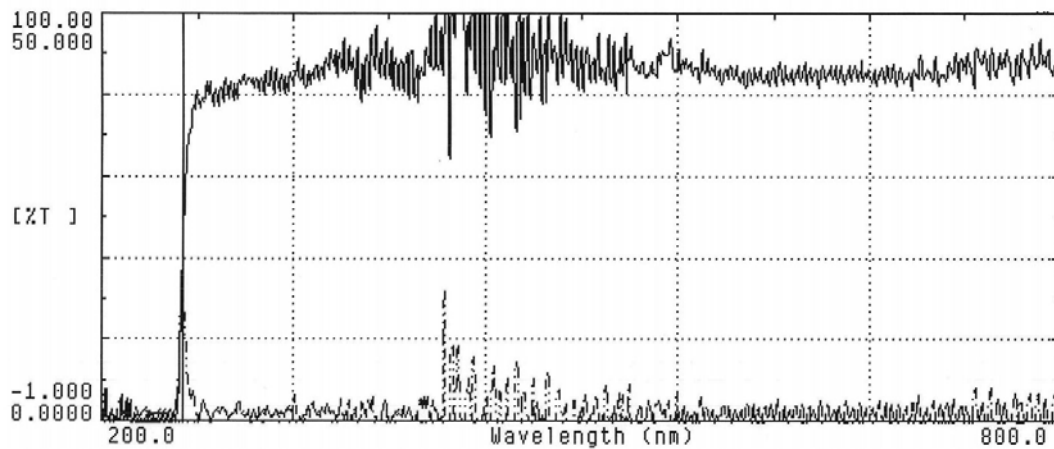
Figure 3. 9 Transmission measurement of superlattice nAlGaN.

50
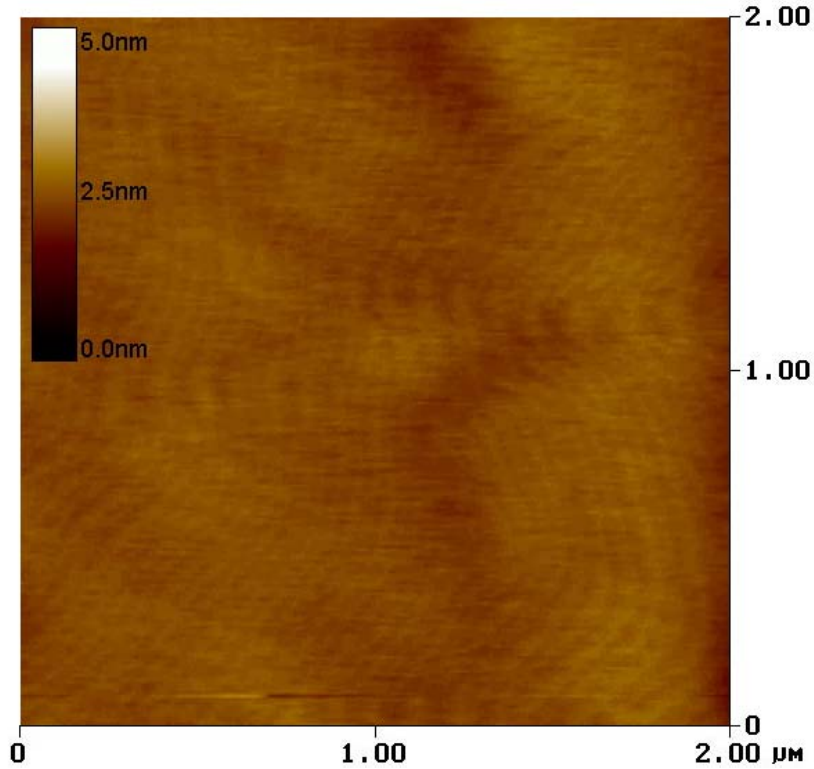
Figure 3. 10 AFM image of superlattice nAlGaN.

The crystal quality characterization has been carried out by XRD (002) symmetric scans and (102) asymmetric scans, which related to the screw-type dislocation and edge-type dislocation, respectively. A comparison diagram of XRD (002) scans of the SL template, conventional nAlGaN, and superlattice nAlGaN is shown in Figure 3.11. The FWHM value has dramatically decrease from 847 arcsec for conventional nAlGaN, to 257 acesec for the proposed method, namely, superlattice nAlGaN, while the value doesn't differ much between the SL template and the SL nAlGaN layer. XRD on-axis rocking curve scan is related to the tilt of crystal grains and thus the screw type dislocation. The on-axis XRD scan suggests that the screw type dislocation has been largely decreased by adopting the superlattice nAlGaN. The XRD (102) asymmetric scan, revealing the grain twist as well as the edge type dislocation, in Figure 3.12 exhibits

higher FWHM values for both nAlGaN structure than the superlattice template. This indicates that silicon doping degrades the material crystal quality and corresponds with the literature reports that the superlattice technique is effective in filtering screw type dislocation and not sensitive to the edge type dislocation.
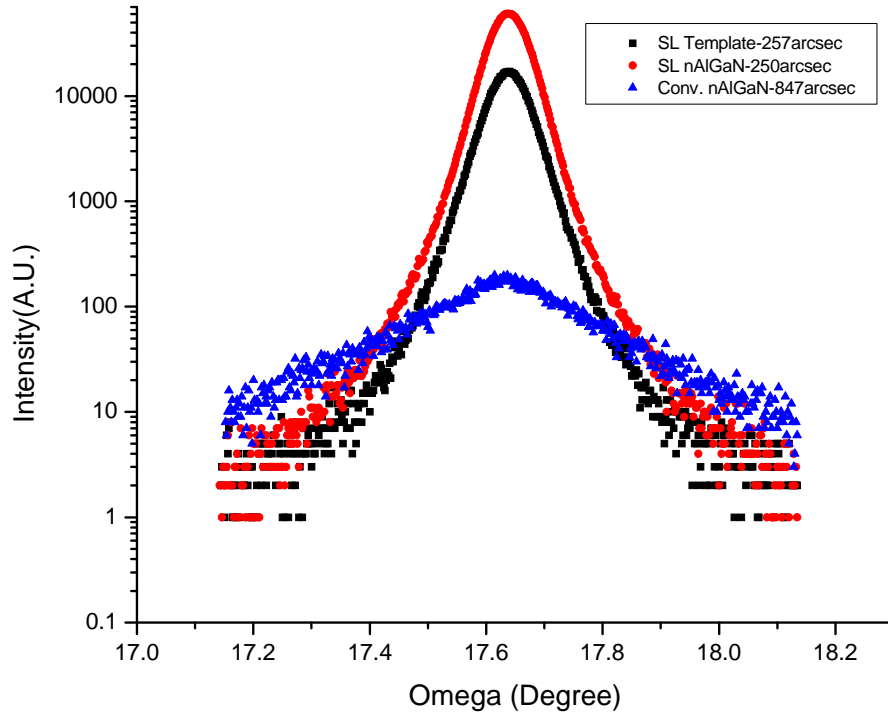
Figure 3. 11 XRD (002) scan of superlattice nAlGaN.
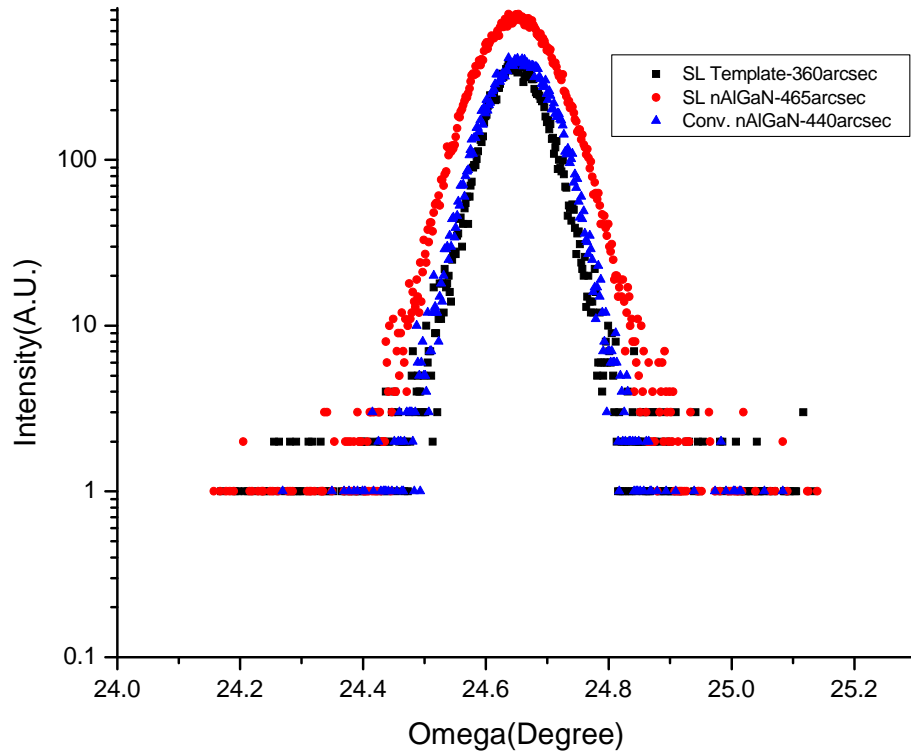
Figure 3. 12 XRD (102) scan of superlattice nAlGaN.

The dislocation density of the superlattice nAlGaN layer is characterized by the etch pit density (EPD) on the 2μm×2μm AFM image as shown in the Figure 3.13. The dislocation density has decreased by a factor of four to around $2.5 \times 10^8 cm^{-2}$ as compared to the conventional nAlGaN layer, whose dislocation density is around $1 \times 10^9 cm^{-2}$ to $5 \times 10^9 cm^{-2}$. A Decrease of the screw type dislocation may be the main reason leading to the improvement of crystal quality, as predicted by the XRD on-axis scan, which may attribute to strain relaxation by adopting superlattice technique in the nAlGaN layer. Figure 3.14 introduces XRD reciprocal space mapping on (105) plane for the SL nAlGaN and conventional nAlGaN, the lateral correlation length and mosaic spread of the SL nAlGaN is 2724Å and 224s, respectively, also 1332Å and 276s for the

conventional nAlGaN. The results suggest a larger grain size and a lower tilt of the crystal grain. A schematic for both nAlGaN strained lines based on the RSM is depicted in Figure 3.15, where the dot red straight line represents the fully strained line. The more the strained relaxation occurs, the larger the angle between the stained line and the fully strain line. The SL nAlGaN is showing **20%** more strain relaxation than the conventional one, which may explain the decreased screw dislocation and thus improved material quality, since fewer defects will be generated to release the strain in the layer. A high quality n-type AlGaN layer on SL template has been achieved by adopting $n\text{-}Al_xGa_{1\text{-}x}N/n\text{-}Al_yGa_{1\text{-}y}N$ superlattice technique, reaching a low dislocation density of $2.5 \times 10^8 cm^{-2}$, RMS roughness of 0.34nm, and sheet resistance of $273\Omega/\square$.
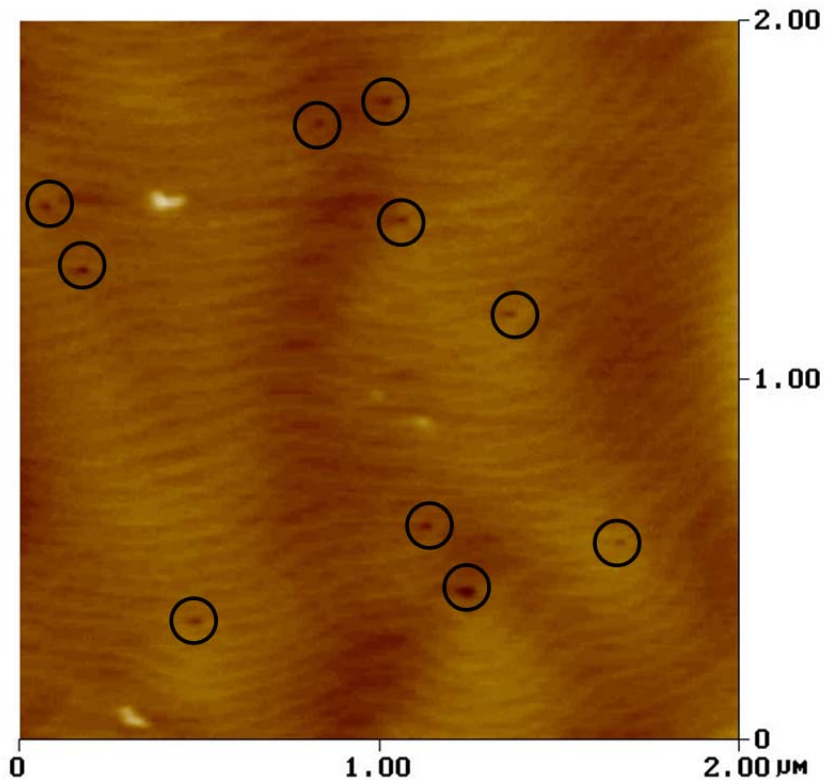
Figure 3. 13 AFM image of superlattice nAlGaN (EPD~2.5×10^8 cm^{-2}).

(a) SL nAlGaN   (b) Conv. nAlGaN
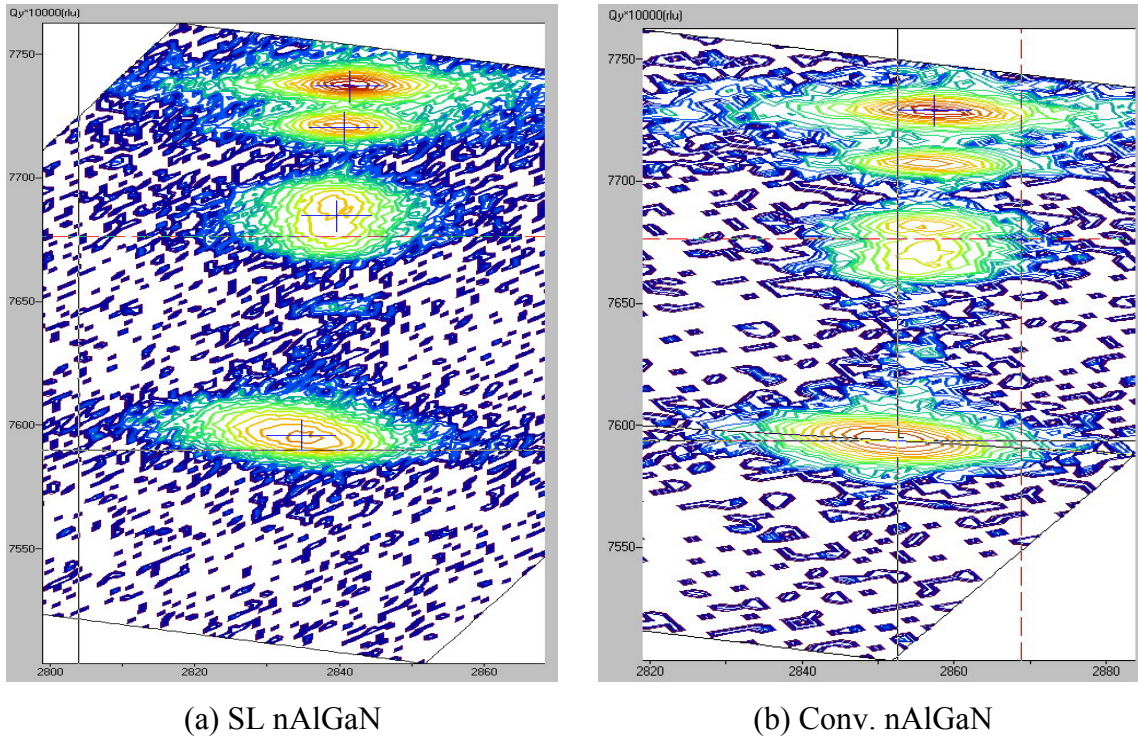
Figure 3. 14 XRD Reciprocal space mapping.
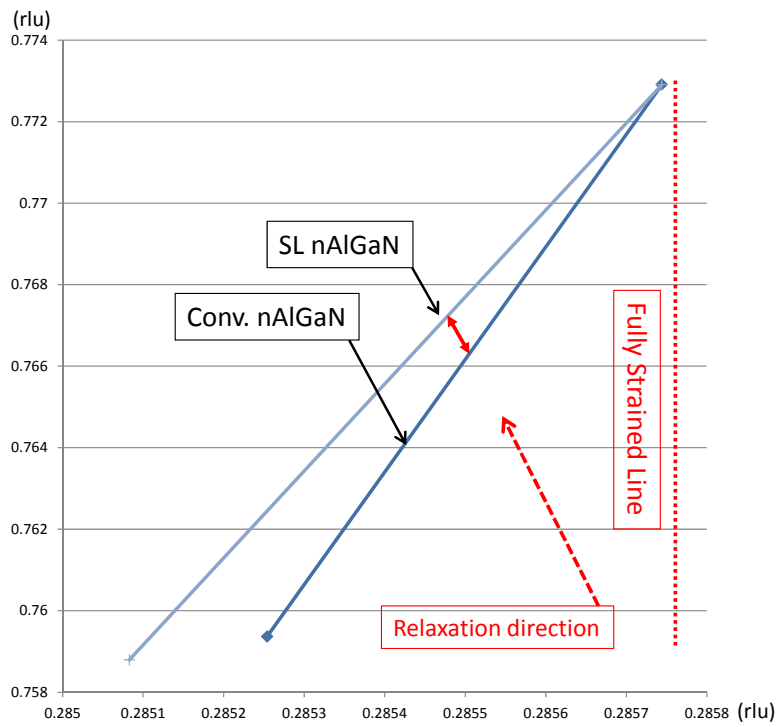
Figure 3. 15 Strain relaxation of superlattice nAlGaN.

3.2.2 Developing Superlattice n-AlGaN on AlN template

Instead of growing the SL n-AlGaN on SL template, in this section, the SL n-AlGaN will be directly deposited on a high quality AlN template. Most of the reports are adopting an un-doped superlattice template as a dislocation filter layer by the mechanism of strain relaxation. However, the extra superlattice layer will dramatically increase the overall growth time, and thus the unit cost of deep UV LED wafer will be increased. It is possible to develop the SL n-AlGaN on AlN template, since the proposed approach of SL n-AlGaN has combined the superlattice concept in the n-AlGaN and is able to show an improved crystal quality through a further strain relaxation. The growth conditions of the SL nAlGaN on AlN template remain the same as the previous SL nAlGaN growth conditions described 3.2.1, except 25% increased layer thickness for the purpose of lowering the sheet resistance.

The transmission characterization is shown in the Figure 3.16 with a slightly higher absorption edge of 255nm, where the transmission fraction has decreased from around 80% to 70%. Both phenomenon may be caused by more incorporated Ga atoms and increased growth rate due to the removal of the SL template. The SL nAlGaN with this absorption edge and transmission is still capable of use in developing deep UV LED. Because of the 25% increased thickness, the sheet resistance of the SL nAlGaN layer has dropped to an average of 212Ω/□ as shown in the Figure 3.17 studied by the sheet resistance mapping, showing a high uniformity of doping in the layer. The sheet resistance value also shows a 22% decrease as compared to the nAlGaN sample in 3.2.1, revealing a well match with the resistance formula ($R = \rho \frac{l}{t \times w}$). The small error between 25% and 22%, may attribute to a small change of electron mobility in the layer.

56
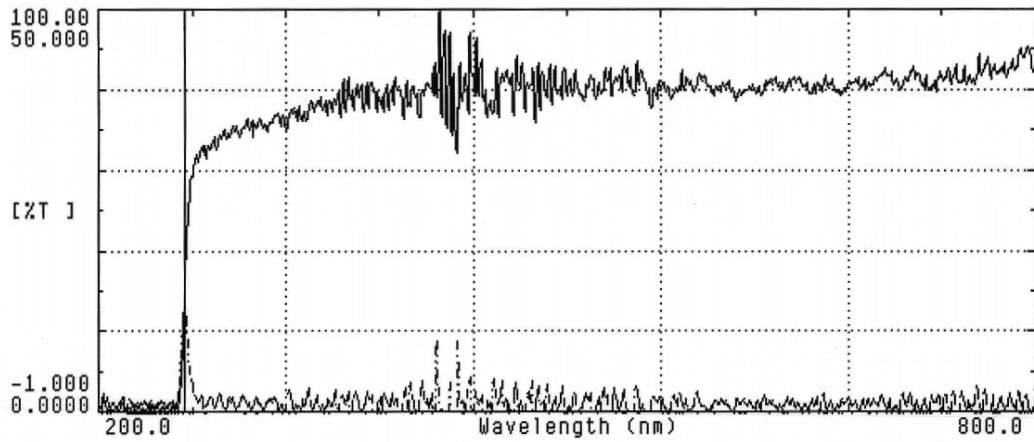
Figure 3. 16 Transmission measurement of superlattice nAlGaN on AlN template.
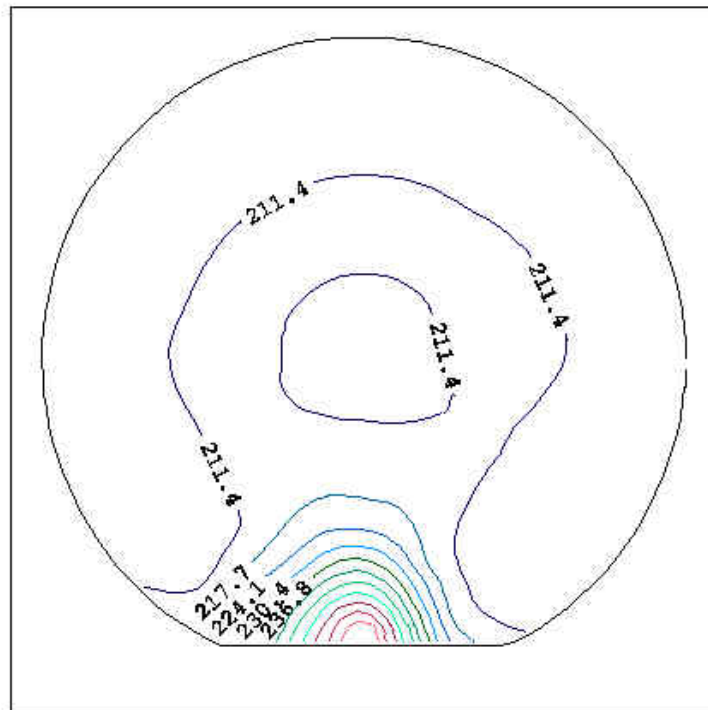
Figure 3. 17 Sheet resistance mapping of superlattice nAlGaN on AlN template.

The crystal quality has been carried out by the XRD (002) scan and (102) scan for revealing the information of screw type dislocation and edge type dislocation, respectively. The comparison diagram of the XRD (002) scans of the SL nAlGaN on AlN,

SL nAlGaN on SL template and the conventional nAlGaN is shown in the Figure 3.18. Although the removal of the SL template did cause a 15% increase of the FWHM value to the SL nAlGaN, the FWHM value of 294arcsec is still three times lower than the conventional one. Strong evidence of the concept of combining the superlattice technique in the nAlGaN is shown from this comparison diagram. It is predictable that the XRD (102) scan should not show much improvement, since the superlattice technique is reported not effective in filtering edge-type dislocation as shown in Figure 3.19, where the FWHM values are not much different from the three samples.
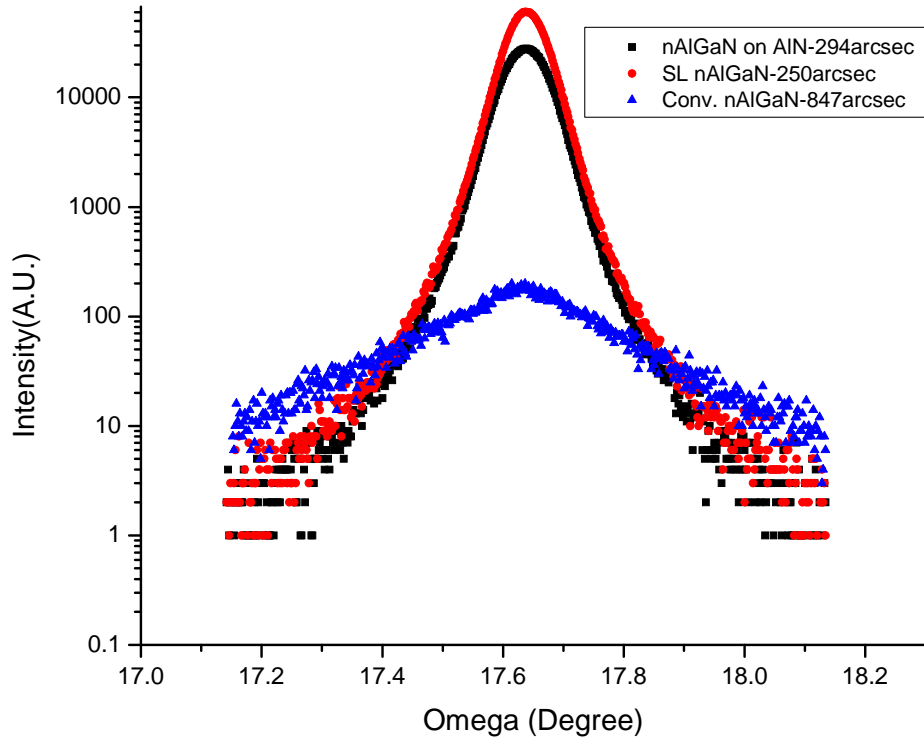
Figure 3. 18 XRD (002) scan of superlattice nAlGaN on AlN template.
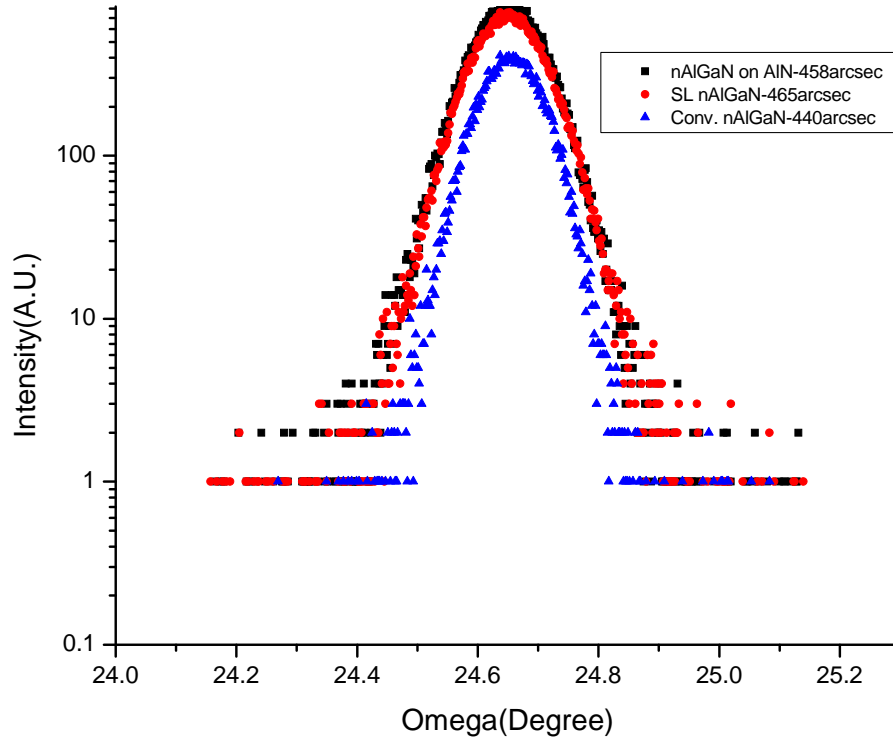
Figure 3. 19 XRD (102) scan of superlattice nAlGaN on AlN template.

Figure 3.20 exhibits the 2μm×2μm AFM image of the etched SL nAlGaN. Around 15 etched pits are found on the 2μm×2μm scan area, representing an EPD of $3.75 \times 10^8 cm^{-2}$, which is close to the previously reported EPD of the SL nAlGaN $(2.5 \times 10^8 cm^{-2})$ on SL template and is dramatically decreased from the conventional nAlGaN $(1.2 \times 10^9 cm^{-2})$. The EPD data degree with the XRD data and again show that the design of combining the superlattice concept in the nAlGaN and removing the commonly used superlattice template is promising in developing low cost, high efficient deep UV LED. Like other superlattice buffer reports, we attribute this improvement of the crystal quality to the relaxed strain in the crystal structure. The XRD RSM scan is shown in Figure 3.21(a), where the lateral correlated length is 1872Å and the mosaic spread is 226s. A comparison diagram in Figure 3.21(b) is used to explain the relaxed

59

strain in the SL nAlGaN directly on AlN. It is reasonable that the SL nAlGaN on AlN has more strain as compared to the SL nAlGaN on SL template since the SL buffer was working as a strain relief layer. Particularly, the conventional nAlGaN relaxation line is only used as a baseline to express a close relaxation degree of the SL nAlGaN on AlN, proving the superlattice nAlGaN is effective in combining the function of strain relaxation, and cannot be used to compare the influence of the defects inside the layers due to the different structure of the two samples.
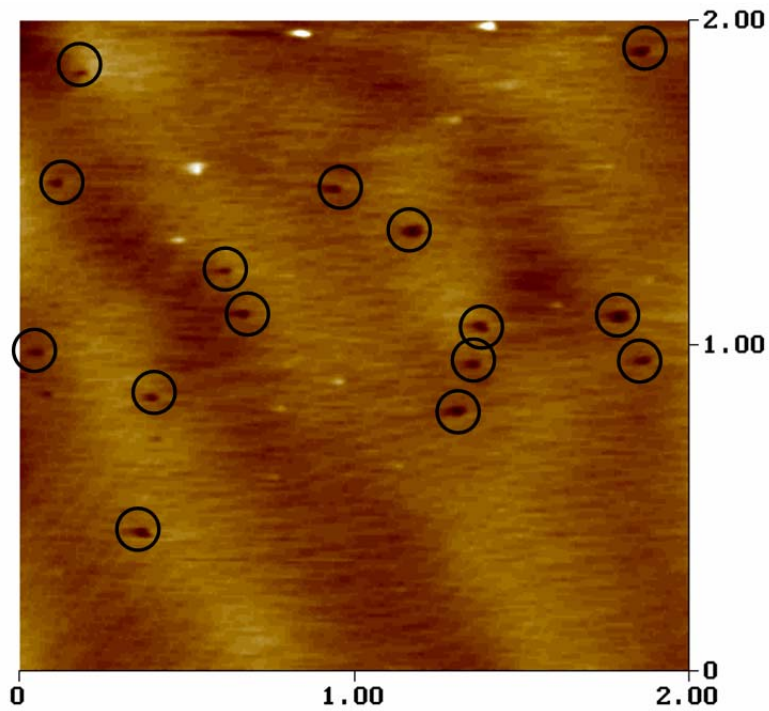
Figure 3. 20 AFM image of superlattice nAlGaN on AlN template (EPD~3.75×10^8 cm^{-2}).

(a)　　　　　　　　　　　　　　(b)
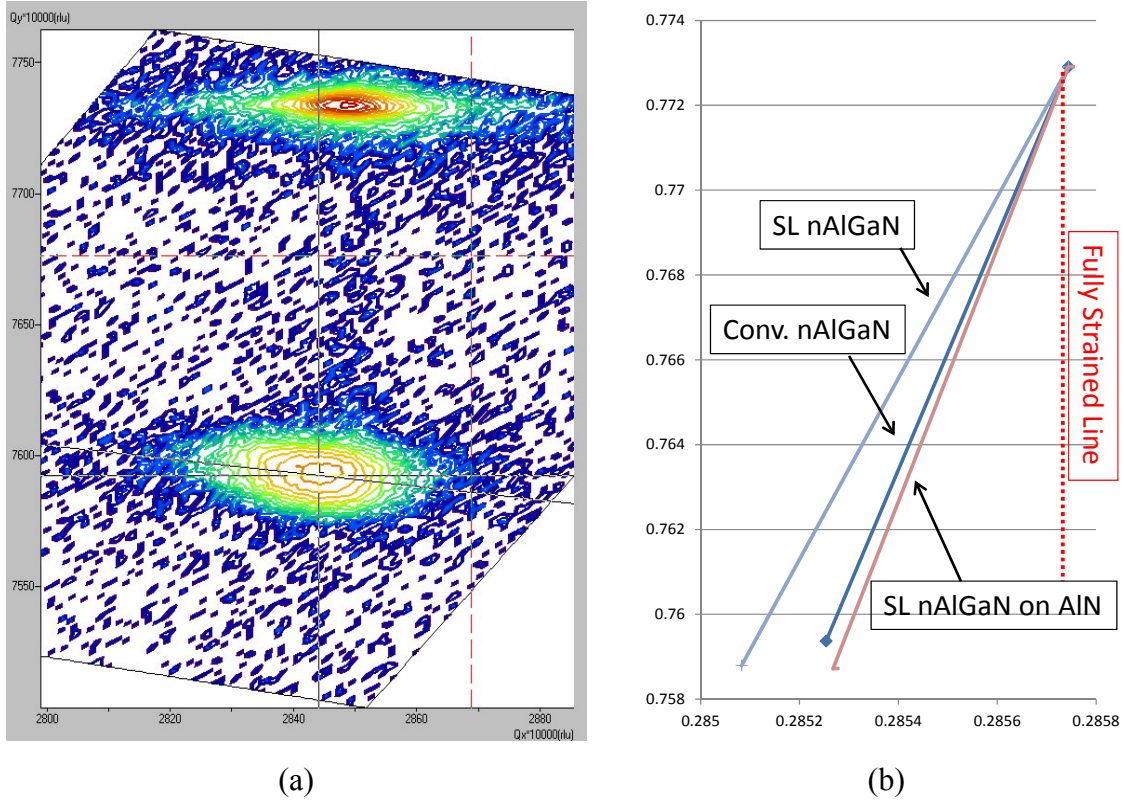
Figure 3. 21 XRD Reciprocal space mapping.

To conclude, the approach of n-Al$_x$Ga$_{1-x}$N/n-Al$_y$Ga$_{1-y}$N superlattice has been proposed to replace the conventional nAlGaN as an electron cladding layer for developing high efficiency deep UV LED. The proposed method is showing a dramatic improvement of the crystal quality with an EPD as low as $2.5 \times 10^8 cm^{-2}$. Additionally, the same approach is used to directly deposit on the AlN template, instead of SL template, to reduce the unit cost of the wafer. A low defects SL nAlGaN on AlN was achieved with an EPD of $3.75 \times 10^8 cm^{-2}$, indicating this approach is promising in fabricating high efficiency, low cost deep UV LED. Table 3.1 summarizes the XRD and EPD characterization data of the proposed approach on different template and the conventional nAlGaN.

Table 3.1 Comparison of SL nAlGaN and Conv. nAlGaN

	Conv. nAlGaN	SL nAlGaN	SL nAlGaN on AlN
XRD (002) scan (arcsec)	847	250	294
XRD (102) scan (arcsec)	440	465	458
Lateral Correlation Length (Å)	1332	2724	1872
Mosaic Spread (s)	276	224	226
EPD (cm^{-2})	1.2×10^9	2.5×10^8	3.75×10^8

CHAPTER 4

SILICON DOPING MODULATION ALGaN

In this chapter, a new approach, silicon doping modulation technique, will be demonstrated to form low defect and high conductivity nAlGaN layer. In the problem identification section, silicon doping is the major problem causing degradation to the epitaxial crystal quality as well as the increased roughness of the layer surface due to the extra impurities introduced into the atomic structure generating additional defects or energies to the lattice. It is inevitable in inducing the silicon impurities to the structure, since silicon ion is the most effective doping source for forming n-type III-Nitrdie semiconductor. However, some reports have shown that the roughen surface resulted by silicon doping may be the major reason causing inclination of treading dislocations. The inclination angle may be influenced by the growth condition such as the growth temperature, the growth rate, the lattice mismatch degree as well as silicon doping level. The larger the bending angle of the threading dislocation, the higher the possibility of the dislocation to cancel each other by forming a dislocation loop or to bend to the basal plan preventing its propagation to the on grown layer.

The silicon doping modulation technique is carried out by simultaneously flowing NH_3, TMA, TMG into the reactor for the growth of AlGaN layer, the growth conditions such as metal organic flow, carrier gas flow, growth temperature and reactor pressure are kept the same as the condition mentioned the conventional nAlGaN, except a pulsed flow

of silane precursor is used instead of constantly flowing of silane source. A schematic

diagram is shown in Figure 4.1. Since the silicon doping has shown to bend the threading

dislocation by roughing the surface, a pulsed silicon doping is expected to bring multiple

interfaces to the structure, increasing the inclination angle and thus increasing the

probability of dislocation annihilation by forming dislocation loops. A series of

experiments are designed to optimize the crystal quality and the conductivity of the

nAlGaN layer. The effects of different silicon doping pulse cycle (On and Off), silicon

doping level and the nAlGaN thinkness on the material properties such as dislocation

density, sheet resistance, surface morphology etc. will be investigated.
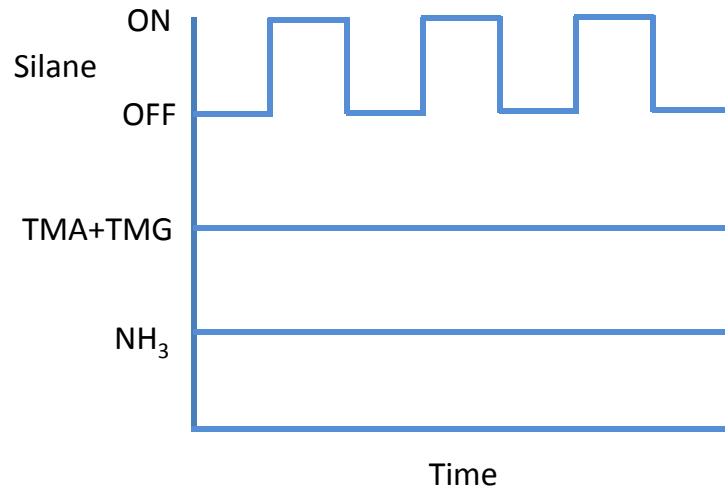
Figure 4. 1 Precursor flow time for silicon doping modulation AlGaN.

4.1 OPTIMIZATION OF SILICON DOPING PULSE CYCLE

To understand the effect of silicon pulse cycle, two n-type $Al_{0.60}Ga_{0.40}N$ samples

were grown. The growth time, temperature, pressure and precursor flows were

intentionally kept same to get a similar thickness and cutoff wavelength and the n-AlGaN

samples were grown on optimized high quality undoped superlattice template with a low dislocation density of 3×10^8 cm^{-2} the same SL template prepared in the previous to decrease the experiment error. Sample A was grown with a si-pulsed cycle of 12 seconds, where the silane 'ON' time is 6 seconds and 'OFF' time is 6 seconds. Sample B was having a 9 second pulsed cycle with silane 'ON' time of 6 seconds and 'OFF' time of 3 seconds. The thickness of all the n-AlGaN samples are around 1um and cutoff wavelength is around 250nm. Transmission spectra of sample A is shown in Figure 6, where a high wafer transparency of 80% was reached and the clear fringing peaks indicate a good optical quality, a similar absorption edge and transparency for sample B.
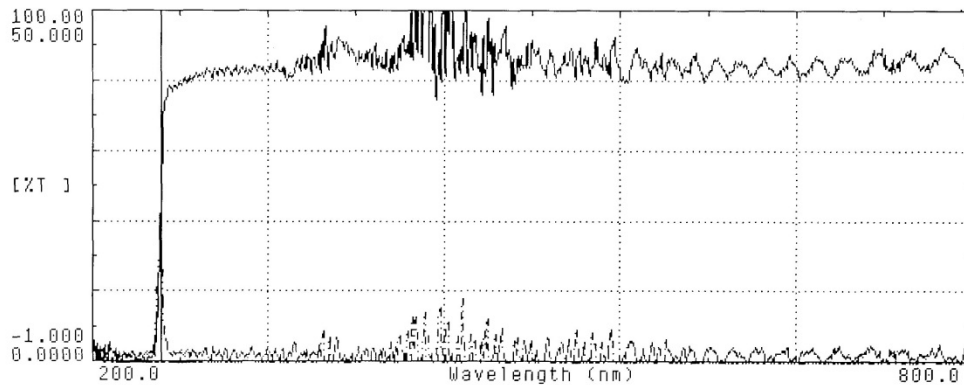
Figure 4. 2 Transmission spectrum of silicon doping modulation AlGaN for Sample A.

Figure 4.3 shows the X-ray (002) ω-scan rocking curve of the superlattice template and both sample A and B. Both of the samples shows an increment of X-ray FWHM from 257 arc-seconds to 356 and 358 arc-seconds for Sample A and Sample B respectively. The small difference of the XRD 002 scan for sample A and sample B can be ignored and considered as instrument caused error. The X-ray (102) ω-scan FWHM values of the superlattice template is 360 arc-seconds, 413 arc-seconds for Sample A and

421 arc-seconds for Sample B, as shown in Figure 4.4, a very small difference has been

shown, however, the difference may not be able to tell whether the change of pulse cycle

cause any tremendous effect to the material quality or not.
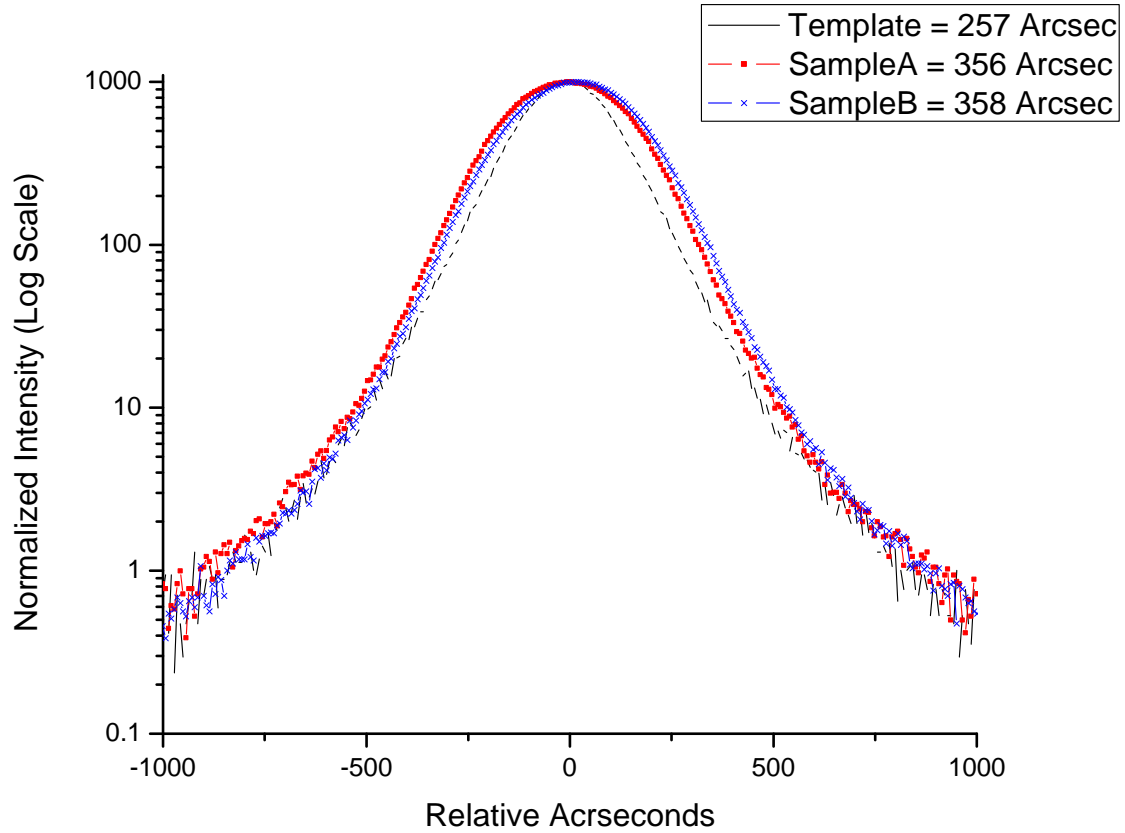
Figure 4. 3 X-ray (002) ω-scan rocking curve.
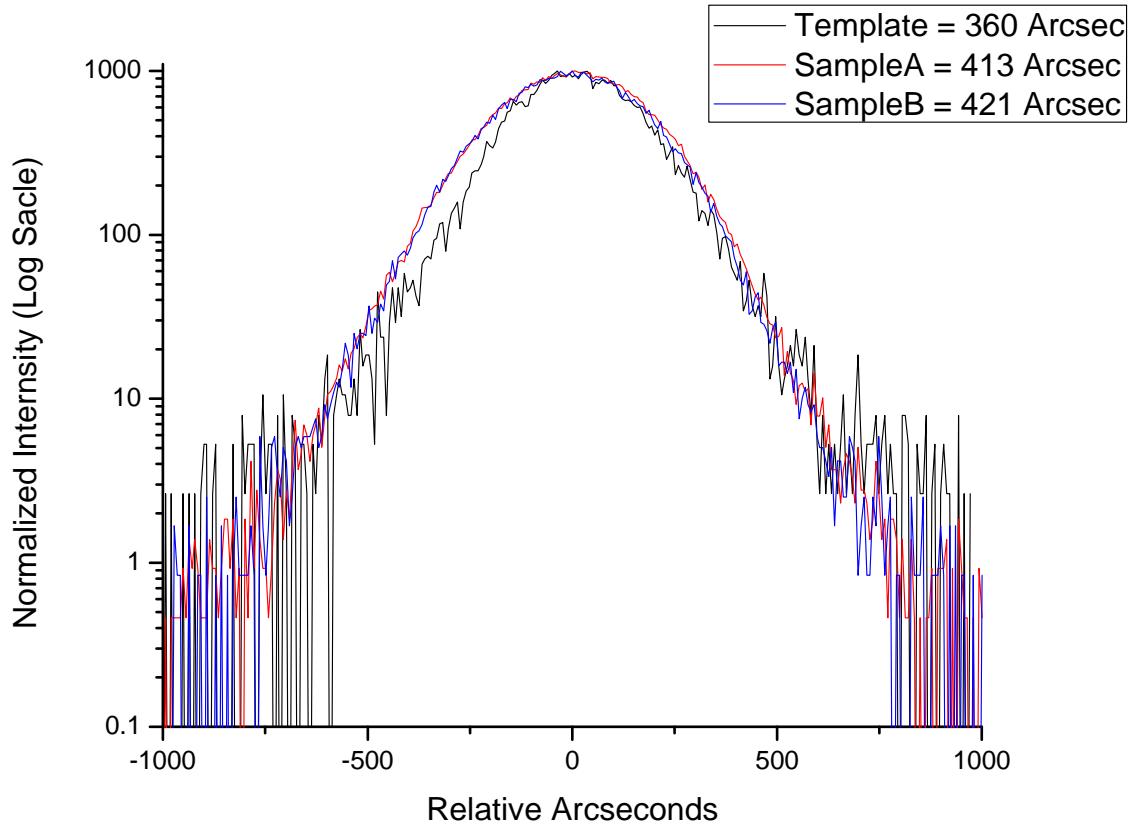
Figure 4. 4 X-ray (102) ω-scan rocking curve

To access the average dislocation density including pure edge, pure screw and mixed type dislocation, etch pits density (EPD) method is approved to be a easiest way, since EPD method doesn`t need long sample preparation time as compare to TEM sample preparation and the etching process can be easily done by dipping the sample in suitable etching solutions. The EPD images for sample A and sample B are showing in Figure 4.5 and Fig 4.6, respectively. Sample B has a smaller EPD than sample A and a smoother surface morphology is shown on the sample B. Both of the images showing a slightly increment in dislocation density as compare to its SL template (EPD~ $3 \times 10^8 cm^{-2}$), however the dislocation density values have significantly decreased comparing to the conventional n-AlGaN (EPD~ $1.2 \times 10^9 cm^{-2}$), which shows one order of magnitude

higher dislocation density. The concept of pulsed silicon doping is initially proved able to improve the crystal quality, and a series of experiments will optimize the nAlGaN by suppressing the propagation of the dislocation.
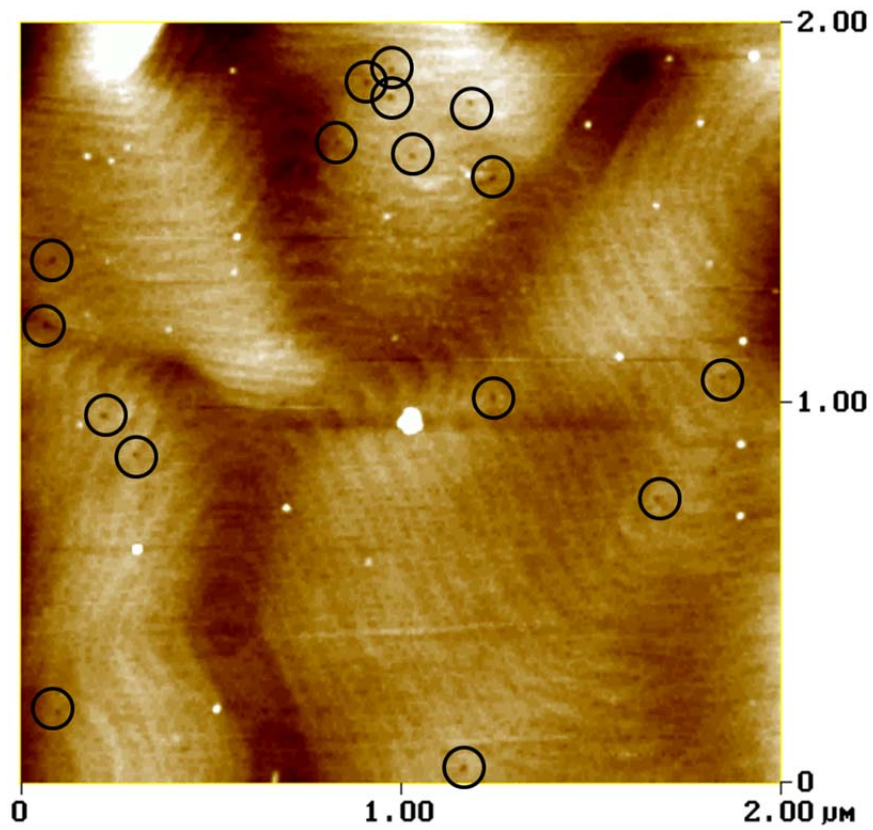
Figure 4. 5 AFM image of sample A (EPD~4×10^8 cm^{-2}).
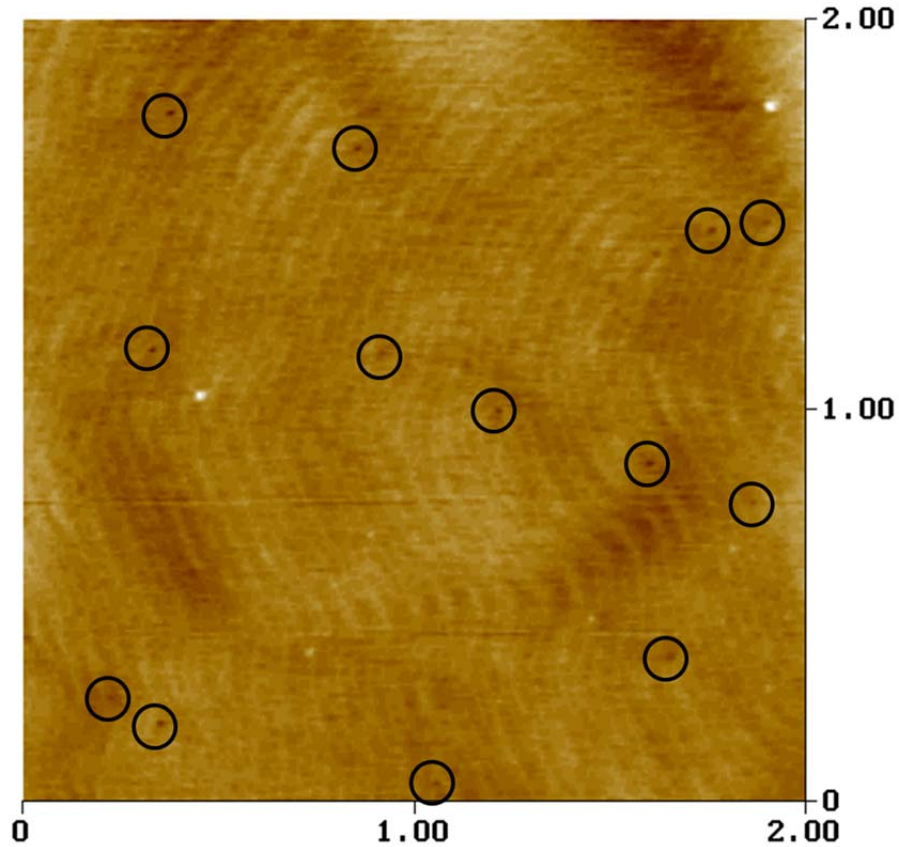
Figure 4. 6 AFM image of sample B (EPD~3.5×10^8 cm^{-2}).

Figure 4.7 shows the relation of sheet resistance and the si-doping pulse time, where sample A with 6 seconds si-doping off time having a sheet resistance value of 499 $\Omega/\square$, while sample B with 3seconds si-doping off time showing a lower sheet resistance value of 391 $\Omega/\square$. Since sample B has lower sheet resistance value and slightly lower EPD, also there is not much difference of the crystal quality characterized from the XRD scans, the si-pulse condition in sample B, consisting 3 seconds si-doping OFF time and 6 seconds si-doping ON time will be adopted as the base condition for the following silicon doping experiments.
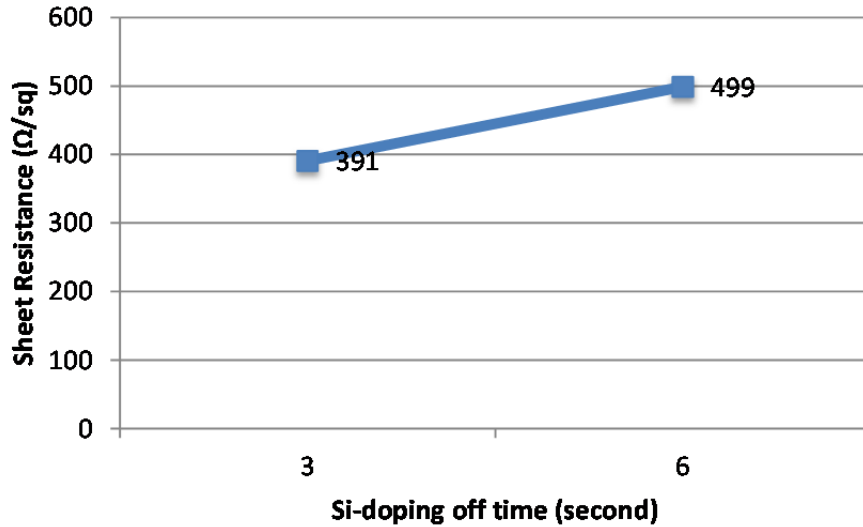
Figure 4. 7 Sheet Resistance with increasing of si-doping off time.

4.2 THICKNESS AND DOPING EFFECT

In this section, a series of experiments will be used to optimize the growth condition of the pulsed silicon doping for developing low defect, high conductivity and thick nAlGaN. The silicon pulse cycle will be kept the same for all the experiments, while the silicon doping level and the nAlGaN layer total thickness will be tuned. To get a comprehensive understanding of the effects from various growth condition to facilitate the optimization, cross-comparison of the characterization data including nomarski image, surface morphology, XRD on-axis and off-axis scans, XRD reciprocal space mapping, sheet resistance etc. will be applied.

4.2.1 Thickness effect with constant doping level

Two different experiment setups will be used to find the effect of thickness to the nAlGaN material properties. For the first setup, four different thickness nAlGaN will be compared, while the silicon doping level of 40 sccm flowing constantly during the silicon

70

pulse ON time. To differentiate these four samples based on the thickness, the sample has the same thickness as the conventional nAlGaN will be called 1X-40, where the 40 indicating the doing level, similarly sample with double thickness as compare to the conventional nAlGaN will be named 2X-40, thus four samples, 1/2X-40; 1X-40, 2X-40, 4X-40 will be first compared here. Transmission spectrum of 2X-40 is shown in Figure 4.8 with a sharp absorption edge of 250nm, the other three samples have a similar transparency and absorption edge and thus no need to show all the result here. The thickness of the nAlGaN layer for sample 2X-40 with a value of 6.4 μm was determined by SEM cross-section image as shown in the Figure 4.9. The surface macro-morphology of the samples are exhibited by Nomarski mode optical microscopy as shown in Figure 4.10. Smooth surface is shown on both 1/2X-40 and 1X-40 samples, however, as the thickness increase some hexagonal sharp shallows with a pit at the center can be seen, this phenomenon becomes severe while the thickness further increase as shown in the 4X-40 case, which may be too rough for the consequent layers. The micro-scale surface morphology is carried by AFM for the samples, for the two thinner layers, the surface is smooth with RMS values of 0.85nm and 0.96nm respectively. While the thickness increases, as suggested from the previous Nomarski images, the surface is getting rougher for both of the samples as shown in the Figure 4.11, and the roughness increases to 0.63nm and 0.85nm for 2X-40 and 4X-40 respectively. This trend should be able to be modified through the growth condition. However, the surface morphology cannot provide the crystal quality information of the sample and thus XRD scans and EPD will be used.

71
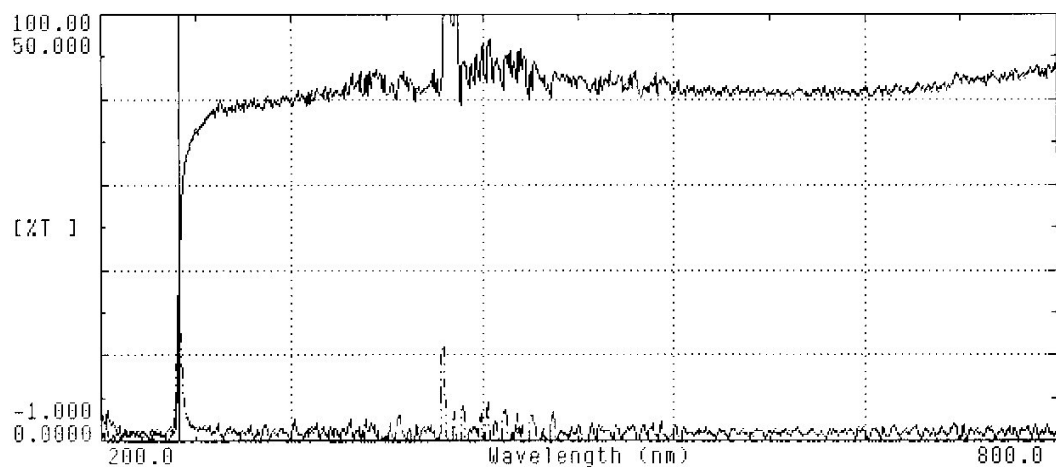
Figure 4. 8 Transmission spectrum of silicon doping modulation AlGaN.
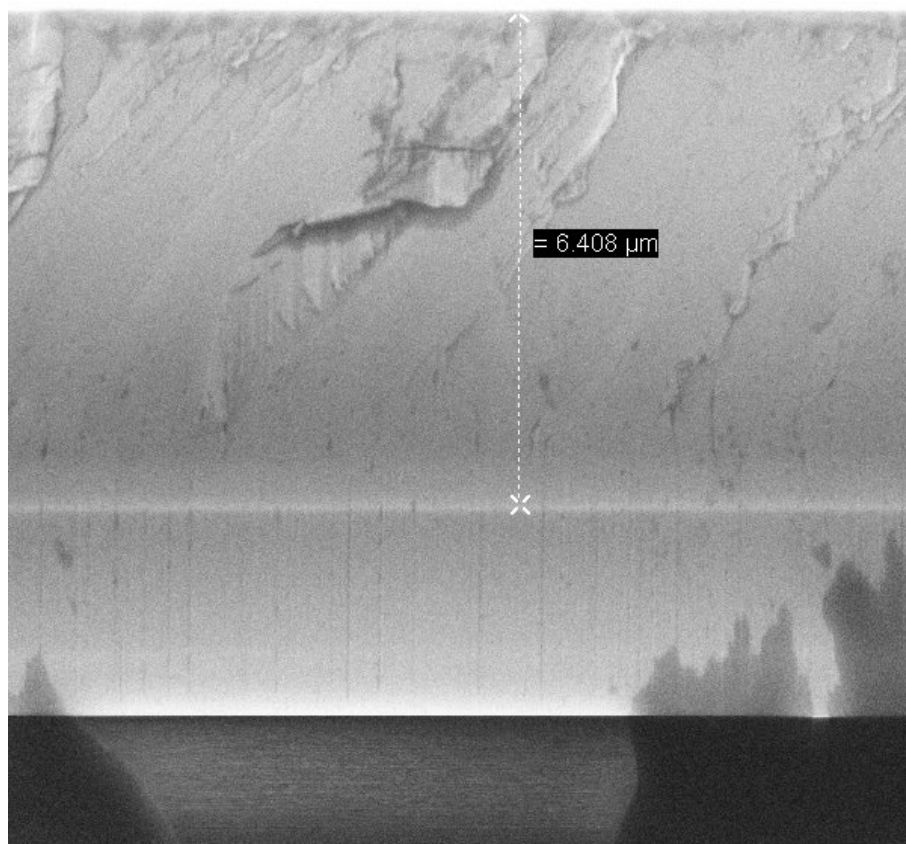
Figure 4. 9 SEM cross-section image of 2X-40.
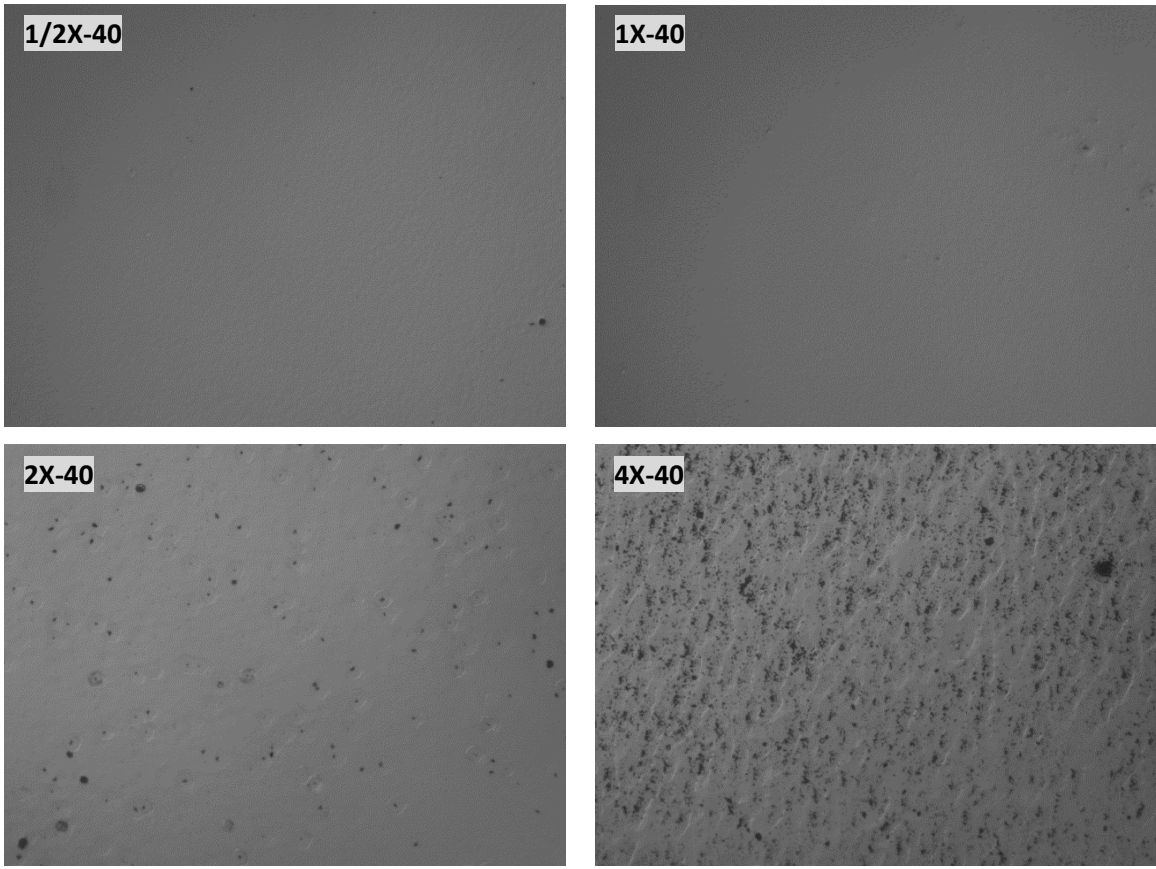
Figure 4. 10 Nomarski images of silicon doping modulation AlGaN samples.
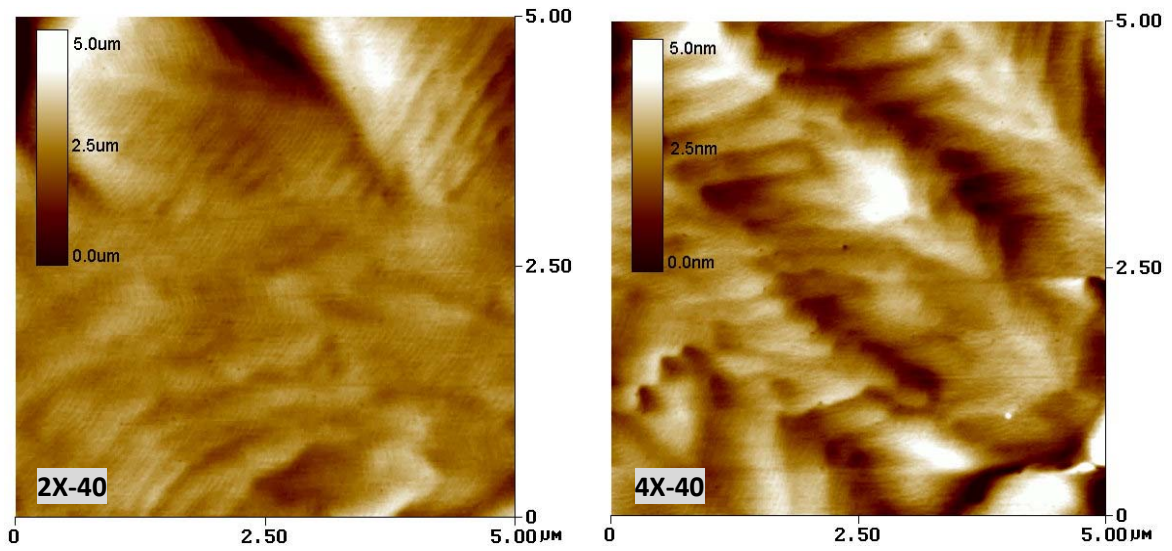
Figure 4. 11 AFM images of silicon doping modulation AlGaN samples.

Figure 4.12 reveals the XRD on-axis scans and off-axis scans of the samples, both of the scans showing a trend of increased FWHM values while the nAlGaN thickness were increased. From the experiences, we may conclude that the crystal quality of the thicker silicon pulsed nAlGaN must be poorer than the thin one, however this result is contradict to the etching pits experiments as shown in Figure 4.13, where the 1X-40sample and the 4X-40 samples are showing the same EPD value (4×10^8cm^{-2}), while 1/2X-40 and 2X-40 are getting EPD value of 3.5×10^8cm^{-2} and 3.75×10^8cm^{-2}, respectively. This disagreement maybe because the XRD scans are measuring the entire nAlGaN layer including the bottom portion and surface, any defects within this nAlGaN layer no matter before or after bending or whether forming loops or not will contribute to the broadening of the XRD rocking curve and thus the FWHM value, whereas the EPD value will only related to the threading dislocations propagating to the surface. It is understandable that a thicker sample will have more roughened interfaces caused by the pulsed silicon doping technique and thus a higher FWHM value; on the other hand, these roughened interfaces may be the driven sources bending the threading dislocation, however the EPD value did not further decrease with the increasing interface, it is possible that there are additional dislocation generated during the thickening process when the thickness pass the critical value.
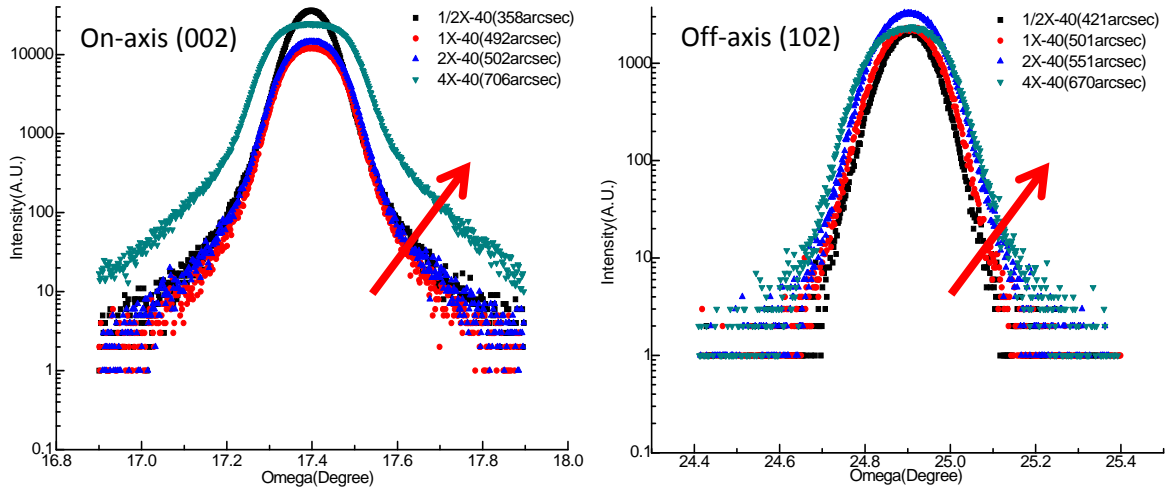
Figure 4. 12 XRD (002) and (102) scans of silicon doping modulation AlGaN samples.

1X-40(EPD~4×10^8cm^{-2})   4X-40(EPD~4×10^8cm^{-2})
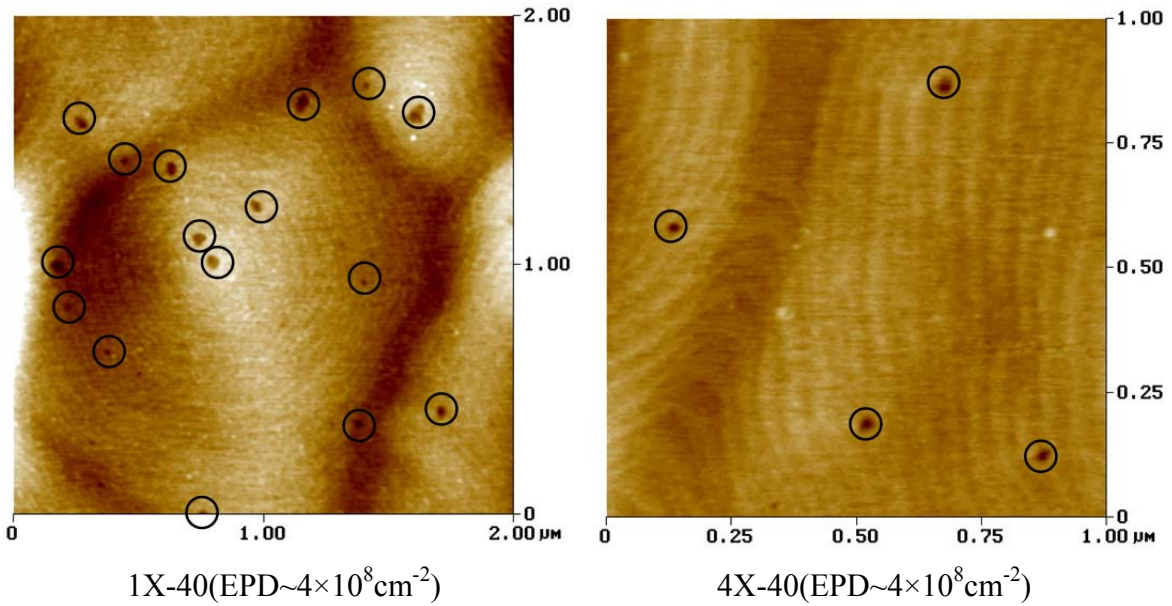
Figure 4. 13 AFM images of etched silicon doping modulation AlGaN samples.

The Sheet resistance values of the samples are plotted in the Figure 4.14, where he sheet resistance values are reciprocally corresponding to the thickness, and a lowest sheet resistance value of 38Ω/□ is achieved.
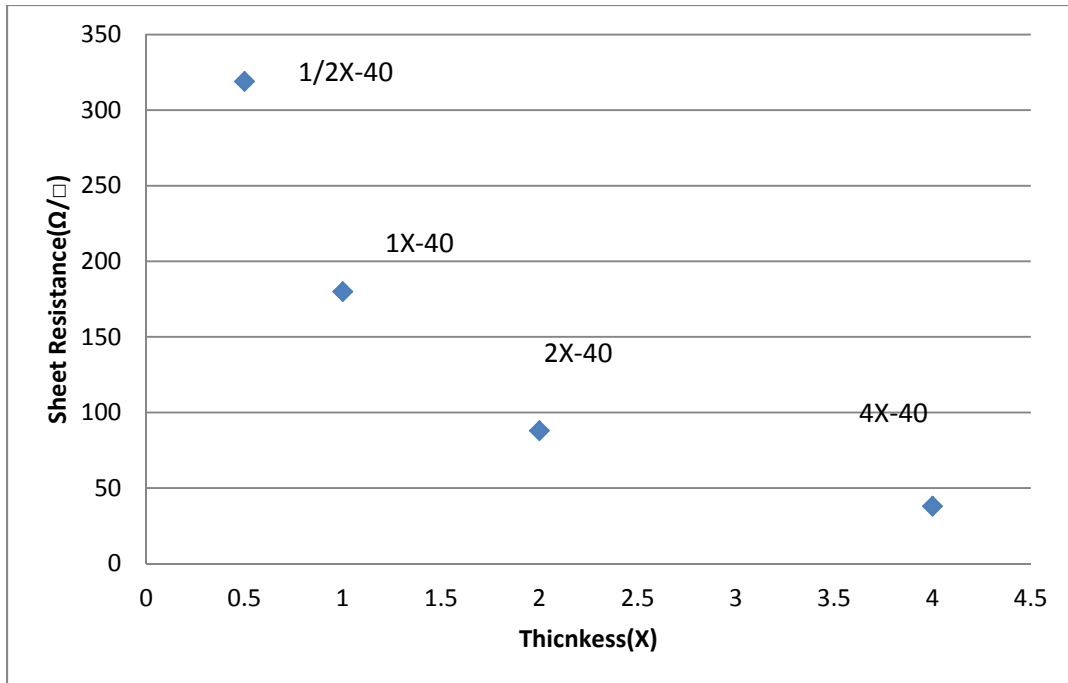
Figure 4. 14 Sheet resistance of silicon doping modulation AlGaN samples.

The second experiment setup is increasing the silicon doping level to 80 sccm, samples 1X-80 and 2X-80 will be compared. The transmission data of both samples showing sharp absorption edge around 250nm. AFM roughness showing slightly rougher surface on the thicker sample with a RMS value of 1.3nm, same phenomenon has been seen on their Nomarski images as shown in Figure 4.15 where the 2X-80 sample showing a more undulate feature as compare to the 1X-80, these increased roughness along with the thicker deposition is following the same trend from the previous experiment setup. The XRD on-axis and off-axis scan also showing the same tendency for these samples, namely the thicker has higher FWHM values on both scans as shown in the Figure 4.16.

Figure 4. 15 Nomarski images of silicon doping modulation AlGaN samples.
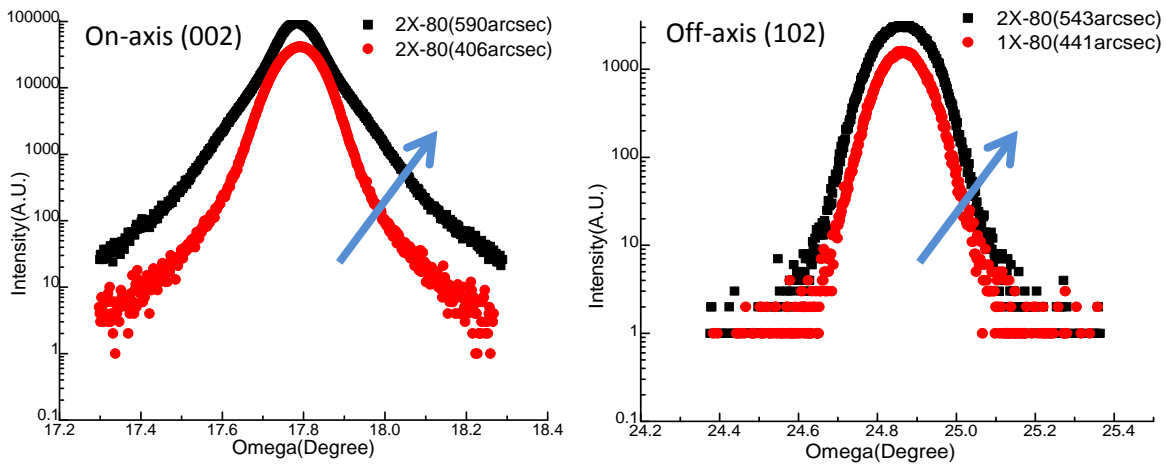
Figure 4. 16 XRD (002) and (102) scans of silicon doping modulation AlGaN samples.

As mentioned above this trend cannot accurately tell the material defects density, instead the EPD method will be adopted as shown in the Figure 4.17, though the XRD scans showing a wider peak, the EPD of the 2X-80 sample has reach a low EPD value of 2.5×10^8cm^{-2}. Also sheet resistance value of the 2X-80 sample is as low as 50Ω/□. The strain relaxation relation of the above samples in both experiment setup 1 and 2 is depicted in the Figure 4.18 extracted from the XRD reciprocal space mapping on (105) plane. When the doping is 40 sccm, the more strain relaxed with the increased thickness, and in the 4X-40 sample the layer is totally relaxed, whereas for the case of 80 sccm the

strain did not change at all with thickness. The phenomenon may because the heavily doping is the dominant factor in the strain relaxation process, and thus the increased thickness did not affect the strain relaxation, however, a further increase thickness may induce more relaxation. Since the 2X-80 sample possess low EPD density of $2.5 \times 10^8 cm^{-2}$ indicating a high crystal quality, a low sheet resistance of $50\Omega/\square$ implicating a high conductivity, as well as a smooth surface with AFM RMS value of 1.3nm, a full LED structure will be developed by adopting this silicon pulsed nAlGaN.

1X-80(EPD~$3.75 \times 10^8 cm^{-2}$)   2X-80(EPD~$2.5 \times 10^8 cm^{-2}$)
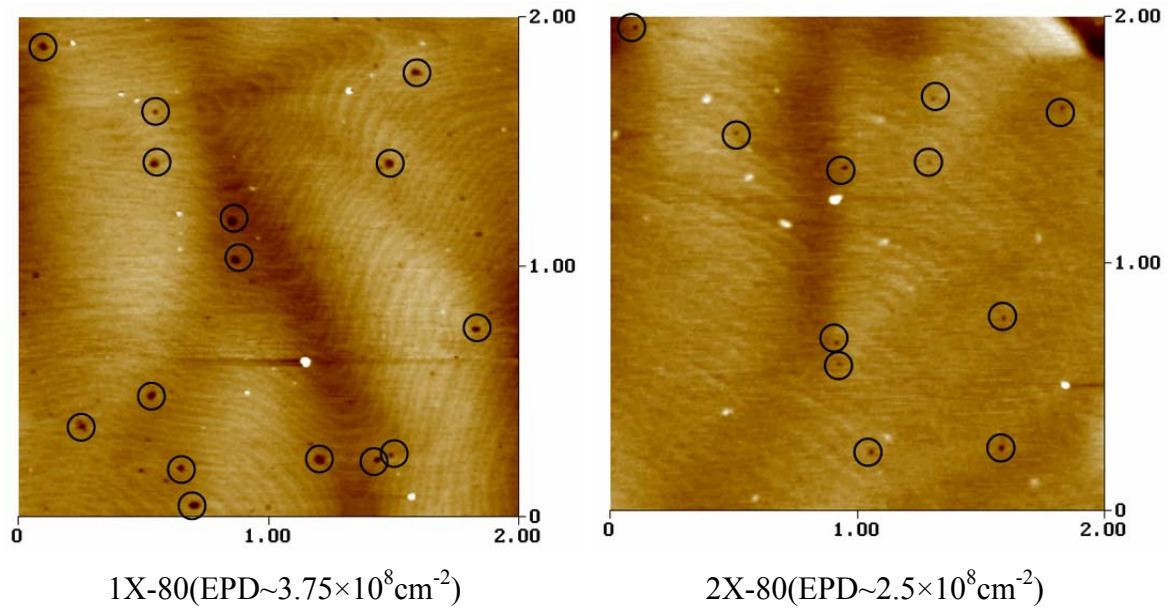
Figure 4. 17 AFM images of etched silicon doping modulation AlGaN samples.
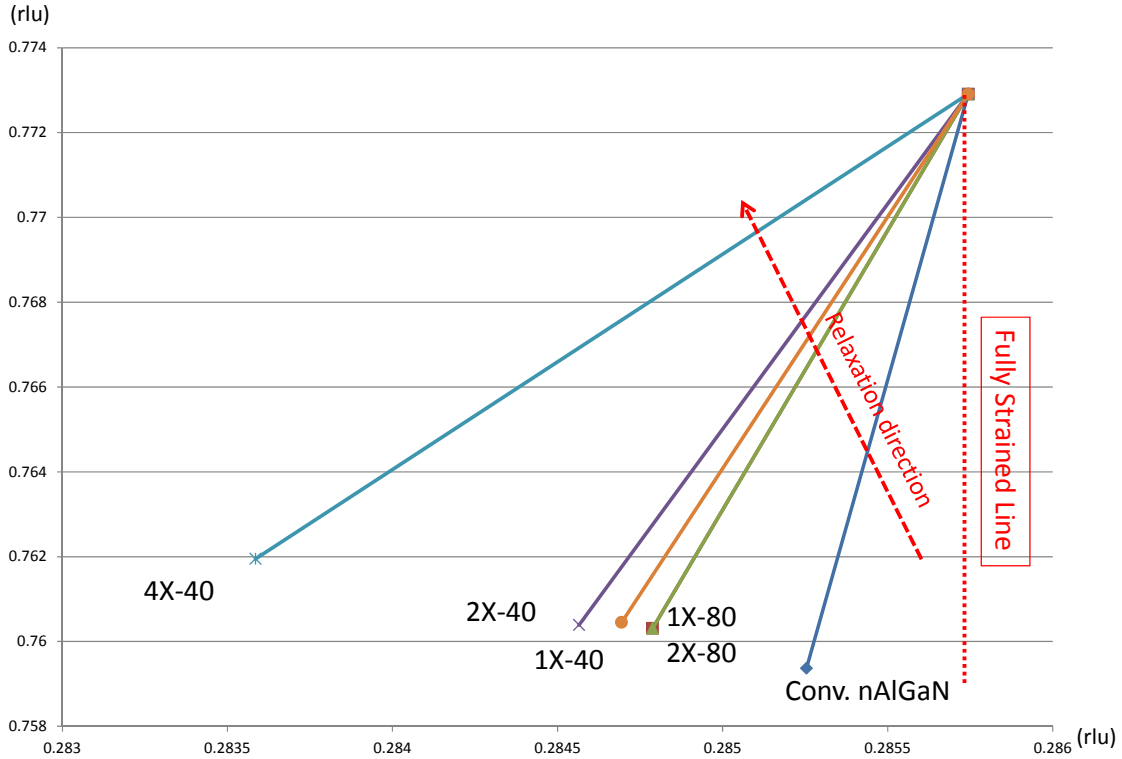
Figure 4. 18 Strain relaxation of silicon doping modulation nAlGaN samples.

4.3   SILICON DOPING MODULATION ALGAN ON ALN

The pulsed si doping technique also is employed to deposit nAlGaN directly on AlN, two samples having exactly the same growth condition as 2X-40 and 2X-80 named 2X-40-AlN and 2X-80-AlN were studied. In the Figure 4.19 dramatic cracks are showing on the 2X-80-AlN sample, while for the same thickness sample, 2X-40-AlN showing a more smooth surface. Comparing the 2X-80-AlN sample to the 2X-80 one (Figure 4.14), which was deposited on the superlattice template, one can deduce that the removal of superlattice template attribute to the cracking. However, there are no cracks revealed on the 2X-40-AlN sample, which may because the two different growth condition samples have different stress system from each other. When the stress pass a critical value in the 2X-80-AlN sample due to the removal of superlattice template, which impacting its stress

system, cracks were triggered to release these stress. The impact of the nAlGaN crystal quality by the removal of superlattice template is characterized by XRD scans and EPD. The increase of silicon doing showing an increase of XRD FWHM values on both scans, this increase may be related to the cracks on the heavily doped sample.
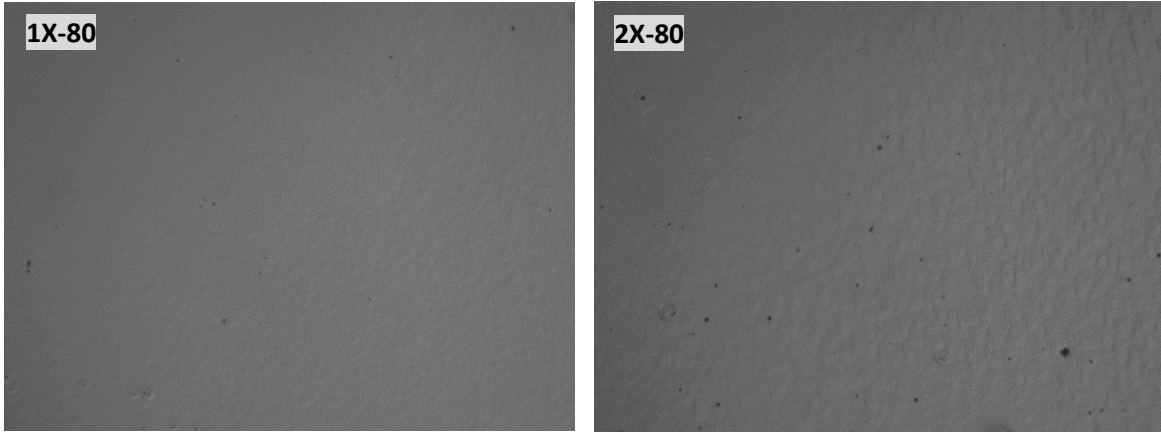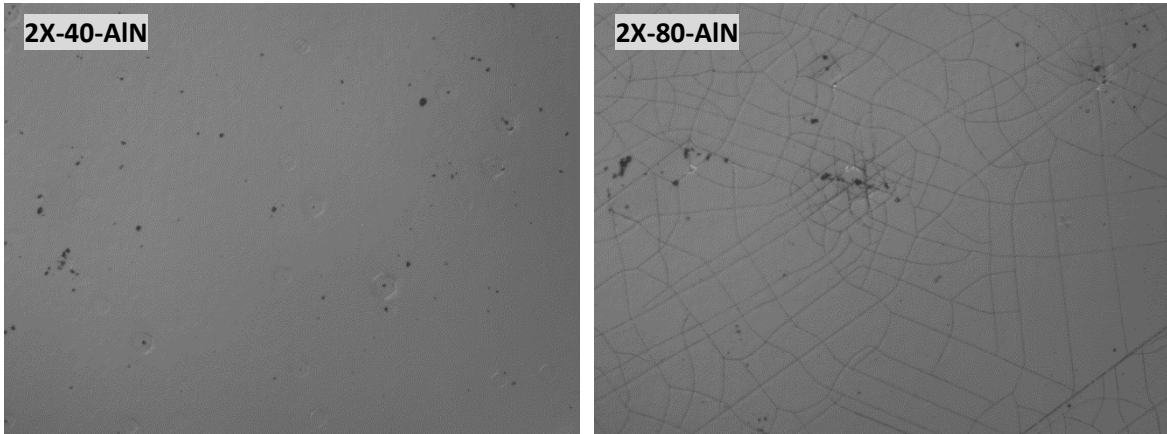

Figure 4. 19 Nomarski images of silicon doping modulation nAlGaN samples on AlN template.
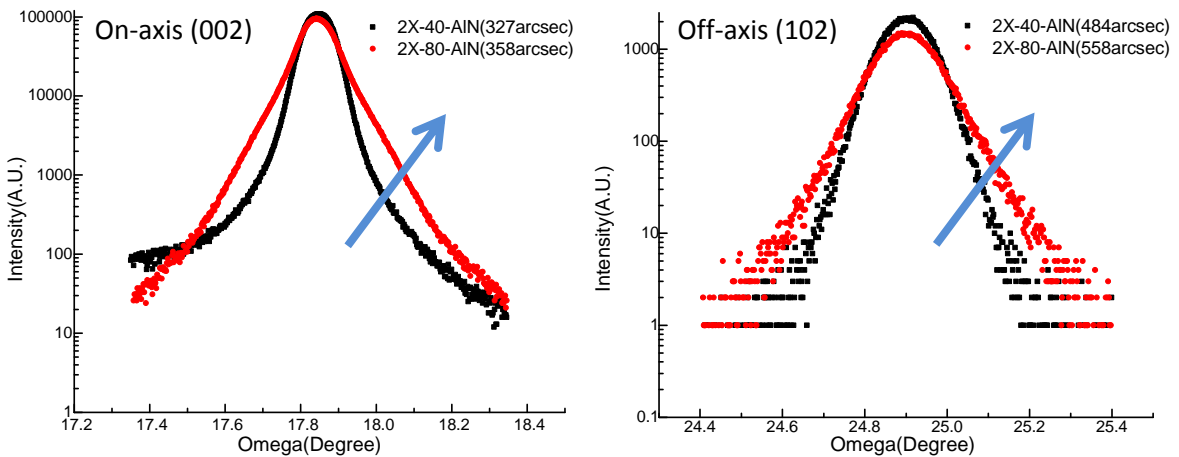
Figure 4. 20 XRD (002) and (102) scans of silicon doping modulation AlGaN samples on AlN template.

The EPD results is showing in the Figure 4.21, both of the samples showing huge degradation of their crystal quality, the EPD value is $1.1\times10^9 cm^{-2}$ and $1.2\times10^9 cm^{-2}$ for

80

2X-40-AlN and 2X-80-AlN respectively, while the value is 3.75×10^8cm^{-2} for 2X-40 and

2.5×10^8cm^{-2} for 2X-80. Dramatic difference results have been shown between pulsed

silicon doing nAlGaN technique to the superlattice nAlGaN, in which the EPD only

increased from 2.5×10^8cm^{-2} to 3.75×10^8cm^{-2} as shown in the Figure 4.22. This can be

strong evidence that the superlattice nAlGaN technique is able to successfully combine

the function of superlattice template into the nAlGaN and demonstrate relief of strains.

2X-40-AlN(EPD~1.1×10^9cm^{-2})   2X-80-AlN(EPD~1.2×10^9cm^{-2})
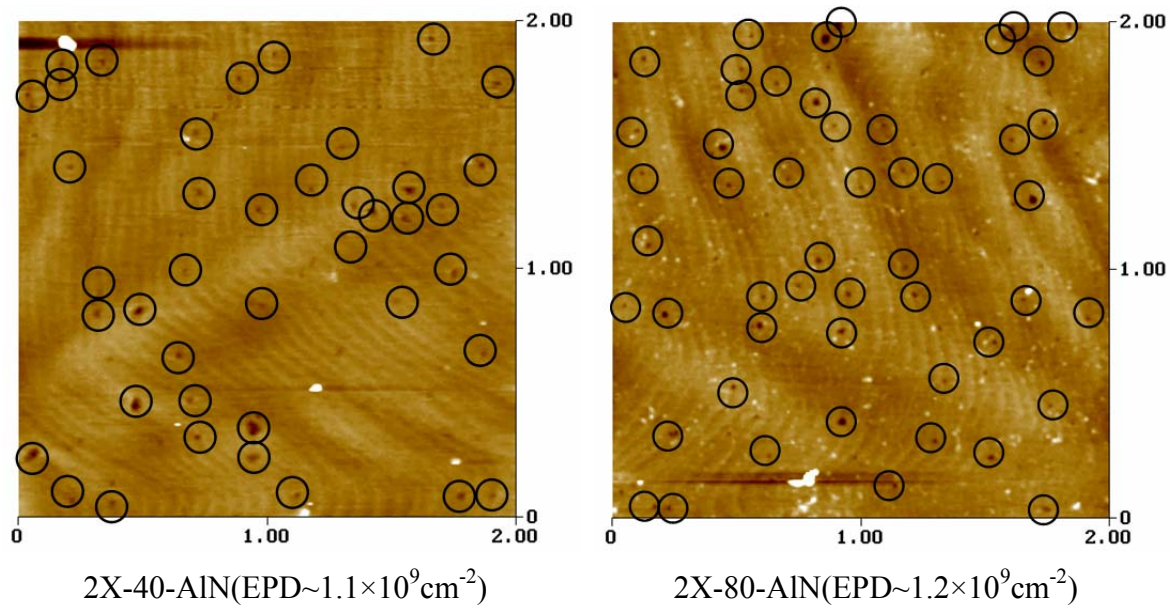
Figure 4. 21 AFM images of etched silicon doping modulation AlGaN samples on AlN template.
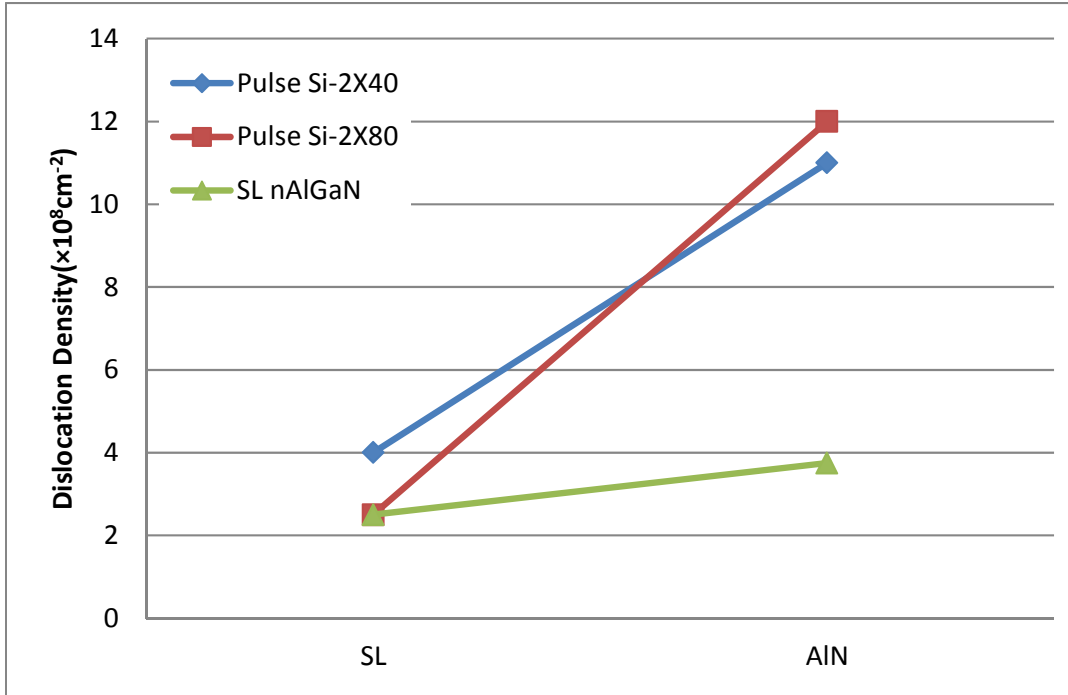
Figure 4. 22 Dislocation densities of nAlGaN samples on different template.

XRD reciprocal space mapping is carried out for revealing the strain relaxation information for the samples in this chapter as depicted in the Figure 4.23. The heavily doping 2X-80-AlN sample is showing more relaxation than the light doping 2X-40-AlN sample through the generation of heavily cracking. Comparing all these samples to the conventional one, the effective strain relaxation has been shown, and thus the material quality has been dramatically improved.
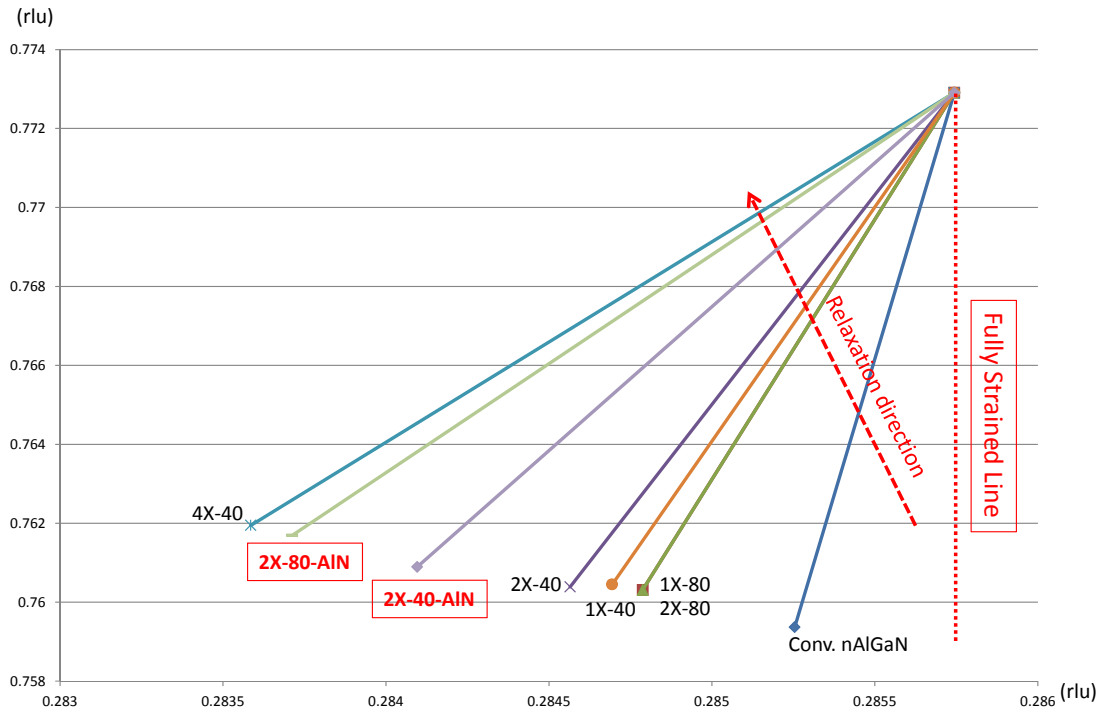
Figure 4. 23 Strain relaxation of nAlGaN samples.

CHAPTER 5

HIGH EFFICIENCY DEEP UV LED

In this chapter, the growth, characterization and fabrication of high efficiency of deep UV LEDs will be demonstrated. All the LEDs will employ identical epitaxial structures, except the buffer layers and electron cladding layers, which will be applied based on the previously optimized nAlGaN techniques, specifically, short period superlattice nAlGaN, pulsed silicon doping nAlGaN and conventional nAlGaN. The comparison of the optical power and the light spectrum of the LEDs will be carried out by electroluminescence on the as grown DUV LED wafer.

5.1 DEVELOP OF HIGH EFFICIENCY DEEP UV LED

To develop the high efficiency deep UV LED, the low defects, high conductivity nAlGaN has been demonstrated by using the short period superlattice nAlGaN(SPSL nAlGaN) and silicon doping modulation nAlGaN in the chapter 3 and chapter 4 respectively. In this section, deep UV LED structure carried out by growing the standard active region and p-type layers on two different proposed nAlGaN layers are used to compare with the deep UV LED developed on the conventional nAlGaN, which is depicted in the Figure 5.1. The LED structure is deposited on 2" c-plane sapphire substrate, then the high temperature AlN and superlattice template were used as template for the growth of nAlGan electron cladding layer. On top of the nAlGaN layer, five periods of multiple quantum wells (MQWs) are grown as active region and designed to

84

emit light with emission peak at around 280nm. A 70% aluminum content AlGaN is then grown on the MQWs as electron blocking layer to improve the injection efficiency by preventing the electron overflow, followed by a hole cladding layer and p-type contact layer for making ohmic contact, assisting holes injection. A more detail growth condition can refer to reference [114].

P+-GaN contact layer	Contact Layer
P-Al$_{0.5}$Ga$_{0.5}$N cladding layer	Hole Cladding Layer
P-Al$_{0.7}$Ga$_{0.3}$N blocking layer	Electron Blocking Layer
MQW AlGaN/AlGaN	5 Periods MQW
Conv. AlGaN:Si	Electron Cladding Layer
AlGaN/AlGaN SL	Strain Relief SL Template
AlN/AlGaN SL	
HT-AlN	High Temperature AlN
Sapphire (0001)	
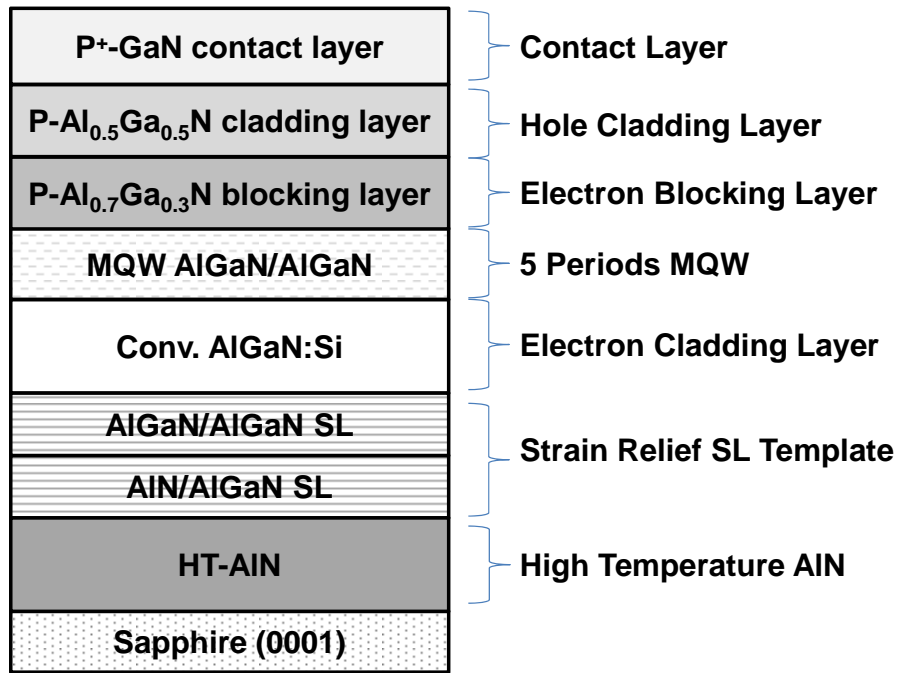
Figure 5. 1 Deep UV LED structure.

The influence of the nAlGaN layers to the LED optical power and light spectrum are characterized by electroluminescence (EL) by spectrometer. To prevent the confusion, the LED adopting conventional nAlGaN is noted as conventional LED(Conv. LED), while the LED employing silicon doping modulation technique in the nAlGaN and the LED applying short period superlattice nAlGaN layer are noted as Si:modulation LED and SPSL LED respectively. The epitaxial structure of each LED is illustrated in the Figure 5.2, where both of the conventional LED and the Si: modulation LED were grown

85

on superlattice template, whereas the SPSL LED was directly deposited on the AlN template without the additional strain-relief superllatice layer.

| (a)Conventional LED | (b)Si: modulation LED | (c)SPSL LED |
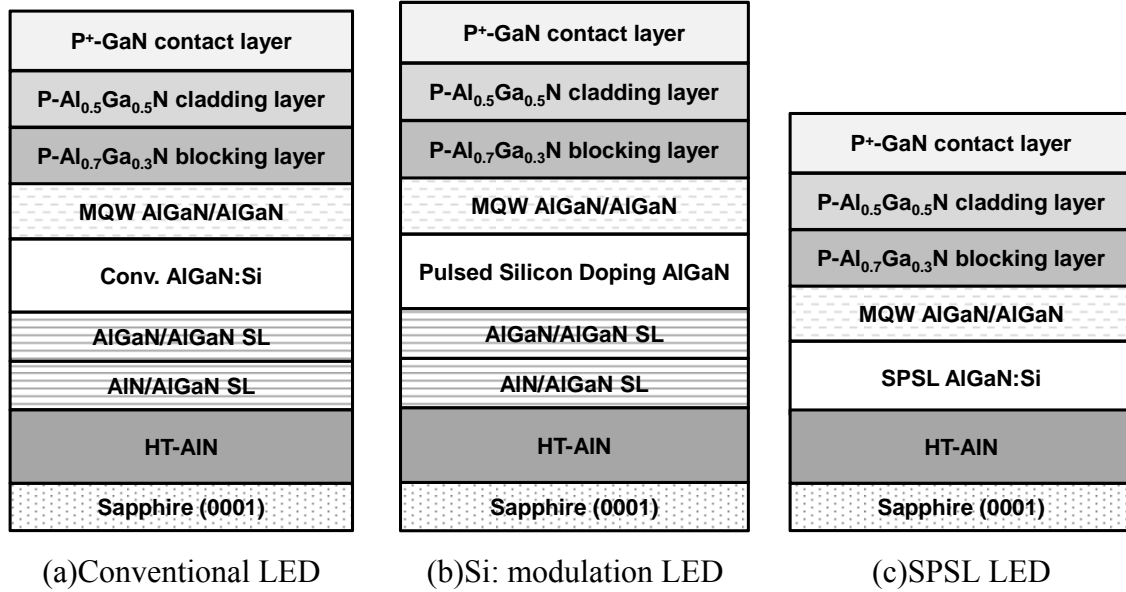
Figure 5. 2 Development of Deep UV LED structure with different nAlGaN techniques.

Figure 5.3 is showing the sheet resistance of these LED samples. High sheet resistance uniformity is seen on both Si: modulation LED and SPSL LED. The sheet resistance value is corresponding to the previously reported nAlGaN techniques, with the average value of 200.7 $\Omega/\square$ for SPSL LED, 108.9 $\Omega/\square$ for conventional LED and a lowest value of 53.57 $\Omega/\square$ for Si: modulation LED.

|(a)Conventional LED|(b)Si: modulation LED|(c)SPSL LED|
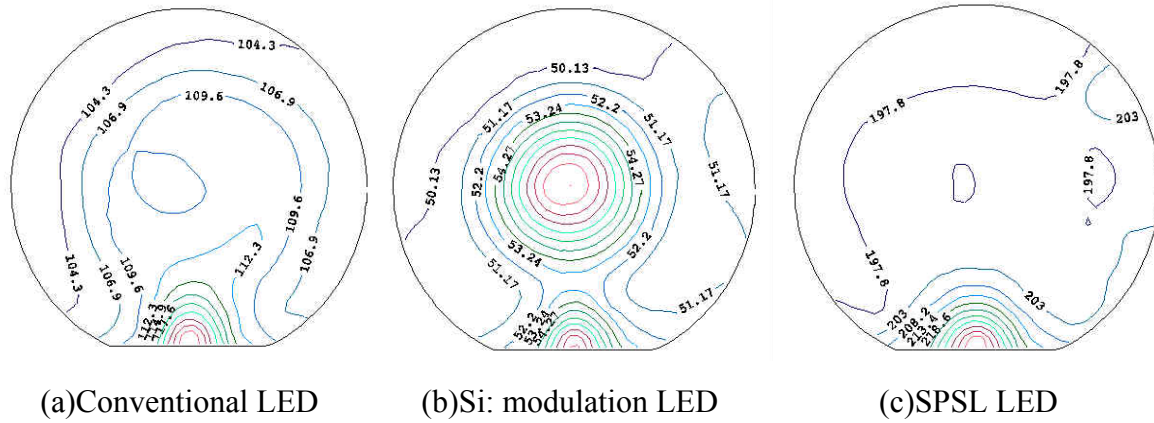
Figure 5. 3 Sheet resistance mapping of DUV LED samples.

Figure 5.4 exhibit the as grown LED wafer spectrum of the conventional LED with a sharp band to band emission peak at 280nm and a long wavelength parasitic emission peak at 345nm, where the primary to parasitic peak emission ratio is around 250. The long wavelength parasitic peak usually arises from the radiative recombination involving deep levels, namely from conduction band to deep level recombination in either barrier layer or most likely p-AlGaN layer. The inset picture in the Figure 5.4 shows a schematic of the band to band and band to deep level processes [115]. The parasitic emission can be improved by the adoption of electron blocking layer and improving the epitaxial layers crystalline quality. The light spectrum of the Si: modulation LED and SPSL LED are shown in the Figure 5.5 (a) and (b) respectively. Since both of the Si: modulation nAlGaN and SPSL nAlGaN have shown the decrease of dislocation density in the previous chapters, the LED spectrums based on these two nAlGaN techniques show the reduction of the long wavelength parasitic peak, resulting in the main to parasitic peak emission ratio larger than 1000. Beside the shrink of the 345nm parasitic peak, a longer wavelength side peak center at 410nm has revealed, which is possibly due to the radiative recombination of overflowed electron to the deep

level at p-GaN and may be mitigated by further design of the electron blocking layer. It is noticeable that an existence of short-wavelength emission shoulder at 260nm, which may result from the recombination of AlGaN barrier.
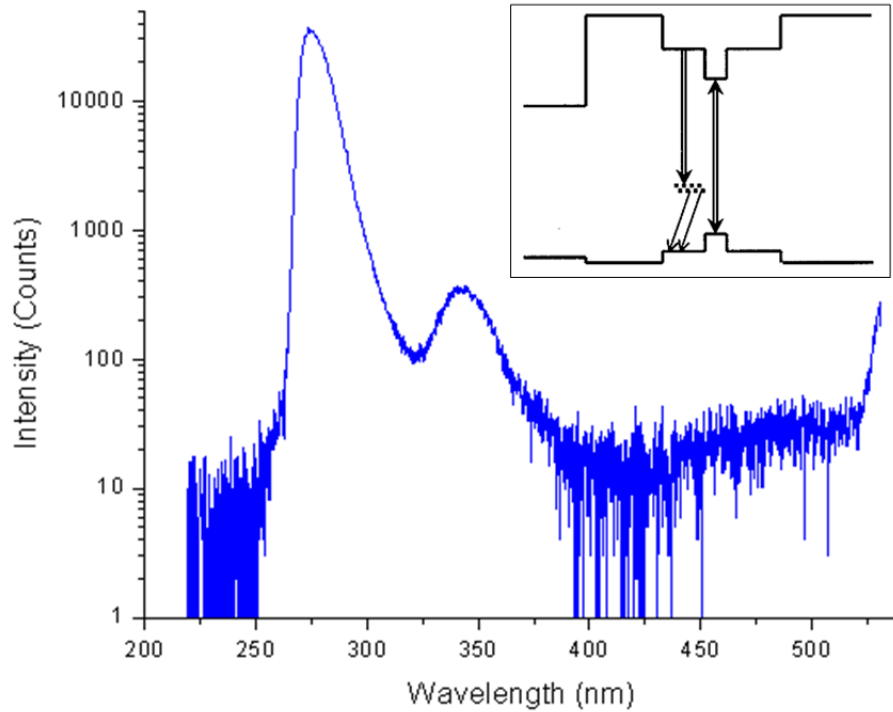
Figure 5. 4 EL emission spectrum of DUV LED on conventional nAlGaN layer.
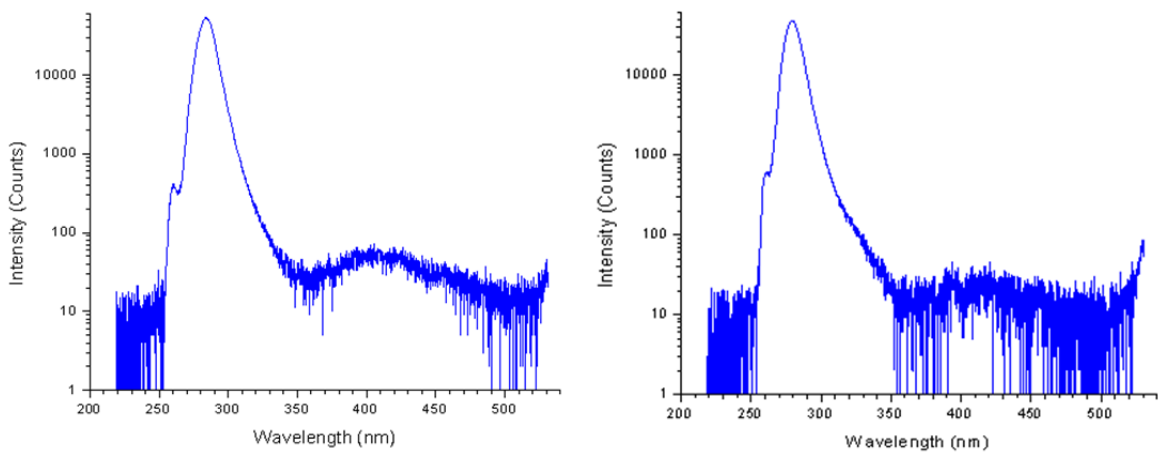
(a) Si: modulation LED (5.5 ~ 5.7uw)   (b) SPSL LED (4.8 ~ 5.5uw)

Figure 5. 5 EL emission spectrum of DUV LED.

The Relation of the LED optical power to the LED nAlGaN dislocation density is depicted in the Figure 5.6, where the obvious trend is showing that the decrease of dislocation density results in an increase of the DUV LED optical power to around 32%, and it is believed that this improvement is due to the reduce of the dislocation density assists the process of radiative recombination, namely the probability for the occurrence of radiative recombination has increased.
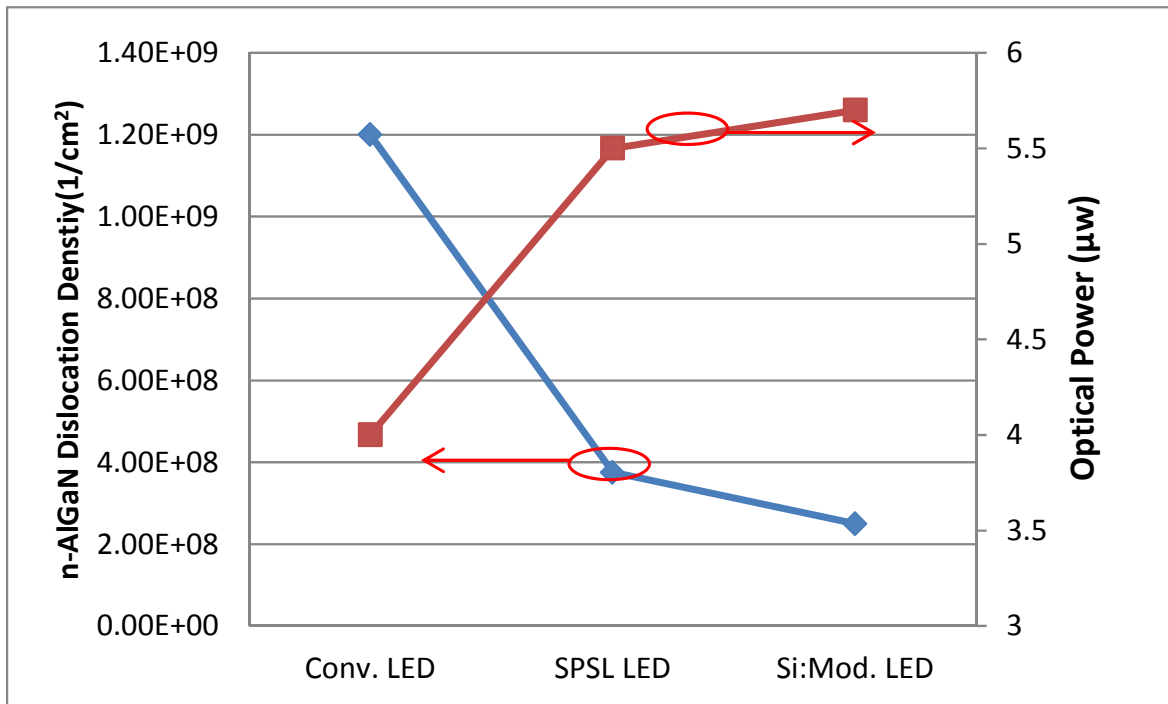
Figure 5. 6 Comparison of dislocation densities and optical power of DUV LEDs with different nAlGaN techniques.

5.2   DEEP UV LED DEVICE

In this section, UV LED device is carried out on the Si: modulation LED wafer by using the conventional LED fabrication process, where the mesa size is 200μm×200μm. The Deep UV LED device spectrum is shown in the Figure 5.7, where the main emission peak is centered at 281nm. Parasitic peaks, such as the short wavelength 260nm side peak

and longer wavelength 350nm and 440nm side peaks with higher main to parasitic emission peak can are also shown on the LED device light emission spectrum.
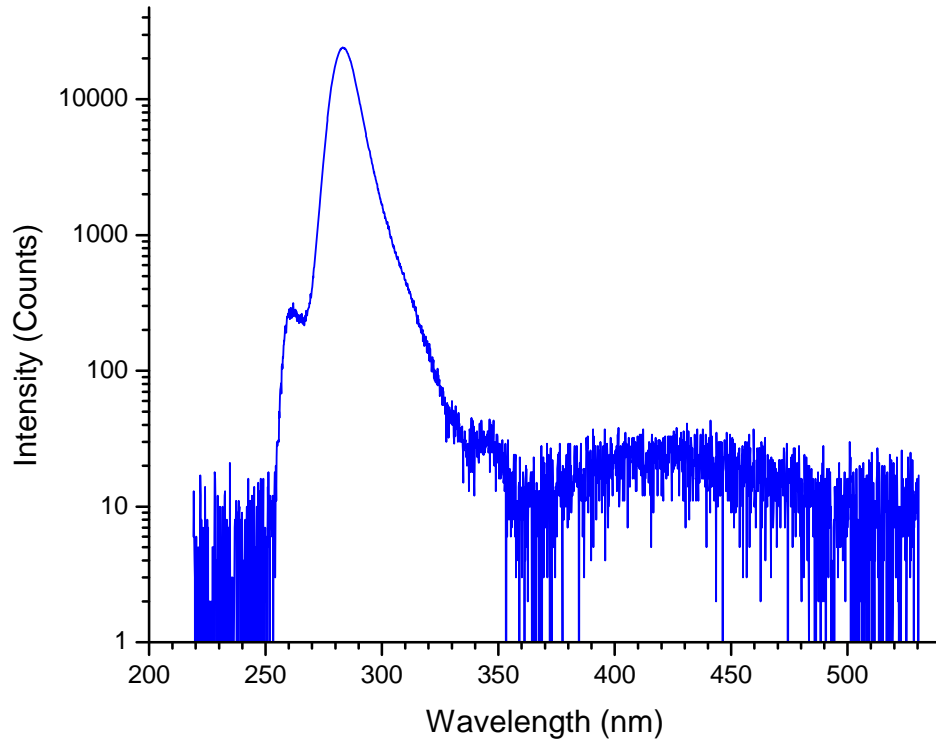
Figure 5. 7 Silicon doping moduation Deep UV LED light spectrum.

Figure 5.8 exhibits the comparison of LED devices optical power between conventional structure LED and si: modulcation structure LED. By adopting the silicon modulation technique, the LED optical power has increase around 25% from 0.48mW to 0.61mW, since the device fabrication factors, including the dimension are intently kept the same, indicating the light extraction efficiency for both of the devices are the same. Thus the improvement of the optical power can be attributed to the improvement of the international quantum efficiency, due to the dramatically decrease of the dislocation density by adopting the si doping modulation technique. Apart from the improvement of the optical power performance, the use of the si doping modulation technique can help to

achieve crack free n-AlGaN with thickness up to 10μm, resulting the sheet resistance as low as 38Ω/□. Considering the surface morphology and the smoothness, the thickness of the nAlGaN was designed around 6um with a sheet resistance of 53 Ω/□ for the si: modulation LED, while the conventional LED has a higher sheet resistance of 109 Ω/□. The decrease of the nAlGaN sheet resistance results in the increase of the slope of the I-V curve as shown in the Figure 5.9.
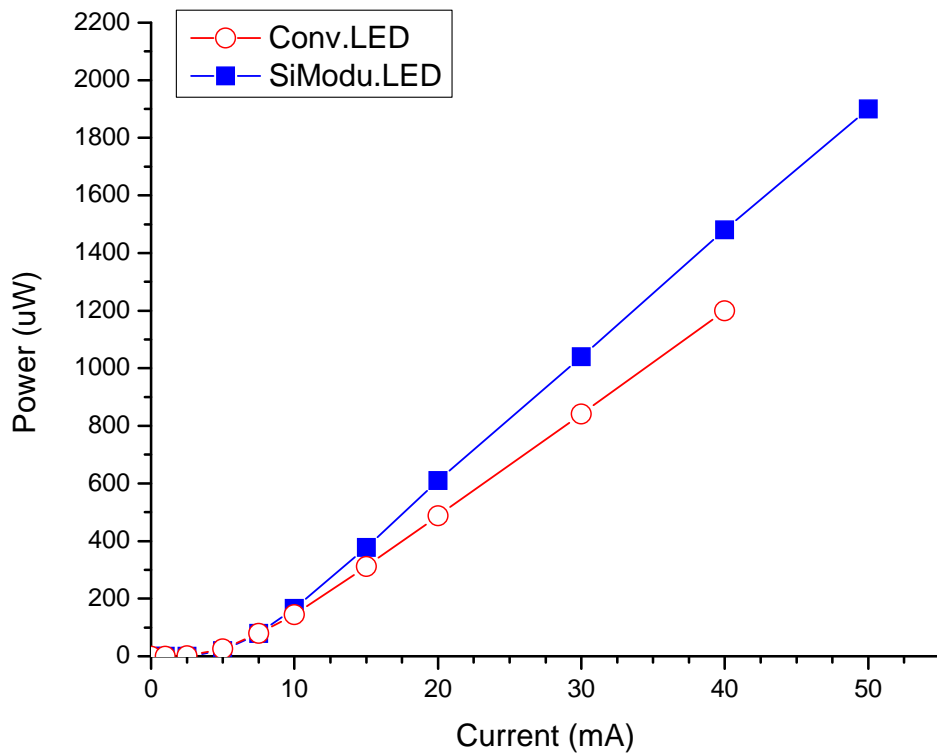
Figure 5. 8 L-I characteristics of DUV LEDs.
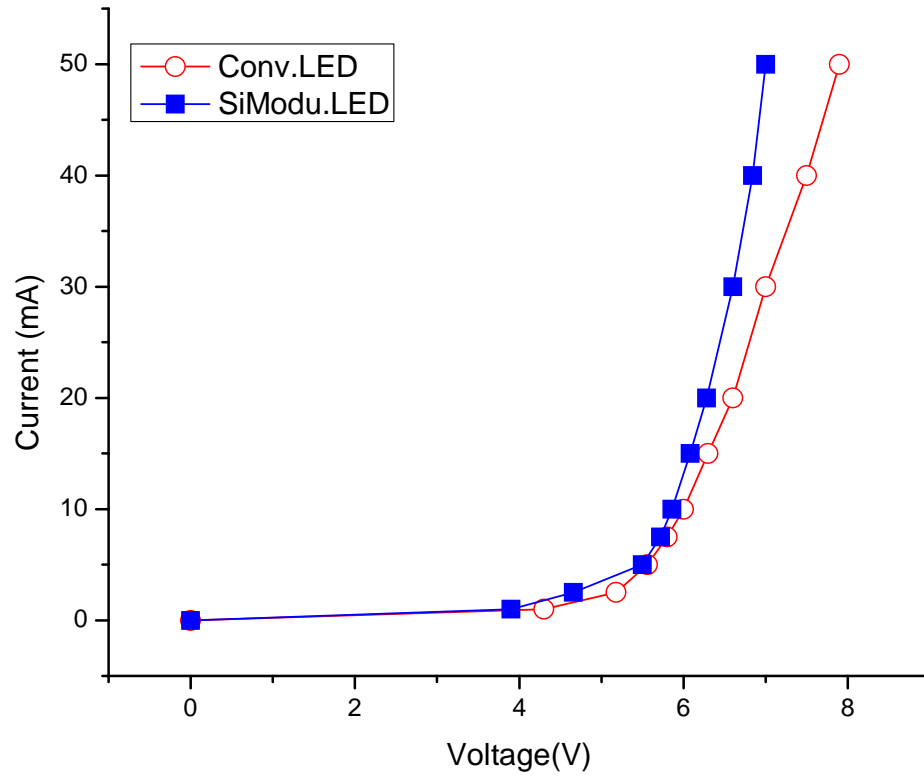
Figure 5. 9 I-V characteristics of DUV LEDs.

CHAPTER 6

FUTURE WORKS AND CONCLUSION

6.1 CONCLUSION

This research is focused on improving the efficiency of deep UV optoelectronic devices, by improving the base template epilayers specifically silicon doped n-type AlGaN electron cladding layer on which the subsequent quantum well and other device layers are grown. The n-type AlGaN electron cladding layer is crucial in determining the internal quantum efficiency (IQE), current spreading issues and junction heat dissipating performance for optoelectronic devices. This dissertation focused on developing methods to reduce dislocation in the silicon doped n-type AlGaN which is currently the limiting factor in achieving high power, robust and stable Deep UV optoelectronic devices.

Two key approaches have been investigated to mitigate the defect generation namely; a) Silicon doping modulation AlGaN, b) short period Superlattice (SPSL) silicon doped AlGaN. This research has shown that the optimized silicon doping modulation technique was able to create multiple rough interfaces to decrease the density of threading dislocation from $1.2 \times 10^9 \text{cm}^{-2}$ to 3×10^8 cm^{-2} as compared to the conventional n-AlGaN. Furthermore, by adopting this technique, a 12nm thick, crack free silicon doped $Al_xGa_{1-x}N$ (x=60%) layer is able to achieved with a low sheet resistance of 38Ω/□. Another proposed short period superlattice silicon doped AlGaN technique showed the ability of stain relaxation investigated by XRD reciprocal lattice mapping and is able to

filter screw type threading dislocation from 1.2×10^9cm^{-2} to 2.5×10^8cm^{-2}. One of the major contribution of this technique is not only the ability in effectively decreasing dislocation density but also combining the function of un-doped superlattice template into this technique, which facilitate the development of low cost and low defects DUV LED directly on AlN template instead of on the additional un-doped superlattice template. Our result showed a threading dislocation density of 3.5×10^8cm^{-2} was achieved by direct depositing the SPSL silicon doped AlGaN layer on AlN template.

Deep UV LEDs developed by adopting conventional nAlGaN, silicon doping modulation nAlGaN and SPSL silicon doped AlGaN on AlN with dislocation density of 1.2×10^9cm^{-2}, 3×10^8cm^{-2} and 3.5×10^8cm^{-2} respectively were characterized by on wafer electroluminescence to investigate the influence of the dislocation density on the optical power. The results showed that both of the LEDs adopting proposed nAlGaN techniques with threading dislocation of around 3×10^8cm^{-2} show dramatic (>30%) improvement in optical power. Deep UV LED device fabricated on the silicon doping modulation LED shows a 25% increase of it optical power (from 0.48mW to 0.61mW) as compared to the conventional LED, which attributes to the reduction of the dislocation density. The results also exhibit a slightly drop of device driving voltage due to the improvement of nAlGaN sheet resistance.

6.2 FUTURE WORK

This work propose Silicon doping modulation technique and short period superlattice technique to improve the layer quality and control the layer sheet resistance in the high aluminum content (> 50%) electron cladding AlGaN layer. Both of the concepts will be adopted in the p-type layer to decrease dislocations generated due to the

lattice mismatch between high aluminum content electron blocking layer and the p-GaN layer. Furthermore, since the experiments have shown that the short period superlattice silicon doped AlGaN technique is able to maintain crystal quality or defect level on AlN template. This will help to dramatically reduce the unit cost of Deep UV LED, since the superlattice template requires long preparation time and large amount of metal organic sources, carrier gases, Ammonia, etc.

There are some other issues that cause the degradation of the recombination efficiency. Currently, most of the Nitride-based LED devices with crystal structures grown along c-orientation exhibit spontaneous and strain- induced piezoelectric fields which can cause degradation in device performance, especially the combination efficiency, due to the reduced recombination probability of the electrons cloud and holes cloud in the active region, which is also known as quantum confine stark effect (QCSE). We have demonstrated that the use of semipolar or nonpolar sapphire substrate is effective in reducing the QCSE phenomenon; however, the device optical power was low, due to the existence of high threading dislocation in the active layer. To further reduce the defects density, a high quality AlN template is prerequisite for the development of the high power Deep UV LED on semipolar or nonpolar sapphire substrate and will be studied in the future.

BIBLIOGRAPHY

[1]   Asif Khan, K. Balakrishnan, "Present Status of Deep UV Nitride Light Emitters," *Mater Sci Forum,* vol. 590, p. 141, 2008.

[2]   Pankove J. I., Miller E. A., and Berkeyheiser J. E., "GaN electroluminescent diodes," *RCA Review,* vol. 32, p. 383, 1971.

[3]   Maruska H. P., Rhines W. C., Stevenson D. A., "Preparation of Mg-doped GaN diodes exhibiting violet," *Mat. Res. Bull.,* vol. 7, p. 777, 1972.

[4]   W. M. Yim and R. J. Paff, "Thermal expansion of AlN, sapphire, and silicon," *J. Appl. Phys.,* vol. 45, p. 1456, 1974.

[5]   H. Amano, N. Sawaki, I. Akasaki and Y. Toyoda, "Metalorganic vapor phase epitaxial growth of a high quality GaN film using an AlN buffer layer," *Appl. Phys. Lett.,* vol. 48, p. 353, 1986.

[6]   I. Akasaki, H. Amano, Y. Koide, K. Hiramatsu, and N. Sawaki, "Effects of ain buffer layer on crystallographic structure and on electrical and optical properties of GaN and Ga1−xAlxN (0 < x ≦ 0.4) films grown on sapphire substrate by MOVPE," *J. Cryst. Growth,* vol. 98, p. 209, 1989.

[7]   Y. Koide, N. Itoh, K. Itoh, N. Sawaki and I. Akasaki, "Effect of AlN Buffer Layer on AlGaN/α-Al2O3 Heteroepitaxial Growth by Metalorganic Vapor Phase Epitaxy," *Jpn. J. Appl. Phys.,* vol. 27, p. 1156, 1988.

[8]   H. Amano, I. Akasaki, K. Hiramatsu, N. Koide and N. Sawaki, "Effects of the buffer layer in metalorganic vapour phase epitaxy of GaN on sapphire substrate," *Thin Solid Films,* vol. 163, p. 415, 1988.

[9]   H. Amano, M. Kito, K. Hiramatsu, and I. Akasaki, "P-Type Conduction in Mg-Doped GaN Treated with Low-Energy Electron Beam Irradiation (LEEBI)," *Jpn. J. Appl. Phys.,* vol. 28, p. L2112, 1989.

[10]   S. Nakamura, "GaN Growth Using GaN Buffer Layer," *Jpn. J. Appl. Phys.,* vol. 30, p. L1705, 1991.

[11]   Nakamura S., Senoh M., Iwasa N., Nagahama S., "High-brightness InGaN blue, green, and yellow lightemitting diodes with quantum well structures," *Jpn. J. Appl. Phys.,* vol. 34, p. L797, 1995.

[12]   Nakamura S., Senoh M., Nagahama S., Iwasa N., Yamada T., Matsushita T., Sugimoto Y., and Kiyoku H. , "Room-temperature continuous-wave operation of InGaN multi-quantum-well structure laser diodes," *Appl. Phys. Lett.,* vol. 69, p. 4056, 1996.

[13]   Nakamura, S.; Fasol, G., "The Blue Laser Diode: GaN Based Light Emitters and Lasers," Berlin, Germany, Springer, 1997, p. 216.

[14]   "U.S. Department of Energy," 2012. [Online]. Available: http://www1.eere.energy.gov/buildings/ssl/highlights_cree06.html.

[15]   K. Balakrishnan, M. Lachab, H. C. Chen, D. Blom, V. Adivarahan, I. Ahmad, Q. Fareed, M. A. Khan, "MOCVD growth of semipolar AlxGa1−xN on m-plane sapphire for applications in deep-ultraviolet light emitters," *physica status solidi A,* vol. 208, p. 2724, 2011.

[16]   E. F. Schubert, Light-Emitting Diodes, Cambridge University Press; 2 edition, 2006.

[17]   X. A. Cao, J. A. Teetsov, F.Shahedipour-Sandvik F, and S. D. , *J. Cryst. Growth,* vol. 264, p. 172, 2004.

[18]   T. Lei, K. F. Ludwig, and T.D. Moustakas, *J. Appl. Phys.,* vol. 74, p. 4430, 1993.

[19]   H. S. Cheong, M. G. Na, Y. J.Choi, T. V. Cuong, C. H. Hong, E. K. Suh, B. H. Kong, and H.K. Cho, *J. Cryst. Growth,* vol. 298, p. 699, 2007.

[20]   C. Q. Chen, V. Adivarahan, M. Shatalov, M. E. Gaevski, E. Kuokstis, J. W. Yang, H. P. Maruska, Z. Gong, M. Asif Khan, R. Liu, A. Bell, and F. A. Ponce, *Phys. Status Solidi ,* vol. 2, p. 2732, 2005.

[21] T. Paskova and K. R. Evans, *IEEE J. Sel. Top. Quantum Electron,* vol. 15, p. 1041, 2009.

[22] S. W. Kim, H. Aida, and T.Suzuki, *Phys. Status Solidi C,* vol. 10, p. 2483, 2004.

[23] Z. Y. Li, M. H. Lo, C. H. Chiu, P. C. Lin, T. C. Lu, H. C. Kuo, and S. C. Wang, *J. Appl. Phys.,* vol. 105, p. 013013, 2009.

[24] X. Ni, J. Lee, M. Wu, X. Li, R. Shimada, Ü. Özgür, A. A. Baski, H. Morkoç, T. Paskova, G. Mulholland, and K. R. Evans, "Internal quantum efficiency of c-plane InGaN and m-plane InGaN on Si and GaN," *Appl. Phys. Lett.,* vol. 95, p. 101106, 2009.

[25] H.-W. Huang, C. C. Kao, J. T.Chu, S. C. Wang and C. C. , "Improvement of InGaN-GaN Light-Emitting Diode," *IEEE Photonics Technology Letters,* vol. 17, p. 983, 2005.

[26] M. Y. Hsieh, C. Y. Wang, L. Y. Chen, T. P. Lin, M. Y. , "Improvement of External Extraction Efficiency in GaN Based LEDs by SiO2 Nanosphere Lithography," *IEEE Electron Device Letters,* vol. 29, p. 658, 2008.

[27] Tadatomo K, Okagawa H, Ohuchi Y, Tsunekawa T, Imada Y,Kato M and Taguchi T, "High output power InGaN ultraviolet light-emitting diodes fabricated on patterned substrates using metalorganic vapor phase epitaxy," *Japan. J. Appl. Phys.,* vol. 40, p. L583, 2001.

[28] M Ali, O Svensk, L Riuttanen, M Kruse, S Suihkonen, A E Romanov, P T Törmä, M Sopanen, H Lipsanen, M A Odnoblyudov and V E Bougrov, "Enhancement of near-UV GaN LED light extraction efficiency by GaN/sapphire template patterning," *Semicond. Sci. Technol.,* vol. 27, p. 082002, 2012.

[29] M. R. Krames et al., "igh-power truncated-inverted-pyramid (AlxGa1−x)0.5In0.5P/GaP light-emitting diodes exhibiting >50% external quantum efficiency," *Appl. Phys. Lett.,* vol. 75, p. 2365, 1999.

[30] C. F. Shen, S. J. Chang, W. S. Chen, T. K. Ko, C. T. Kuo , "Nitride-Based High-Power Flip-Chip LED with Double-Side Patterned Sapphire Substrate," *IEEE Photonics Technology Letters,* vol. 19, p. 780, 2007.

[31] S. H. Huang, R. H. Horng, K. S. When, Y. F. Lin, K. W. , "Improved Light Extraction of Nitride-Based Flip-Chip Light-Emitting Diodes via Sapphire Shaping

and Texturing," *IEEE Photonics Technology Letters,* vol. 18, p. 2623, 2006.

[32] Hung-Wen Huang, Chung-Hsiang Lin, Zhi-Kai Huang, Kang-Yuan Lee, Chang-Chin Yu, and Hao-Chung Kuo, "Improved Light Output Power of GaN-Based Light-Emitting Diodes Using Double Photonic Quasi-Crystal Patterns," *IEEE Electron Device Letters,* vol. 30, p. 1152, 2009.

[33] J. Shakya, K. H. Kim, J. Y. Lin, and H. X. Jiang, "Enhanced light extraction in III-nitride ultraviolet photonic crystal light-emitting diodes," *Appl. Phys. Lett.,* vol. 85, p. 142, 2004.

[34] Tetsuo Fujii et al., "Micro Cavity Effect in GaN-Based Light-Emitting Diodes Formed by Laser Lift-Off and Etch-Back Technique," *Jpn. J. Appl. Phys.,* vol. 43, p. L411, 2004.

[35] Michael R. Krames,Oleg B. Shchekin, Regina Mueller-Mach, Gerd O. Mueller, Ling Zhou,Gerard Harbers, and M. George Craford, "Status and Future of High-Power Light-Emitting Diodes for Solid-State Lighting," *Journal of Display Technology,* vol. 3, p. 160, 2007.

[36] Sari Vilhunen&Heikki Särkkä&Mika Sillanpää, "Ultraviolet light-emitting diodes in water disinfection," *Environ Sci Pollut Res Int.,* vol. 16, p. 439, 2009.

[37] N. Ryškeviča, S. Juršėnasa, P. Vittaa, E. Bakienėb, R. Gaskac, A. Žukauskasa, "Concept design of a UV light-emitting diode based fluorescence sensor for real-time bioparticle detection," *Sensors and Actuators B: Chemical,* p. 371, 2010.

[38] P. Vitta ; N. Kurilcik ; S. Jursenas ; A. Zukauskas ; E. Bakiene ; J. Zhang ; T. Katona ; Y. Bilenko ; A. Lunev ; X. Hu ; J. Deng ; R. Gaska, "Fluorescence-lifetime identification of biological agents using deep ultraviolet light-emitting diodes," *Proc. SPIE,* vol. 5990, pp. 59900X-1, 2005.

[39] Gang Chen, Feras Abou-Galala, Zhengyuan Xu, Brian M. Sadler, "Experimental evaluation of LED-based solar blind NLOS communication links," *Optics Express,* vol. 16, no. 19, p. 15059, 2008.

[40] "National Aeronautics and Space Administration," [Online]. Available: http://www.nasa.gov/.

[41] J. Han, M. H. Crawford, R. J. Shul, J. J. Figiel, M. Banas, L. Zhang, Y. K. Song, H. Zhou, and A. V. Nurmikko, "AlGaN/GaN quantum well ultraviolet light emitting

diodes," *Appl. Phys. Lett.,* vol. 73, p. 1688, 1998.

[42] T. Nishida, H. Saito, and N. Kobayashi, "Submilliwatt operation of AlGaN-based ultraviolet light-emitting diode using short-period alloy superlattice," *Appl. Phys. Lett.,* vol. 78, p. 399, 2001.

[43] V. Adivarahan, A. Chitnis, J. P. Zhang, M. Shatalov, J. W. Yang, G. Simin, M. Asif Khan, R. Gaska, and M. S. Shur, "Ultraviolet light-emitting diodes at 340 nm using quaternary AlInGaN multiple quantum wells," *Appl. Phys. Lett.,* vol. 79, p. 4240, 2001.

[44] A. Kinoshita, H. Hirayama, M. Ainoya, Y. Aoyagi, and A. Hirata, "Room-temperature operation at 333 nm of Al0.03Ga0.97N/Al0.25Ga0.75N quantum-well light-emitting diodes with Mg-doped superlattice layers," *Appl. Phys. Lett.,* vol. 77, p. 175, 2000.

[45] Muhammad Asif Khan, Vinod Adivarahan, Jian Ping Zhang, Changqing Chen, Edmundas Kuokstis, Ashay Chitnis, Maxim Shatalov, Jin Wei Yang and Grigory Simin, "Stripe Geometry Ultraviolet Light Emitting Diodes at 305 Nanometers Using Quaternary AlInGaN Multiple Quantum Wells," *Jpn. J. Appl. Phys.,* vol. 40, p. L1308, 2001.

[46] V. Adivarahan, S. Wu, A. Chitnis, R. Pachipulusu, V. Mandavilli, M. Shatalov, J. P. Zhang, M. Asif Khan, G. Tamulaitis, A Sereika, I. Yilmaz, M. S. Shur, and R. Gaska, "AlGaN single-quantum-well light-emitting diodes with emission at 285 nm," *Appl. Phys. Lett.,* vol. 81, p. 3666, 2002.

[47] J. P. Zhang, A. Chitnis, V. Adivarahan, S. Wu, V. Mandavilli, R. Pachipulusu, M. Shatalov, G. Simin, J. W. Yang, and M. Asif Khan, "Milliwatt power deep ultraviolet light-emitting diodes over sapphire with emission at 278 nm," *Appl. Phys. Lett.,* vol. 81, p. 4910, 2002.

[48] Fujioka A, Misaki T, Murayama T, Narukawa Y and Mukai T, " Improvement in output power of 280-nm deep ultraviolet light-emitting diode by using AlGaN multi quantum wells," *Appl. Phys. Express,* vol. 3, p. 041001, 2010.

[49] K. Mayes, A. Yasan, R. McClintock, D. Shiell, S. R. Darvish, P. Kung, and M. Razeghi, "High-power 280 nm AlGaN light-emitting diodes based on an asymmetric single-quantum well," *Appl. Phys. Lett. ,* vol. 84, p. 1046, 2004.

[50] Yitao Liao, Christos Thomidis, Chen-kai Kao, and Theodore D. Moustakas, "AlGaN based deep ultraviolet light emitting diodes with high internal quantum

efficiency grown by molecular beam epitaxy," *Appl. Phys. Lett.,* vol. 98, p. 081110, 2011.

[51] Hideki Hirayama, Tohru Yatabe, Norimichi Noguch2, Tomoaki Ohashi, and Norihiko Kamata, "231–261 nm AlGaN deep-ultraviolet light-emitting diodes fabricated on AlN multilayer buffers grown by ammonia pulse-flow method on sapphire," *Appl. Phys. Lett.,* vol. 91, p. 071901, 2007.

[52] V. Adivarahan, W. H. Sun, A. Chitnis, M. Shatalov, S. Wu, H. P. Maruska, and M. Asif Khan, "250 nm AlGaN light-emitting diodes," *Appl. Phys. Lett.,* vol. 85, p. 2175, 2004.

[53] J. R. Grandusky, S. R. Gibb, M. C. Mendrick, and L. J. Schowalter, "Properties of Mid-Ultraviolet Light Emitting Diodes Fabricated from Pseudomorphic Layers on Bulk Aluminum Nitride Substrates," *Appl. Phys. Express,* vol. 3, p. 072103, 2010.

[54] Hideki Hirayama, Norimichi Noguchi, Tohru Yatabe, and Norihiko Kamata, "227 nm AlGaN Light-Emitting Diode with 0.15 mW Output Power Realized using a Thin Quantum Well and AlN Buffer with Reduced Threading Dislocation Density," *Appl. Phys. Express,* vol. 1, p. 051101, 2008.

[55] Y. Taniyasu, M. Kasu, and T. Makimoto, "An aluminium nitride light-emitting diode with a wavelength of 210 nanometres," *Nature,* vol. 444, p. 325, 2006.

[56] Edmond J et al, "High efficiency GaN-based LEDs and lasers on SiC," *J. Cryst. Growth,* vol. 272, p. 242, 2004.

[57] Kneissl M, Yang Z, Teepe M, Knollenberg C, Johnson N M, Usikov A and Dmitriev V, "Ultraviolet InAlGaN light emitting diodes grown on hydride vapor phase epitaxy AlGaN/sapphire template," *Japan. J. Appl. Phys.,* vol. 45, p. 3905, 2006.

[58] Tsuzuki H et al , "High-performance UV emitter grown on high-crystalline quality AlGaN underlying layer," *Phys. Status Solidi a,* vol. 206, p. 1199, 2009.

[59] H. Tsuzuki, F. Mori, K. Takeda, M. Iwaya, S. Kamiyama, H. Amano, I. Akasaki, H. Yoshida, M. Kuwabara, Y. Yamashita, and H. Kan,, "Novel UV devices on high-quality AlGaN using grooved underlying layer," *J. Cryst. Growth,* vol. 311, p. 2860, 2009.

[60] Michael Kneissl, Zhihong Yang, Mark Teepe, Cliff Knollenberg, Noble M. Johnson, Alexander Usikov and Vladimir Dmitriev, "Ultraviolet InAlGaN Light

Emitting Diodes Grown on Hydride Vapor Phase Epitaxy AlGaN/Sapphire Templates," *Jpn. J. Appl. Phys.,* vol. 45, p. 3905, 2006.

[61] C. Pernot, M. Kim, S. Fukahori, T. Inazu, T. Fujita, Y. Nagasawa, A. Hirano, M. Ippommatsu, M. Iwaya, S. Kamiyama, I. Akasaki, and H. Amano, "Improved Efficiency of 255–280 nm AlGaN-Based Light-Emitting Diodes," *Appl. Phys. Express,* vol. 3, p. 061004, 2010.

[62] C. Pernot, S. Fukahori, T. Inazu, T. Fujita, M. Kim, Y. Nagasawa, A. Hirano, M. Ippommatsu, M. Iwaya, S. Kamiyama, I. Akasaki, and H. Amano, "Development of high efficiency 255–355 nm AlGaN-based light-emitting diodes," *Phys. Status Solidi A,* vol. 208, p. 1594, 2011.

[63] M Kneissl, T Kolbe, C Chua, V Kueller, N Lobo, J Stellmach, A Knauer, H Rodriguez, S Einfeldt, Z Yang, N M Johnson and M Weyers, "Advances in group III-nitride-based deep UV light-emitting diode technology," *Semicond. Sci. Technol.,* vol. 26, p. 014036, 2011.

[64] C. J. Sun, P. Kung, A. Saxler, H. Ohsato, K. Haritos, and M. Razeghi, "A crystallographic model of (00·1) aluminum nitride epitaxial thin film growth on (00·1) sapphire substrate," *J. Appl. Phys.,* vol. 75, p. 3964, 1994.

[65] Sergey Yu. Karpov and Yuri N. Makarov, "Dislocation effect on light emission efficiency in gallium nitride," *Appl. Phys. Lett.,* vol. 81, p. 4721, 2002.

[66] J. S. Speck and S. J. Rosner, "The role of threading dislocations in the physical properties of GaN and its alloys," *Physica B,* vol. 273, p. 24, 1999.

[67] A. F. Wright and U. Grossner, "The effect of doping and growth stoichiometry on the core structure of a threading edge dislocation in GaN," *Appl. Phys. Lett. ,* vol. 73, p. 2751, 1998.

[68] W. Schockley and W. T. Read, Jr., "Statistics of the Recombinations of Holes and Electrons," *Phys. Rev. B,* vol. 87, p. 835, 1952.

[69] J. Bai, M. Dudley, W. H. Sun, H. M. Wang, and M. Asif Khan, "Reduction of threading dislocation densities in AlN/ sapphire epilayers driven by growth mode modification," *Appl. Phys. Lett.,* vol. 88, p. 051903, 2006.

[70] S.B. Thapa, C. Kirchner, F. Scholz, G.M. Prinz, K. Thonke, R. Sauer, A. Chuvilin, J. Biskupek, U. Kaiser, D. Hofstetter, "Structural and spectroscopic properties of

AlN layers grown by MOVPE," *J. Crystal Growth,* vol. 298, p. 383, 2007.

[71] Y Ohba, R Sato, "Growth of AlN on sapphire substrates by using a thin AlN bu!er layer grown two-dimensionally at a very low V/III ratio," *J. Crystal Growth,* vol. 221, p. 258, 2000.

[72] Masataka Imura, Naoki Fujimoto, Narihito Okada, Krishnan Balakrishnan, Motoaki Iwaya, Satoshi Kamiyama, Hiroshi Amano, Isamu Akasaki, Tadashi Noro, Takashi Takagi, Akira Bandoh, "Annihilation mechanism of threading dislocations in AlN grown by growth form modification method using V/III ratio," *J. Crystal Growth,* vol. 300, p. 136, 2007.

[73] Imura et al., "High-Temperature Metal-Organic Vapor Phase Epitaxial Growth of AlN on Sapphire by Multi Transition Growth Mode Method Varying V/III Ratio," *Jpn. J. Appl. Phys.,* vol. 45, p. 8639, 2006.

[74] R. Gaska, C. Chen, J. Yang, E. Kuokstis, A. Khan, G. Tamulaitis, I. Yilmaz, M. S. Shur, J. C. Rojo, and L. J. Schowalter, "Deep-ultraviolet emission of AlGaN/AlN quantum wells on bulk AlN," *Appl. Phys. Lett.,* vol. 81, p. 4658, 2002.

[75] G. Tamulaitis, I. Yilmaz, M. S. Shur, Q. Fareed, R. Gaska, and M. A. Khan, "Photoluminescence of AlGaN grown on bulk AlN substrates," *Appl. Phys. Lett.,* vol. 85, p. 206, 2004.

[76] Zaiyuan Ren, Q. Sun, S.-Y. Kwon, J. Han, K. Davitt, Y. K. Song, A. V. Nurmikko, W. Liu, J. Smart, L. Schowalter, "AlGaN deep ultraviolet LEDs on bulk AlN substrates," *physica status solidi C,* vol. 4, p. 2482, 2007.

[77] Imura et al., "Microstructure of epitaxial lateral overgrown AlN on trench-patterned AlN template by high-temperature metal-organic vapor phase epitaxy," *Appl. Phys. Lett.,* vol. 89, p. 221901, 2006.

[78] J. Mei, F. A. Ponce, R. S. Qhalid Fareed, J. W. Yang, and M. Asif Khan, "Dislocation generation at the coalescence of aluminum nitride lateral epitaxy on shallow-grooved sapphire substrates," *Appl. Phys. Lett.,* vol. 90, p. 221909, 2007.

[79] Hong-Mei Wang, Jian-Ping Zhang, Chang-Qing Chen, Q. Fareed, Jin-Wei Yang, and M. Asif Khan, "AlN/AlGaN superlattices as dislocation filter for low-threading-dislocation thick AlGaN layers on sapphire," *Appl. Phys. Lett.,* vol. 81, p. 604, 2002.

[80] W. H. Sun, J. P. Zhang, J. W. Yang, H. P. Maruska, M. Asif Khan, R. Liu, and F. A. Ponce, "Fine structure of AlN/AlGaN superlattice grown by pulsed atomic-layer epitaxy for dislocation filtering," *Appl. Phys. Lett.,* vol. 87, p. 211915, 2005.

[81] R. Jain, W. Su1, J. Yang, M. Shatalov, X. Hu, A. Sattu, A. Lunev, J. Deng, I. Shturm, Y. Bilenko, R. Gaska, and M. S. Shur, "Migration enhanced lateral epitaxial overgrowth of AlN and AlGaN for high reliability deep ultraviolet light emitting diodes," *Appl. Phys. Lett.,* vol. 93, p. 051113 , 2008.

[82] Sten Heikman, Stacia Keller, Scott Newman, Yuan Wu, Craig Moe, Brendan Moran, Mathew Schmidt, Umesh K. Mishra, James S. Speck and Steven P. DenBaars, "Epitaxial Lateral Overgrowth of High Al Composition AlGaN Alloys on Deep Grooved SiC Substrates," *Jpn. J. Appl. Phys.,* vol. 44, p. L405, 2005.

[83] J.R. Grandusky, J.A. Smart, M.C. Mendrick, L.J. Schowalter, K.X. Chen, E.F. Schubert, "Pseudomorphic growth of thick n-type $Al_xGa_{1-x}N$ layers on low-defect-density bulk AlN substrates for UV LED applications," *J. Crystal Growth,* vol. 311, p. 2864, 2009.

[84] James R. Grandusky, Shawn R. Gibb, Mark C. Mendrick, Craig Moe, Michael Wraback, and Leo J. Schowalter, "High Output Power from 260 nm Pseudomorphic Ultraviolet Light-Emitting Diodes with Improved Thermal Performance," *Appl. Phys. Express,* vol. 4, p. 082101, 2011.

[85] Iftikhar Ahmad, Balakrishnan Krishnan, Bin Zhang, Qhalid Fareed, Mohamed Lachab, Joseph Dion, Asif Khan, "Dislocation reduction in high Al-content AlGaN films for deep ultraviolet light emitting diodes," *physica status solidi A,* vol. 208, p. 1501, 2011.

[86] V. F. Mymrin, K. A. Bulashevich, N. I. Podolskaya, and S. Y. Karpov, "Bandgap engineering of electronic and optoelectronic devices on native AlN and GaN substrates: A modeling insight," *J. Cryst. Growth,* vol. 281, p. 115, 2005.

[87] A. Y. Polyakov, N. B. Smirnov, A. V. Govorkov, M. G. Milvidskii, J. M. Redwing, M. Shin, M. Skowronski, D. W. Greve, and R. G. Wilson, "Properties of Si donors and persistent photoconductivity in AlGaN," *Solid-State Electron,* vol. 42, p. 627, 1998.

[88] C. Stampfl and C. G. Van der Walle, "Doping of $Al_xGa_{1-x}N$," *Appl. Phys. Lett.,* vol. 72, p. 459, 1998.

[89] W Götz, R.S Kern, C.H Chen, H Liu, D.A Steigerwald, R.M Fletcher, "Hall-effect characterization of III–V nitride semiconductors for high efficiency light emitting diodes," *Mater. Sci. Eng. B,* vol. 59, p. 211, 1999.

[90] Bilenko et al., "10 Milliwatt Pulse Operation of 265nm AlGaN Light Emitting Diodes," *Jpn. J. Appl. Phys. ,* vol. 44, p. L98, 2005.

[91] K. Zhu, M. L. Nakarmi, K. H. Kim, J. Y. Lin, and H. X. Jiang, "Silicon doping dependence of highly conductive n-type Al0.7Ga0.3N," *Appl. Phys. Lett.,* vol. 85, p. 4669, 2004.

[92] Jianchang Yan, Junxi Wang, Peipei Cong, Lili Sun, Naixin Liu, Zhe Liu, Chao Zhao, Jinmin Li, "Improved performance of UV-LED by p-AlGaN with graded composition," *physica status solidi C,* vol. 8, p. 461, 2010.

[93] Hideki Hirayama, Yusuke Tsukada, Tetsutoshi Maeda1, and Norihiko Kamata, "Marked Enhancement in the Efficiency of Deep-Ultraviolet AlGaN Light-Emitting Diodes by Using a Multiquantum-Barrier Electron Blocking Layer," *Appl. Phys. Express,* vol. 3, p. 031002, 2010.

[94] Akira Fujioka, Takao Misaki, Takashi Murayama, Yukio Narukawa, and Takashi Mukai, "Improvement in Output Power of 280-nm Deep Ultraviolet Light-Emitting Diode by Using AlGaN Multi Quantum Wells," *Appl. Phys. Express,* vol. 3, p. 041001, 2010.

[95] M. Shatalov, A. Chitnis, P. Yadav, Md. F. Hasan, J. Khan, V. Adivarahan, H. P. Maruska, W. H. Sun, and M. Asif Khan, "Thermal analysis of flip-chip packaged 280 nm nitride-based deep ultraviolet light-emitting diodes," *Appl. Phys. Lett.,* vol. 86, p. 201109, 2005.

[96] Hwang et al., "276nm Substrate-Free Flip-Chip AlGaN Light-Emitting Diodes," *Appl. Phys. Express,* vol. 4, p. 032102, 2011.

[97] L. Zhou, J. E. Epler, M. R. Krames, W. Goetz, M. Gherasimova, Z. Ren, J. Han, M. Kneissl, and N. M. Johnson, "Vertical injection thin-film AlGaN/AlGaN multiple-quantum-well deep ultraviolet light-emitting diodes," *Appl. Phys. Lett.,* vol. 89, p. 241113, 2006.

[98] N. Lobo, H. Rodriguez, A. Knauer, M. Hoppe, S. Einfeldt, P. Vogt, M. Weyers, and M. Kneissl, "Enhancement of light extraction in ultraviolet light-emitting diodes using nanopixel contact design with Al reflector," *Appl. Phys. Lett.,* vol. 96,

p. 081109, 2010.

[99] M. Khizar, Z. Y. Fan, K. H. Kim, J. Y. Lin, and H. X. Jiang, "Nitride deep-ultraviolet light-emitting diodes with microlens array," *Appl. Phys. Lett.,* vol. 86, p. 173504, 2005.

[100] Shatalov et al., "AlGaN Deep-Ultraviolet Light-Emitting Diodes with External Quantum Efficiency above 10%," *Appl. Phys. Express,* vol. 5, p. 082101, 2012.

[101] Iftikhar Ahmad, Balakrishnan Krishnan, Bin Zhang, Qhalid Fareed, Mohamed Lachab, Joseph Dion, Asif Khan, "Dislocation reduction in high Al-content AlGaN films for deep ultraviolet light emitting diodes," *physica status solidi A,* vol. 208, p. 1501, 2011.

[102] "Thin Film," [Online]. Available: http://www.eng.usf.edu/~tvestgaa/ThinFilm/.

[103] D. K. Schroder, Semiconductor Material and Device Characterization, 3rd Edition, Wiley-Interscience, 2006.

[104] D. K. Schroder, Semiconductor material and device characterization, John Wiley & Sons, Inc., 2006.

[105] "The van der Pauw Technique," [Online]. Available: http://tau.nanophys.kth.se/cmp/hall/node5.html.

[106] M.A.Moram and M.E.Vickers, "X-ray diffraction of III-nitrides," *Rep. Prog. Phys,* vol. 72, p. 036502, 2009.

[107] J. A. Dion, *Reduced Defect Density nAlGaN Template Layer for Improved Output Deep-UV LED,* PhD dissertation,University of South Carolina, ProQuest/ UMI, 2010.

[108] H. Chen, "STRUCTURAL AND MORPHOLOGICAL ANALYSES OF AlN AND AlGaN LAYERS," University of South Carolina, 2010.

[109] C. Skierbiszewski, T. Suski, M. Leszczynski, M. Shin, M. Skowronski, M. D. Bremser, and R. F. Davis, "Evidence for localized Si-donor state and its metastable properties in AlGaN," *Appl. Phys. Lett.,* vol. 74, p. 3833, 1999.

[110] K. B. Nam, J. Li, M. L. Nakarmi, J. Y. Lin, and H. X. Jiang, "Achieving highly conductive AlGaN alloys with high Al contents," *Appl. Phys. Lett.,* vol. 81, p. 1038, 2002.

[111] J. W. Matthews and A. E. Blakeslee, "Defects in epitaxial multilayers," *J. Cryst. Growth,* vol. 27, p. 118, 1974.

[112] L. Romano, C. van de Walle, J. Ager, W. Götz, and R. S. Kern, "Effect of Si doping on strain, cracking, and microstructure in GaN thin films grown by metalorganic chemical vapor deposition," *J. Appl. Phys.,* vol. 87, p. 7745, 2000.

[113] P. Cantu, F. Wu, P. Waltereit, S. Keller, A. E. Romanov, U. K. Mishra, S. P. DenBaars, and J. S. Speck, Appl. Phys. Lett. 83, 674 (2003)., "Si doping effect on strain reduction in compressively strained Al0.49Ga0.51N thin films," *Appl. Phys. Lett.,* vol. 83, p. 674, 2003.

[114] Wenhong Sun, Vinod Adivarahan, Maxim Shatalov, Youngbae Lee, Shuai Wu, Jinwei Yang, Jianping Zhang and M. Asif Khan, "Continuous Wave Milliwatt Power AlGaN Light Emitting Diodes at 280 nm," *Jpn. J. Appl. Phys.,* vol. 43, p. L1419, 2004.

[115] M. Shatalov, A. Chitnis, V. Mandavilli, R. Pachipulusu, J. P. Zhang, V. Adivarahan, S. Wu, G. Simin, M. Asif Khan, G. Tamulaitis, A. Sereika, I. Yilmaz, M. S. Shur, and R. Gaska, "Time-resolved electroluminescence of AlGaN-based light-emitting diodes with emission at 285 nm," *Appl. Phys. Lett.,* vol. 82, p. 167, 2003.

[116] J. Wu, W. Walukiewicz, W. Shan, K. M. Yu, J. W. Ager, S. X. Li, E. E., "Temperature dependence of the fundamental band gap of InN," *J. Appl. Phys.,* vol. 94, 2003.